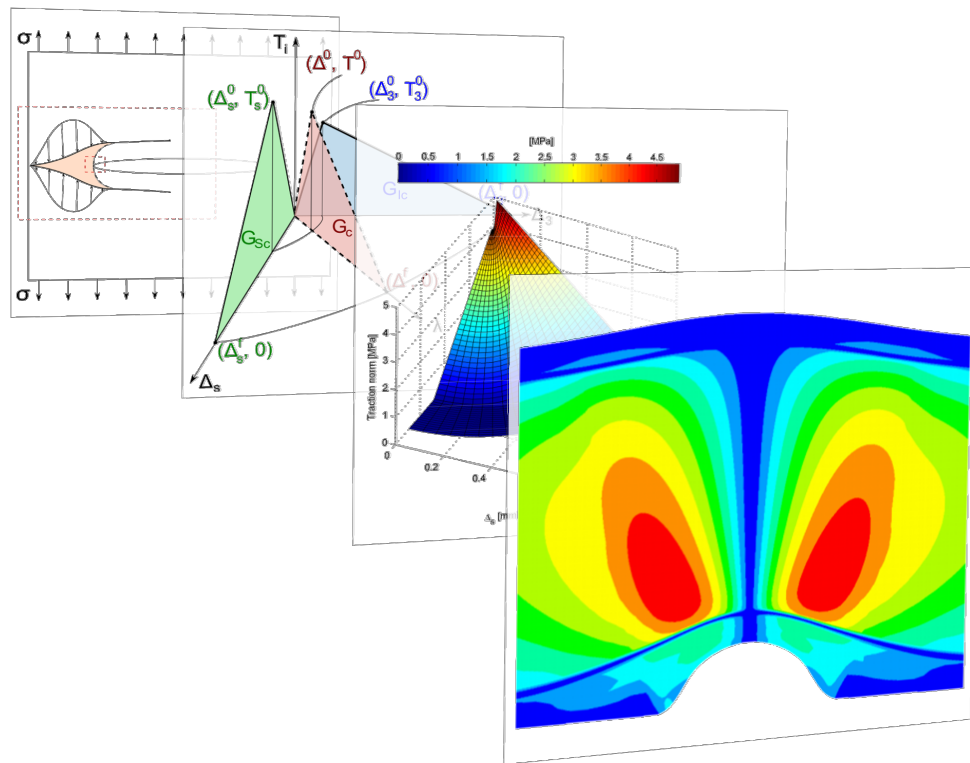


# Formulation of Cohesive Finite Element for Analysing Strength of Wrinkles in Glass-Epoxy Laminates



PROJECT GROUP DMS466B

4<sup>TH</sup> SEMESTER

DESIGN OF MECHANICAL SYSTEMS

AALBORG UNIVERSITY

THE 4<sup>TH</sup> OF JUNE 2013





**Title:** Formulation of Cohesive Finite Element for Analysing Strength of Wrinkles in Glass-Epoxy Laminates  
**Semester:** 4  
**Semester theme:** Master Thesis  
**Project period:** 01/02-2013 to 04/06-2013  
**ECTS:** 30  
**Supervisor:** Esben Lindgaard  
**Project group:** DMS466b

---

Esben Toke Christensen

---

Jonas Heidemann Sjølund

---

Jens Ammitzbøll Glud

**SYNOPSIS:**

This master thesis describes the formulation and use of Cohesive Zone Modelling in the framework of the Finite Element Method. A Cohesive Element is programmed and then validated through a number of comparisons with results from the literature. Difficulties arising when using this method are addressed, and implications hereof are discussed. Subsequently the element is used for analysing the strength of wrinkle defects in Glass-Epoxy Laminates. This is done by studying the influence of the geometrical parameters of the wrinkle through a parametric study. Through a normalised study this is used to propose a simple expression to estimate the strength reduction due to the wrinkle.

Number printed: 6 Pieces  
Pages: 156 Pages  
Appendix: 2  
Enclosures: CD

**By signing this document, each member of the group confirms participation on equal terms in the process of writing the project. Thus, each member of the group is responsible for all the contents of the project.**



# Resumé

Dette kandidatspeciale omhandler formulering af kohæsive elementer og brug heraf til analyse af delamination i en foldningsdefekt i en glas-epoxy lamineret struktur. I begyndelsen af rapporten forklares motivationen for at analysere en foldningsdefekt med brudmekanik. Herefter følger en kort gennemgang af klassisk lineær elastisk brudmekanik. Brudmekanik i form af kohæsiv zone modellering vil herefter blive introduceret, og teori, for hvordan en kohæsiv zone model kan inkorporeres i Finite Element Metoden, vil blive gennemgået. På baggrund af denne teori vil en kohæsiv brugerelementrutine blive programmeret. Denne rutine er anvendt i sammenhæng med det kommercielle Finite Element program ANSYS. For at verificere, at den programmerede rutine virker efter hensigten, er en række verifikationsforsøg udført med rutinen. I disse forsøg sammenholdes resultater fra den kohæsive brugerelementrutine med klassiske brudmekaniske løsninger og løsninger fundet ved brug af den allerede eksisterende kohæsive elementrutine indbygget i ANSYS. Introduktion af kohæsive elementer gør et problem ulineært. Løsningen af et ulineært problem med kohæsive elementer kan give konvergensproblemer. I denne forbindelse undersøges det hvilke parametre, der har indflydelse på at løse sådanne konvergensproblemer. Efter fuldendt verifikation er den kohæsive brugerelementrutine anvendt til at analysere delamination i en foldningsdefekt. En FE model for en foldningsdefekt, der kan repræsentere fysiske forsøgsemner fra studier udført i litteraturen, er derfor blevet opstillet. Modellen er parametriseret således, at forskellige parametriske studier kan udføres. Resultater fra FE modellen, før og efter delamination, sammenholdes med eksperimentielle DIC målinger udført i litteraturen. Til sidst er der udført parametriske studier for at analysere, hvorledes forskellige geometriske parametre i en foldningsdefekt påvirker bæreevnen af en konstruktion med en sådan defekt. Dette kandidatspeciale omhandler formulering af kohæsive elementer og brug

heraf til analyse af delamination i en foldningsdefekt i en glas-epoxy lamineret struktur. I begyndelsen af rapporten forklares motivationen for at analysere en foldningsdefekt med brudmekanik. Herefter følger en kort gennemgang af klassisk lineær elastisk brudmekanik. Brudmekanik i form af kohæsiv zone modellering vil herefter blive introduceret, og teori, for hvordan en kohæsiv zone model kan inkorporeres i Finite Element Metoden, vil blive gennemgået. På baggrund af denne teori vil en kohæsiv brugerelementrutine blive programmeret. Denne rutine er anvendt i sammenhæng med det kommercielle Finite Element program ANSYS. For at verificere, at den programmerede rutine virker efter hensigten, er en række verifikationsforsøg udført med rutinen. I disse forsøg sammenholdes resultater fra den kohæsive brugerelementrutine med klassiske brudmekaniske løsninger og løsninger fundet ved brug af den allerede eksisterende kohæsive elementrutine indbygget i ANSYS. Introduktion af kohæsive elementer gør et problem ulineært. Løsningen af et ulineært problem med kohæsive elementer kan give konvergensproblemer. I denne forbindelse undersøges det hvilke parametre, der har indflydelse på at løse sådanne konvergensproblemer. Efter fuldent verificering er den kohæsive brugerelementrutine anvendt til at analysere delamination i en foldningsdefekt. En FE model for en foldningsdefekt, der kan repræsentere fysiske forsøgsemner fra studier udført i litteraturen, er derfor blevet opstillet. Modellen er parametriseret således, at forskellige parametriske studier kan udføres. Resultater fra FE modellen, før og efter delamination, sammenholdes med experimentielle DIC målinger udført i litteraturen. Til sidst er der udført parametriske studier for at analysere, hvorledes forskellige geometriske parametre i en foldningsdefekt påvirker den statiske kompressionelle bæreevne af en konstruktion med en sådan defekt.

# Preface

This thesis is written by a 4<sup>th</sup> semester group of the master programme 'Design of Mechanical Systems' at Aalborg University. The project is based on a project proposal from Assistant Professor, Ph.D. Esben Lindgaard and Ph.D. student Brian Bak in collaboration with Siemens Wind Power A/S. Esben Lindgaard is supervisor and Brian Bak is co-supervisor on this project.

## Reading Guide

Throughout the thesis references will be used according to the Harvard method. In the end of the thesis a full list with the complete details such as title, authors, ISBN, publisher, etc. is compiled. Figures and tables are numbered according to the chapter where they are present, so that the first figure in Chapter 7 is called Figure 7.1 etc. Figures and tables have captions with explanatory text. Equation references are numbered the same way, but also takes section numbers into account. Also equations are written inside a parenthesis, e.g. (3.1.1) is the first equation in section 1 of Chapter 3. A list of nomenclature as well as appendices can be found in in the end of the thesis.

A CD containing used literature that has been downloaded from the Internet, the thesis in PDF format, MATLAB scripts, and ANSYS scripts is attached to the thesis.

A special thanks is directed to the project supervisors for providing literature and giving useful suggestions, which helped the authors address and solve problems encountered during the project period. Furthermore a special thanks is directed to Ph.D. Martin Leong for providing additional information regarding his article Leong (2012).



# Contents

<b>1</b>	<b>Introduction</b>	<b>1</b>
1.1	Project Background . . . . .	1
1.2	Problem Specification . . . . .	4
1.3	Problem Solving Approach . . . . .	6
<b>I</b>	<b>Introduction to Cohesive Zone Modeling in the Framework of the Finite Element Method</b>	<b>9</b>
<b>2</b>	<b>Linear Elastic Fracture Mechanics</b>	<b>11</b>
2.1	Concepts of LEFM . . . . .	11
2.2	Test Specimens . . . . .	16
2.3	LEFM in the FEM . . . . .	22
2.4	Conclusion . . . . .	23
<b>3</b>	<b>Modelling the Cohesive Zone</b>	<b>25</b>
3.1	The Cohesive Zone Concept . . . . .	25
3.2	Approach for Combining CZM with the Continuum . . . . .	26
3.3	CZM Formulated as Boundary Value Problem . . . . .	28
3.4	Weak Formulation . . . . .	29
3.5	Kinematics . . . . .	32
3.6	Solvers . . . . .	34
3.7	Discretisation . . . . .	37
3.8	Constitutive Relation . . . . .	42
3.9	Finalising the Element Formulation . . . . .	50
3.10	Conclusion . . . . .	51
<b>4</b>	<b>Implementation and Verification</b>	<b>53</b>

4.1	Implementation of CZ Element . . . . .	54
4.2	Element Verification . . . . .	54
4.3	Application on Specimen Models . . . . .	61
4.4	Influence of Onset Traction . . . . .	70
4.5	Conclusion . . . . .	74
<b>II</b>	<b>Analysis of Wrinkle Defect</b>	<b>75</b>
<b>5</b>	<b>Verification of FE Wrinkle Model</b>	<b>77</b>
5.1	Parametrisation . . . . .	77
5.2	Modelling . . . . .	79
5.3	Meshing . . . . .	81
5.4	Comments to Leong (2012) . . . . .	83
5.5	Comparison with DIC before FM1 . . . . .	84
5.6	Physical Interpretation . . . . .	87
5.7	Conclusion . . . . .	91
<b>6</b>	<b>Delamination in a Wrinkle Defect</b>	<b>93</b>
6.1	Modeling FM1 . . . . .	93
6.2	Modeling FM2 . . . . .	98
6.3	Mode Mixity and Damage . . . . .	100
6.4	Failure Criterion for FM2 . . . . .	101
6.5	Conclusion . . . . .	102
<b>7</b>	<b>Parametric Studies</b>	<b>105</b>
7.1	Approach . . . . .	105
7.2	Analyses in Absolute Parameters . . . . .	108
7.3	Analyses in Normalised Parameters . . . . .	111
7.4	A Simple Criterion . . . . .	113
7.5	Conclusion . . . . .	116
<b>8</b>	<b>Conclusions</b>	<b>117</b>
8.1	Suggestions for Future Work . . . . .	119
	<b>Bibliography</b>	<b>123</b>

*CONTENTS*

xi

**III Appendix**

127

A Fracture Mechanical Properties

B Implementation and Usage of the User Programmed  
Cohesive Zone Element



# Chapter 1

## Introduction

In this chapter the background and motivation for this M.Sc. thesis are presented. Furthermore the problem is clarified, and the problem solving approach is described.

### 1.1 Project Background

This M.Sc. thesis is written in collaboration with Siemens Wind Power A/S (SWP). SWP manufactures horizontal axis wind turbines. In order to lower the cost of produced electricity from the wind turbines, the trend is to manufacture as large blades as possible. By using larger blades the amount of energy that can be harvested from the wind increases, thereby increasing the output of the wind turbine. Larger blades also means heavier blades, which means that other structural components such as nacelle, tower, hub, bearings, etc. have to be larger as well, resulting in higher costs. It is therefore a persistent challenge for wind turbine manufacturers to keep the weight of the blades as low as possible in order to be competitive in the global wind turbine market (Leong, 2012). In order to make low-weight blades, SWP produces blades made of laminated composite materials. The composite materials used consist of glass fiber, epoxy, and balsa wood. Compared to metallic structures these materials give the possibility of making a lighter structure due to the high strength/stiffness to density ratio, and the ease of tailoring the material properties to the given loading at a particular point in the blade. However laminated composite materials also introduce several new failure modes, which are not found in metallic structures. In order to make a weight competitive design, the designer should strive to use the lowest possible Margin of Safety

(MoS) without compromising the structural integrity of the blade. This calls for precise failure criteria. According to Leong (2012, p. 13) the World Wide Failure Exercise (WWFE) ended up showing, that the best failure criteria in 20% of the test cases were off by between 50% and 150%, which obviously cannot be characterised as being precise.

The blades produced by SWP consist of both monolithic laminates and sandwich structures. A part of the blade consisting of a sandwich structure is shown in Figure 1.1. In this thesis the focus will be on sandwich structures.

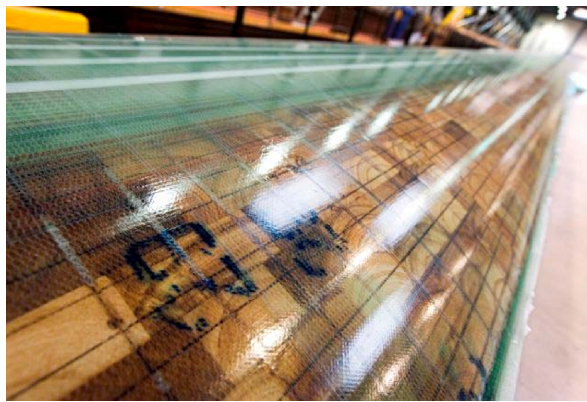


Figure 1.1: Part of SWP blade made as a sandwich structure, where the core material, balsa, can be seen. The picture is taken from the project proposal supplied by the supervisors.

The most commonly occurring failure modes in sandwich structures are shown in Figure 1.2, and their respective names are listed below.

- (a) Facesheet yielding/fracture.
- (b) Core shear failure.
- (c,d) Facesheet wrinkling.
- (e) Buckling.
- (f) Shear crimping.
- (g) Facesheet dimpling.
- (h) Local indentation.

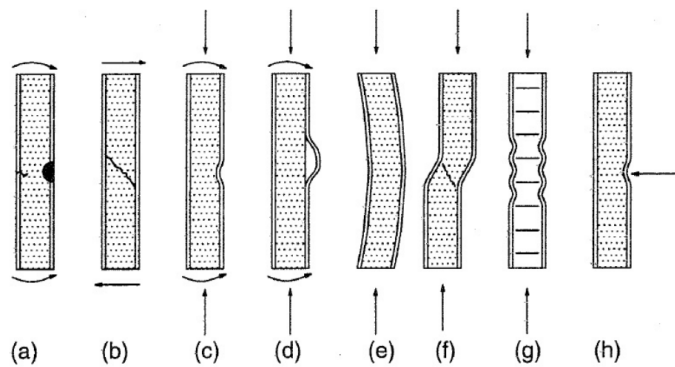


Figure 1.2: Illustration of the most commonly occurring failure modes (Zenkert, 1997).

There are several ways to check for these failure modes. One way is using the Finite Element Method (FEM), which is time consuming for the engineer as well as computationally demanding, and furthermore needs a precise failure criterion, which does not exist in some cases. Another way is to use analytically derived or empirically found criteria for the different failure modes. The failure modes (a) and (b) can be designed against using standard failure criteria as those used in WWFE. For the rest of the failure modes, analytical as well as empirical design guidelines can be found in e.g. Kassapoglou (2010). One thing the failure criteria and design guidelines generally have in common is, that they assume perfectly flat laminates, where no defects are present. Defects are commonly accounted for by increasing the MoS.

SWP produces wind turbine blades using their patented IntegralBlade<sup>®</sup> technology. This technology makes it possible for SWP to cast the entire blade in one process using Vacuum Assisted Resin Transfer Moulding (VARTM), and eliminates the need for subsequent assembly of the blades. According to Leong (2012) the VARTM process potentially introduces defects such as dry spots and wrinkle defects. Dry spots are areas of fiber material which have not been properly impregnated with resin, while wrinkle defects are out-of-plane fiber misalignments. The dry spots have to be repaired after the VARTM process is complete. According to Leong (2012, p.3) blade design engineers have to evaluate, whether a found wrinkle defect has to be repaired or not. Currently the majority of the defects are being repaired.

The focus of the Ph.D. thesis (Leong, 2012) was therefore to analyse wrinkle defects and find a suitable way to characterise, whether a given wrinkle defect would affect the structural integrity of the blade. According to Leong (2012, p.6) the compressive strength of a sandwich panel decreased by up to 55%, when wrinkle defects were present in the specimens investigated. He also found that layerwise delamination was the governing failure mode in specimens with a wrinkle defect. During the testing in Leong (2012), the author was not capable of capturing the damage initiation and propagation, even when a high speed camera recording at 9000 frames per second was used. Leong (2012) applied the Northwestern University (NU) criterion on a linear 3D Finite Element Analysis (FEA) in order to predict damage initiation in the specimens analysed and tested.

This M.Sc. thesis builds upon the work done by Leong (2012), using a different approach for predicting and analysing failure in wrinkle defects. The approach taken will be based on fracture mechanics and more specifically the field of Cohesive Zone Modelling (CZM). Reasons for this choice are elaborated in chapters 2 and 3. It is believed, that by the use of CZM along with the FEM it will be possible to capture and analyse the damage initiation and development. Furthermore establishment of a way to predict the strength of a given specimen will be attempted, and the influence of the governing parameters will be examined.

## 1.2 Problem Specification

As stated above, the purpose of this project is to analyse how wrinkle defects affect the load carrying capability of laminated sandwich structures. An approach to this can be either experimental or by simulation. Leong (2012) focused on the experimental part, but also put some emphasis on failure criteria to be used with a linear FEA. A linear FEA is however only valid up to the point of damage initiation of the predicted failure mode. This is due to the fact, that the effects of the failure mode are not taken into account. For e.g. delamination, a certain failure criterion might be able to predict the strain/stress required for delamination to initiate, but it will not introduce the actual debonding in the model after initiation. This debonding would in a real scenario cause the load to be redistributed in the model. Thus phenomena

occurring after damage initiation are not captured in a linear FEA, and this is where the fracture mechanics approach comes into play.

Fracture mechanics is interesting w.r.t. wrinkle defects since Leong (2012) found that delamination is the critical failure mode. Delamination can be regarded as propagating cracks inbetween the plies. Classically, Linear Elastic Fracture Mechanics (LEFM) is used for dealing with crack propagation, but requires knowledge of an already existing crack. It can be argued that cracks will always exist in real structures due to flaws, but it is often difficult to estimate an initial crack length or even determine the location of such a crack, since the areas of interest are of course not visibly available for inspection, or the cracks are simply too small to be detected. Therefore an approach that requires no initial crack is wanted. This is what CZM offers, as it requires no initial crack, but still relies on well known properties such as critical energy release rates.

By being able to simulate the initiation and propagation of delamination, it is hoped that it can be determined more precisely, whether a wrinkle is critical or not. Although Leong (2012) found the NU criterion to be able to determine delamination initiation, it was also found that much load carrying capability was still left beyond this point as shown on Figure 1.3. Simulation of crack propagation will thus be able to show this remaining strength, and it will allow for parametric studies of the wrinkle, in order to investigate the influence of different wrinkle geometries.

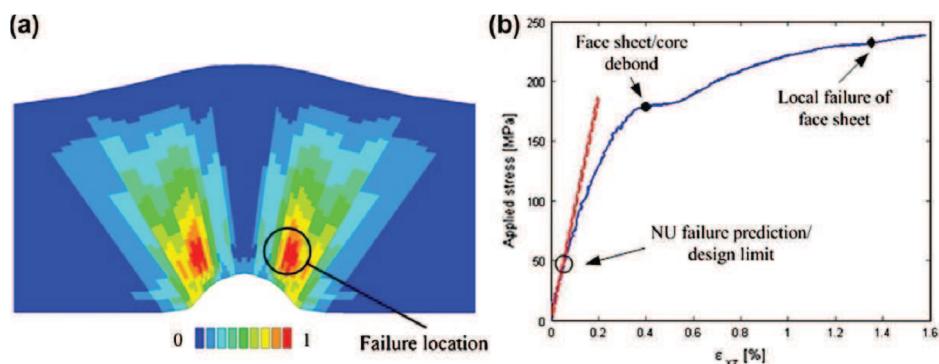


Figure 1.3: (a) NU failure index plot and (b) plot of DIC measured shear strain  $\gamma_{xz}$  vs. applied load at failure location (Leong, 2012).

### 1.3 Problem Solving Approach

As described above the goal of the project is to analyse a wrinkle defect in a composite sandwich structure by the use of CZM. In order to do this, some intermediate steps are required to solve this problem. Of course a literature study has to be performed in order to accumulate knowledge about the subject. This covers both fracture mechanics in general as well as previous studies on the damage mechanics in wrinkle defects. The project group has had the advantage that a good collection of material on both subjects had been collected and provided by supervisors Esben Lindgaard and Brian Bak at the beginning of the project.

The Finite Element (FE) software to be used is ANSYS v14.0. This release already comes with a 3D cohesive zone (CZ) element called INTER205. However the user programmable features of ANSYS will be used, in order to implement a user programmed cohesive zone element. This is done for several reasons: First and foremost, it allows for full customisability of the element formulation and thus opens up as many modelling possibilities as possible. Secondly, the process of implementing the element will give a thorough understanding of the method. Following the implementation of the cohesive zone element, it has to be thoroughly tested in order to verify, that the element formulation is correct. This will be done partly by comparing results obtained from the user programmed element with results obtained using the ANSYS cohesive zone element as well as LEFM, and partly by comparing the behaviours (such as convergence properties) of the user programmed element and the ANSYS element. During the course of the element verification, some of the parameters governing the behaviour of the cohesive zone approach will be investigated in order to gain a deeper understanding of the method. The implementation and verification of the user programmed cohesive zone element will be treated in part 1 of this thesis.

When the element has been properly verified, a parametrised FE model of a wrinkle defect in a laminated composite sandwich structure will be created. Results from this model will then be compared with test data obtained from real specimens and modified as needed in order to obtain a model, that provides good results. Finally, parametric studies are performed on the verified model in order to examine the influence of the wrinkle geometry on the failure

process. This also covers a normalisation of the problem and suggestion of a simple failure criterion. The treatment of wrinkle defects using the cohesive zone modelling approach will be presented in the second part of this thesis.



## Part I

# Introduction to Cohesive Zone Modeling in the Framework of the Finite Element Method



## Chapter 2

# Linear Elastic Fracture Mechanics

In order to treat the subject of this thesis, a natural entry point is to consider the classic approach to fracture mechanics. Therefore in this chapter, the basic concepts of Linear Elastic Fracture Mechanics (LEFM) will be presented, in order to establish the framework for discussing the CZM. LEFM solutions for different simple test specimens will be obtained for later reference and to illustrate the use of LEFM. Finally, the use of LEFM in the FEM will be discussed in order to show some of the advantages and disadvantages of this approach.

### 2.1 Concepts of LEFM

In LEFM the condition for predicting crack growth is either of two approaches: By energy considerations using the energy release rate, or by the stress intensity factor. It can be shown that the stress intensity factor can be related to the energy release rate, and hence is in a way an equivalent concept (Andreasen, 2011, p. 29). Therefore, only the energy release rate approach will be discussed in some detail, whereas the stress intensity factor will only be treated in rough terms.

#### 2.1.1 The Energy Release Rate

The following is primarily based on Andreasen (2011). The concept of the energy release rate is derived by energy considerations for crack growth in the

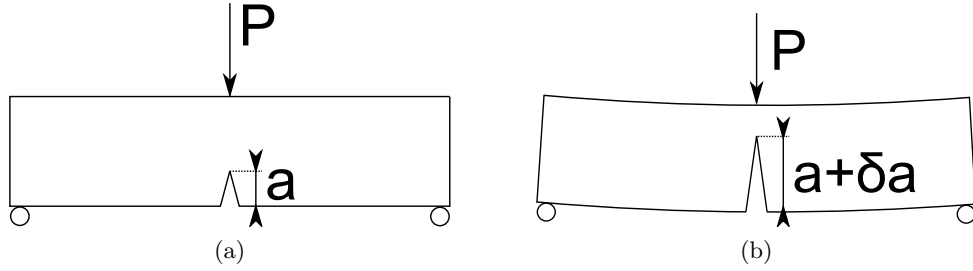


Figure 2.1: Cracked specimen a) before perturbation and b) after perturbation.

situation shown in Figure 2.1a. As seen the problem consists of a specimen with an initial crack of length  $a$  and with an applied load  $P$ . The system is in equilibrium in the shown configuration. Assuming a linear elastic material behaviour, the total elastic potential can be written as

$$\Pi = U(u, a) + V(u, a) \quad (2.1.1)$$

where  $U$  is the strain energy,  $V$  is the potential of the external forces and  $u$  is the displacement field. Note that both the potential of the external force and the strain energy are dependent of the displacement field,  $u$ , and the crack length,  $a$ . Now the subsequent situation, shown in Figure 2.1b is considered, where a variation of the crack length and displacement field is applied to the structure. If the force is kept constant and a quasi-static process is assumed, the energy balance for the two subsequent situations can be written as:

$$0 = U(u + \delta u, a + \delta a) + V(u + \delta u, a + \delta a) + \delta L - U(u, a) - V(u, a) \quad (2.1.2)$$

where  $\delta L$  represents the energy required to form the new crack surface. Making a Taylor-approximation of the variations with respect to the initial configuration, and neglecting terms of second order and higher gives:

$$\begin{aligned} -\delta L = & U(u, a) + V(u, a) + \left( \frac{\partial U}{\partial u} + \frac{\partial V}{\partial u} \right) \delta u + \left( \frac{\partial U}{\partial a} + \frac{\partial V}{\partial a} \right) \delta a \\ & - U(u, a) - V(u, a) \end{aligned} \quad (2.1.3)$$

which reduces to:

$$-\delta L = \left( \frac{\partial U}{\partial u} + \frac{\partial V}{\partial u} \right) \delta u + \left( \frac{\partial U}{\partial a} + \frac{\partial V}{\partial a} \right) \delta a \quad (2.1.4)$$

In the above the first term must be zero due to the principle of minimum total potential energy. Thus the energy required to form a crack surface is given by:

$$-\delta L = \left( \frac{\partial U}{\partial a} + \frac{\partial V}{\partial a} \right) \delta a = \frac{\partial \Pi}{\partial a} \delta a \quad (2.1.5)$$

This brings us to the concept of the energy release rate, which is defined as the change in energy in the system per unit formed crack face. With a change in area of

$$\delta A = t \delta a \quad (2.1.6)$$

where  $t$  is the specimen thickness, the energy release rate then becomes

$$G = \frac{\delta L}{\delta A} = -\frac{1}{t} \frac{\partial \Pi}{\partial a} \quad (2.1.7)$$

From the above derivations it is seen that the energy release rate is dependent on both boundary conditions, constitutive relations and geometry and is thus problem dependent. The way the energy release rate is used to predict crack growth is by comparing it to the critical energy release rate

$$G_c = 2\gamma_0 \quad (2.1.8)$$

where  $\gamma_0$  is the specific free surface energy of the material. Thus the critical energy release rate is a material property. In order for crack growth to be possible, the energy release rate in (2.1.7) must be equal to, or greater than the critical energy release rate. This criterion is known as the Griffith criterion which can more precisely be stated as:

$$G < G_c \quad \text{No crack growth}$$

$$G = G_c \quad \text{Stable crack growth}$$

$$G > G_c \quad \text{Unstable crack growth}$$

The three "categories" in the above formulation of the Griffith criterion can be explained as follows: In the first category, the crack can of course not grow, if the necessary energy for crack growth is not available. In the second category, the system will neither consume or release energy with crack growth, so the crack can grow in a stable manner. In the last category, more energy is put into the system, than the crack consumes when growing. This leads to unstable crack growth, where the crack grows at very high speed.

### 2.1.2 The Stress Intensity Factor

The following is based on Andreasen (2011). As previously mentioned, the stress intensity factor will not be treated in a lot of detail. In order to present the concept, an elliptical hole in a plate is considered. A sketch of the problem is shown in Figure 2.2. According to Andreasen (2011, p. 13), the maximum

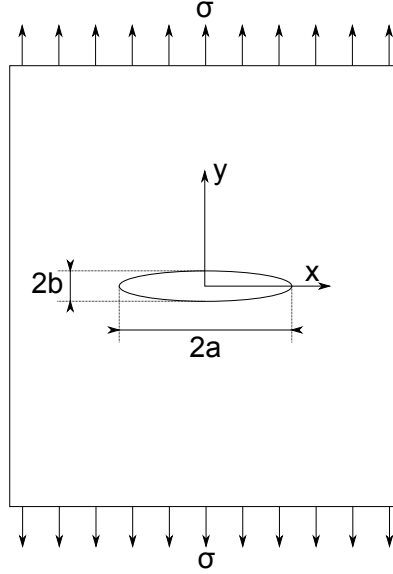


Figure 2.2: Elliptical hole in a plate loaded by a uniform tensile stress.

tensile stress, according to the linear elastic analytic solution, is found at the tip of the elliptical hole  $((x, y) = (a, 0))$ , and has a value of:

$$\sigma_y^{max} = \left(1 + \frac{2a}{b}\right) \sigma \quad (2.1.9)$$

It can therefore be seen, that as the minor axis tends to zero ( $b \rightarrow 0$ ) such that the elliptical hole approaches the shape of a sharp crack, this stress tends to infinity. This would suggest that the structure has no load carrying capability, which is of course not the case. This elastic solution is however found to be useful if the rate at which the stresses go to infinity is considered. For the present case, the tensile stresses in front of the elliptical hole is dominated by the term:

$$\sigma_y = \frac{K}{\sqrt{2\pi(x-a)}} \quad \text{for } x > a \quad (2.1.10)$$

Here  $K$  is called the stress intensity factor, and it describes how quickly the stress approaches infinity. The stress intensity factor in this specific case can

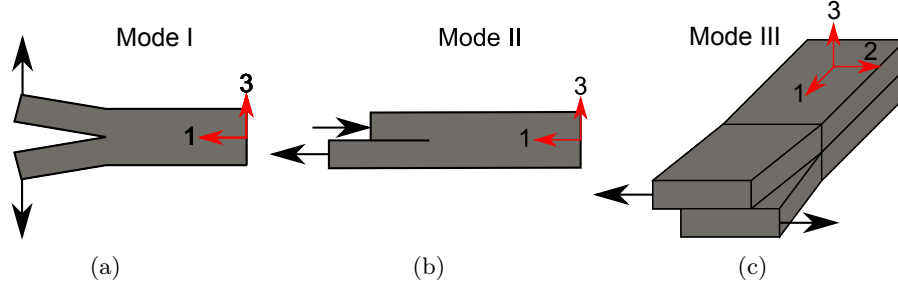


Figure 2.3: a) Mode I crack. b) Mode II crack. c) Mode III crack.

be found as

$$K = \lim_{x \rightarrow a^+} \sigma_y \sqrt{2\pi(x-a)} \quad (2.1.11)$$

In a similar way to the theory regarding the energy release rate, a critical stress intensity factor,  $K_c$ , which is a material property, exists, and crack propagation can be predicted according to the Griffith criterion:

$$\begin{aligned} K < K_c & \text{ No crack growth} \\ K = K_c & \text{ Stable crack growth} \\ K > K_c & \text{ Unstable crack growth} \end{aligned}$$

### 2.1.3 Crack Modes and Mode Mixity

This section is based on Andreasen (2011). So far in the discussion only a specific type of crack has been discussed, but generally in fracture mechanics, three basic types of cracks exist - modes I, II and III cracks. The three modes for an isotropic material are shown schematically in Figures 2.3a, 2.3b, and 2.3c, and it may be recognised that the cracks discussed so far are mode I cracks. The three modes are characterised by symmetries as:

$$\text{Mode I: } u_1^+ = u_1^-, \quad u_2^+ = u_2^-, \quad u_3^+ = -u_3^-$$

$$\text{Mode II: } u_1^+ = -u_1^-, \quad u_2^+ = u_2^-, \quad u_3^+ = u_3^-$$

$$\text{Mode III: } u_1^+ = u_1^-, \quad u_2^+ = -u_2^-, \quad u_3^+ = u_3^-$$

A different value of the critical energy release rate and critical stress intensity factor can in principle be associated with each crack mode. E.g. the three

critical energy release rates  $G_{Ic}$ ,  $G_{IIc}$ , and  $G_{IIIc}$  and similarly the stress intensity factors  $K_{Ic}$ ,  $K_{IIc}$ , and  $K_{IIIc}$  exist. An arbitrary crack can be characterised by its components in each of the three basic crack modes by specifying either energy release rates  $G_I$ ,  $G_{II}$ , and  $G_{III}$  or stress intensity factors  $K_I$ ,  $K_{II}$ , and  $K_{III}$ . Often in plane problems, where  $K_{III}$  must be zero, the mode mixity parameter given below is typically used to specify the crack mode (Andreasen, 2011).

$$\psi = \arctan \left( \frac{K_{II}}{K_I} \right) \quad (2.1.12)$$

Now that the basic concepts and terms of the LEFM have been introduced, simplified analytical expressions for the energy release rates for different commonly used test specimens will be derived. The results will serve to provide reference values for benchmarking examples, but they will also help to show, how the treated test specimens can be used to measure the critical energy release rates and mode interactions for different materials.

## 2.2 Test Specimens

In this section approximate analytical expressions for the energy release rates and mode interactions for the DCB, ENF and MMB tests will be derived, and it will be discussed how these results can be used to measure the material fracture toughnesses. Furthermore expressions for the load-displacement curves are derived. The derivations in this section are based on Goyal (2002), Mi et al. (1998) and Reeder and Jr. (1990).

### 2.2.1 The DCB Test

The Double Cantilever Beam (DCB) test is often used to measure the mode I fracture toughness ( $G_{Ic}$ ,  $K_{Ic}$ ). In this subsection it will be treated analytically in order to find an expression for the energy release rate as well as the force-displacement relation for crack propagation in the test. A sketch of the DCB test is shown in Figure 2.4a. In order to calculate the energy release rate in the test, an expression for the total elastic potential is set up, and (2.1.7) is used. In Figure 2.4b a free body diagram over the top arm of the DCB specimen is shown. From this it is seen that the bending moment in the arm,  $M$ , as a

function of  $x$  is:

$$M(x) = Px \quad (2.2.1)$$

Using Bernoulli-Euler beam theory the strain energy in the arm for any crack length,  $a$ , can be found as

$$U_{arm} = \int_0^a \frac{M(x)^2}{2EI} dx = \frac{P^2 a^3}{6EI} \quad (2.2.2)$$

with  $E$  and  $I$  as the Youngs modulus and area moment of inertia respectively. Neglecting local effects close to the crack tip no strain energy will be stored in the uncracked part of the DCB specimen. The two arms, which by symmetry, must have the same strain energy, stores the total strain energy in the DCB specimen. The strain energy is therefore:

$$U = \frac{P^2 a^3}{3EI} \quad (2.2.3)$$

Now the potential of the applied load can be written

$$V = -2Pw \quad (2.2.4)$$

and the total elastic potential then becomes:

$$\Pi = U + V = \frac{P^2 a^3}{3EI} - 2Pw \quad (2.2.5)$$

Using the second Castigliano theorem, the tip displacements can be found as:

$$0 = \frac{\partial \Pi}{\partial P} = \frac{2Pa^3}{3EI} - 2w \quad (2.2.6)$$

$$w = \frac{Pa^3}{3EI} \quad (2.2.7)$$

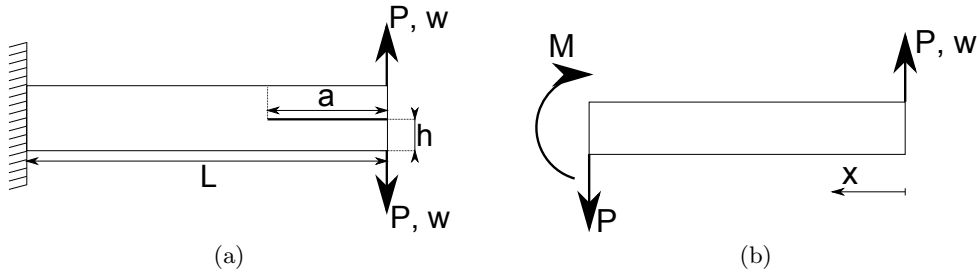


Figure 2.4: a) Sketch of the DCB specimen and b) free body diagram over the top arm of the specimen.

Inserting this displacement into (2.2.5), and using (2.1.7), the energy release rate for the DCB specimen is obtained as:

$$G = -\frac{1}{t} \frac{\partial \Pi}{\partial a} = \frac{P^2 a^2}{tEI} \quad (2.2.8)$$

In the above,  $t$  is of course the specimen thickness. For a propagating crack the load-displacement relation can be found by setting  $G = G_{Ic}$ , solving for  $a$  and substituting this into (2.2.7) resulting in:

$$w = \frac{P}{3EI} \left( \frac{G_{Ic} EIt}{P^2} \right)^{3/2} \quad (2.2.9)$$

Note that the above solution is approximate since Bernoulli-Euler beam theory has been used, and shear deformation is thus disregarded. Furthermore the beam theory is not valid near the points of load introduction and the crack tip due to the local effects. According to Andreasen (2011) however, the solution is reasonably accurate since it is based on the total elastic potential, which is not severely affected by local effects.

It can be seen from the present discussion how the energy release rate of mode I fracture can be determined by performing a test on the DCB specimen. For instance, for a known crack length, the load at crack propagation can be measured, and the energy release rate can be calculated from (2.2.8).

### 2.2.2 The ENF Specimen

The End Notch Flexure (ENF) specimen is commonly used to measure the fracture toughness of a material in mode II crack propagation ( $G_{IIc}$ ,  $K_{IIc}$ ). A sketch of the specimen is shown in Figure 2.5. Since the derivation of the

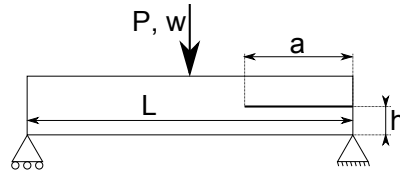


Figure 2.5: Sketch of the ENF specimen.

expression for the energy release rate for this specimen is carried out in the exact same manner as that of the DCB specimen, the derivation will not be shown here. The resulting expressions are however presented since they will

be used later in the thesis. The deflection at the middle of the beam can be found as (Goyal, 2002, p. 192) :

$$w = \frac{P(L^3 + 12a^3)}{384EI} \quad \text{for } a \leq \frac{L}{2} \quad (2.2.10)$$

The energy release rate is found as:

$$G_{II} = \frac{3P^2a^2}{64tEI} \quad (2.2.11)$$

Again setting  $G = G_{IIc}$ , solving for  $a$  and substituting this (2.2.10) an expression for a propogating crack is obtained:

$$w = \frac{P \left( L^3 + 12 \left( \frac{64tEI G_{IIc}}{3P^2} \right)^{3/2} \right)}{384EI} \quad \text{for } a \leq \frac{L}{2} \quad (2.2.12)$$

### 2.2.3 The MMB Specimen

The Mixed Mode Bending (MMB) specimen is used to measure the interaction between the mode I and mode II fracture mechanisms. The test was invented by Reeder and Jr. (1990) and the purpose was to make a test that was suitable for the same specimens used for the ENF and DCB test. A sketch of the specimen is shown in Figure 2.6a, and in Figure 2.6b it is shown how the load is practically applied to the specimen. Considering the two figures, it can easily be shown that the force applied to the lever,  $P$ , is split between the two

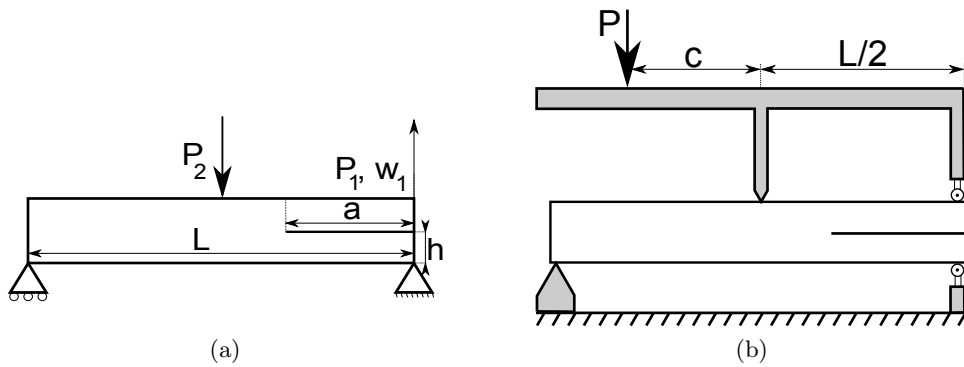


Figure 2.6: a) Sketch of the MMB specimen and b) the way the load is applied to the specimen.

forces transmitted to the specimen,  $P_1$  and  $P_2$ , as:

$$P_1 = \frac{2c}{L}P \quad (2.2.13)$$

$$P_2 = \frac{2c+L}{L}P \quad (2.2.14)$$

In order to estimate the energy release rates in mode I and mode II respectively, the superposition principle is exploited. For this purpose, Figure 2.7 is considered. From the figure it is seen that the MMB specimen can be

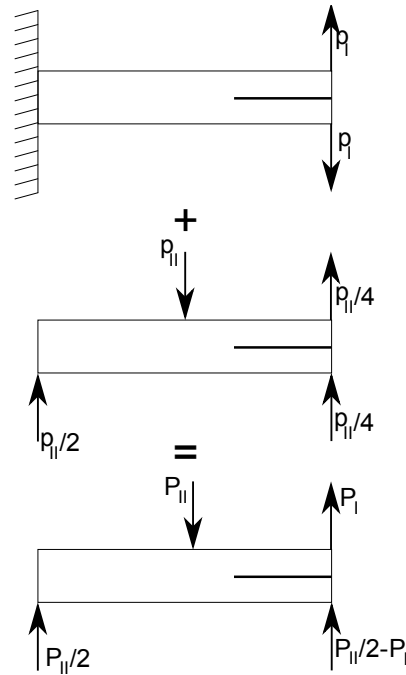


Figure 2.7: How the superposition is considered for the MMB energy release rate solution.

represented as a superposition of the DCB and ENF specimen. The following equations in the forces can be set up:

$$P_1 = \frac{2c}{L}P = p_I + \frac{p_{II}}{4} \quad (2.2.15)$$

$$P_2 = \frac{2c+L}{L}P = p_{II} \quad (2.2.16)$$

These equations can then be solved for the unknown mode I (DCB) forces,  $p_I$ , and the mode II (ENF) force,  $p_{II}$ :

$$p_I = \frac{6c - L}{4L}P \quad (2.2.17)$$

$$p_{II} = \frac{2c + L}{L}P \quad (2.2.18)$$

These forces can then be used directly in equations (2.2.8) and (2.2.11) to provide the mode I and mode II energy release rates for the MMB specimen:

$$G_I = \frac{(6c - L)^2}{16} \frac{P^2 a^2}{L^2 t EI} \quad (2.2.19)$$

$$G_{II} = \frac{3(2c + L)^2}{64} \frac{P^2 a^2}{L^2 t EI} \quad (2.2.20)$$

From this it can be seen that by varying the distance  $c$ , the ratio between the energy release rate in modes I and II can be changed, and that the ratio is:

$$\theta = \frac{G_I}{G_{II}} = \frac{4}{3} \left( \frac{6c - L}{2c + L} \right)^2, \quad c \geq \frac{L}{6} \quad (2.2.21)$$

where  $c = L/6$  gives a ratio of zero, i.e. pure mode II, while an infinite lever arm  $c$  gives a ratio of 12. Thus the MMB test can be used for ratios within this interval. The load-displacement relation can, by referring to Figure 2.6, be expressed through the lever load  $P$  and the tip displacement  $w_1$ , by noting that  $w_1$  depends only on the DCB superposition load  $p_I$ . This can be used to set up the load-displacement relation by using the DCB expression (2.2.7) with  $p_I$ , and furthermore substituting the relation between  $p_I$  and lever load  $P$ :

$$w_1 = \frac{2p_I a^3}{3EI} = \frac{2a^3}{3EI} \left( \frac{6c - L}{4L} \right) P \quad (2.2.22)$$

where the factor of two is due to a different definition of  $w_1$ , as shown on Figure 2.6a, as compared to  $w$  in the DCB test. To find the relation after propagation, the total energy release rate is set equal to the critical such that  $G_c = G_I + G_{II}$ . If solved for  $a$  the following is found:

$$a = \sqrt{\frac{64EIbG_c L^2}{P^2 (7L^2 - 36Lc + 156c^2)}} \quad (2.2.23)$$

which can then be substituted into (2.2.22). The presented expressions are only viable for  $a \leq L/2$ . Determination of  $G_{IIIc}$  will not be described in this thesis, since this property is often regarded as equal to  $G_{IIc}$  (Goyal, 2002, p. 10).

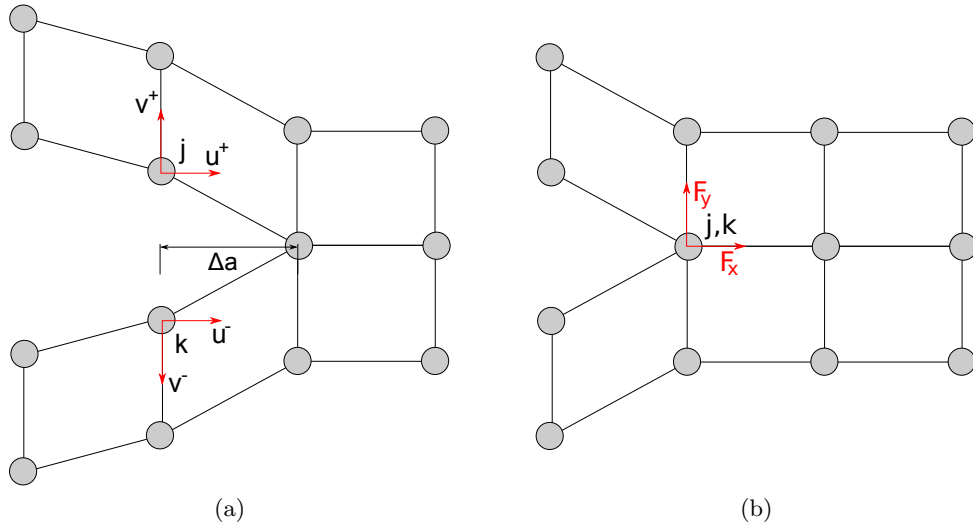


Figure 2.8: Sketch of the principle in CCM showing a) the first FE solution and b) the second FE solution.

### 2.3 LEFM in the FEM

Several methods for using LEFM in the FEM exist. These include methods for estimating both the energy release rate as well as the stress intensity factor. In this section the Crack Closure Method (CCM), which is used to estimate the energy release rate in FEM, is presented in rough terms. This is done in order to clarify some of the advantages and disadvantages in numerical use of LEFM. The following is based on Lindgaard (2011a).

The principle in CCM is illustrated by Figures 2.8a and 2.8b. The method is based on the assumption, that the energy released when the crack grows a short distance, is equal to the amount of work needed to close the crack by the same amount. This is used in the CCM in the FEM by carrying out two analyses based on the same initial geometry. The initial geometry must model the crack and of course the load situation under which the energy release rate is needed. Now the model is solved in order to obtain the result sketched in Figure 2.8a. From these results the displacements  $u^+$  and  $v^+$  for node  $j$ , and  $u^-$  and  $v^-$  for node  $k$  is recorded. Now the model is modified by connecting nodes  $j$  and  $k$  by an MPC. The model is solved, and the result sketched in Figure 2.8b is obtained. From this the reaction forces between nodes  $k$  and  $j$ ,  $F_x$

and  $F_y$ , are recorded. Now the energy release rate is estimated as (Lindgaard, 2011a):

$$G_{tot} = G_I + G_{II} = \frac{F_x(u^+ - u^-)}{2t\Delta a} + \frac{F_y(v^+ - v^-)}{2t\Delta a} \quad (2.3.1)$$

In the above  $\Delta a$  is the difference in crack length between the two analyses, and  $t$  is the model thickness. As already mentioned, variations of the described method, and other methods for estimating the energy release rate using FEM exists, but it should be noted that the CCM is representative for the methods with respect to the model requirements.

From the discussion above a few important conclusions about the use of LEFM in the FEM can be drawn. A major advantage is that linear FEA's are sufficient. This is especially important when dealing with complex FE models, for which a non-linear analysis will be too time consuming. A drawback is that existing knowledge or a reasonable assumption of the crack geometry, size and location in the structure in question is needed, in order to apply LEFM. This is due to the fact that LEFM only provides predictions concerning crack growth, not crack initiation.

## 2.4 Conclusion

The basic concepts and terms in the linear elastic fracture mechanics have been introduced. With a focus on the energy release rate, simple analytical uses of the theory have been illustrated on some of the most common tests used for measuring fracture toughnesses of materials. Furthermore it has been illustrated how LEFM can be used within the framework of the FEM. From this it was found, that an advantage of LEFM in the FEM is that it requires only linear analyses, which of course saves computational time when compared to non-linear analyses. Among drawbacks it was found that LEFM provides no means of predicting crack initiation, and thus a preexisting crack needs to be modeled to predict crack propagation. The found disadvantages provides a motivation for considering alternative methods for predicting fracture failure, especially in structures and details where existing microcracks are hard to detect.



## Chapter 3

# Modelling the Cohesive Zone

In this chapter the theory of cohesive zone modelling necessary for implementing a CZ element will be treated. First the concept of the cohesive zone is briefly introduced. Following this the necessary theoretical constituents required to go from the weak form of the problem to an FE formulation are presented.

### 3.1 The Cohesive Zone Concept

The cohesive zone is another way to consider cracks. The Cohesive zone concept was proposed by Barenblatt (1961), and the intention was to describe the fracture process more realistically, such that the stress singularities, found in LEFM, do not arise. The cohesive zone model divides a crack into two parts. These two parts of the crack are shown in Figure 3.1, and are denoted as the physical crack and the cohesive zone. The cohesive zone is idealised

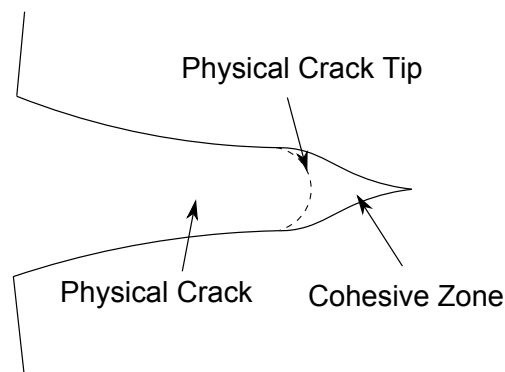


Figure 3.1: Distinction of the two different zones in the crack.

as two cohesive surfaces which are held together by tractions. According to the model proposed by Barenblatt (1961) the traction stems from atomic bonding forces. The tractions in the cohesive zone are related to the relative displacements of the cohesive surfaces through a constitutive law. A physical crack extension occurs when the relative displacements in the cohesive zone reach a critical value. A sketch of a cohesive zone with tractions,  $T$ , as a function of separation distance,  $\Delta$ , is shown on Figure 3.2. In the original

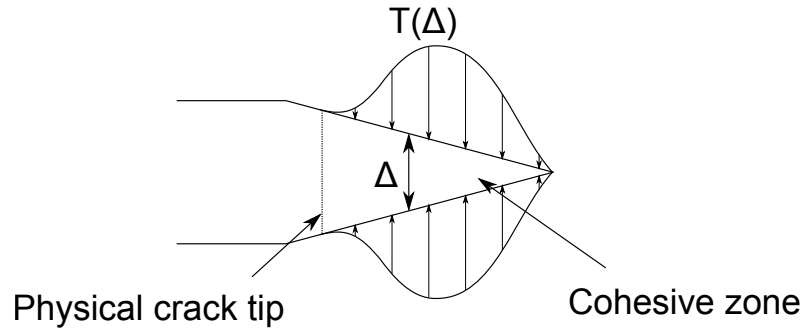


Figure 3.2: A cohesive zone with tractions,  $T$ , as a function of separation distance. Note that the crack shape is not realistic.

model proposed by Barenblatt (1961), the tractions acting on the cohesive surfaces should have a size and distribution such that the infinite stresses found in LEFM are cancelled out (Sun and Jin, 2011, p. 229). Since the cohesive zone model does not build upon a pure continuum formulation as LEFM, a connection between the cohesive zone model and the continuum formulation must be made. This chapter serves to do so.

### 3.2 Approach for Combining CZM with the Continuum

The connection between CZM and the continuum will be established in the framework of the FEM. According to Lindgaard (2011b) the FEM is the most universal numerical method for solution of boundary value problems expressed by Partial Differential Equations (PDEs). Therefore the goal of this chapter is to have an FE formulation that includes the cohesive zone. The continuum formulation of a structural problem is given by a set of coupled PDEs and algebraic equations describing how stress and strain are distributed in the continuum due to the applied boundary conditions. The cohesive zone can be

### 3.2. APPROACH FOR COMBINING CZM WITH THE CONTINUUM 27

incorporated in the continuum formulation by applying the cohesive tractions as boundary conditions. In order to solve this coupled system by the use of the FEM, the governing PDE's along with boundary conditions have to be stated in their weak formulation. When the weak formulation of the problem has been derived, it is possible to discretise it into a finite number of elements. Since there will be solved for the displacements, and the functional turns out to be non-linear in these terms, the element formulation must be made, such that it conforms with the needed formulation used by non-linear solvers. When the discretisation is set up it is seen that two types of elements will be present. One element will be a continuum type element and the other a CZM type element. The element formulation for the continuum will not be carried out

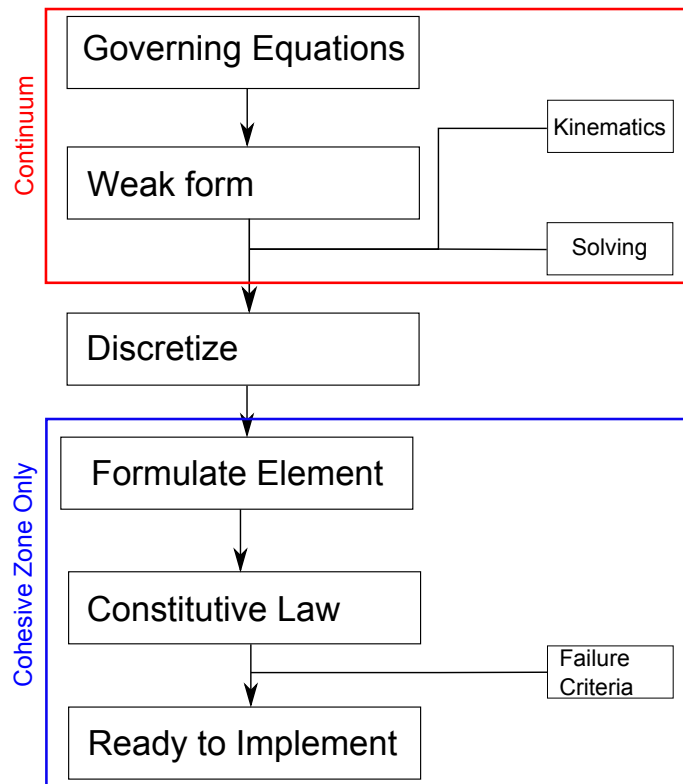


Figure 3.3: Flowchart for the procedure of formulating a CZ element.

since commercial implementations of these elements will be used. Only the part regarding the cohesive zone is brought further, such that finally the CZ element can be formulated. In order to formulate the CZ element, kinematics and a constitutive law for the element will be introduced in this chapter.

The purpose of the kinematics is to obtain relative displacements of the crack surfaces from global displacements. The purpose of the constitutive law is to relate the tractions acting on the crack surfaces to the relative displacements. A flowchart of the approach taken, in order to derive the formulation of a CZ element, is shown in Figure 3.3.

### 3.3 CZM Formulated as Boundary Value Problem

The boundary value problem for a structural component containing a crack is shown in Figure 3.4. As seen from the figure the problem is similar to a

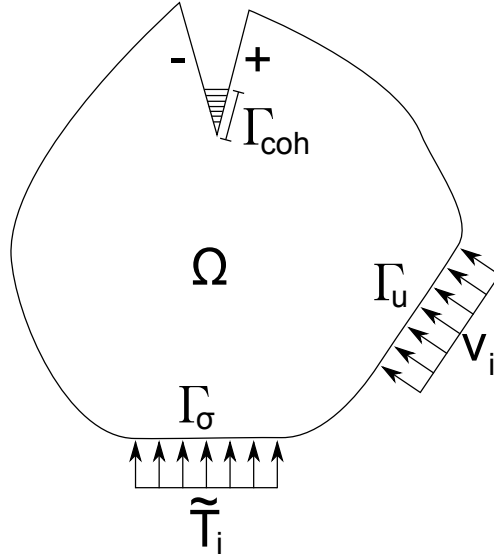


Figure 3.4: Illustration of the boundary value problem.

standard structural problem, if the crack is disregarded. This means that in the domain  $\Omega$  the well known partial differential/algebraic equations regarding geometry, constitutive relations, and equilibrium should be fulfilled. The governing PDE's and their derivation can be found in e.g. Kildegaard (2006) and are in the following shown using Einstein notation. The equilibrium equations can be derived as:

$$\sigma_{ij,j} + b_i = 0 \quad \text{in} \quad \Omega \quad (3.3.1)$$

where (3.3.1)  $b_i$  is the body force and  $\sigma_{ij}$  is the stress tensor. The geometric relationship, which relates strains to displacements, can be expressed through

the nonlinear Green-Lagrange strain tensor:

$$\epsilon_{ij} = \frac{1}{2} (u_{i,j} + u_{j,i} + u_{k,i}u_{k,j}) \quad \text{in } \Omega \quad (3.3.2)$$

where the nonlinear part is included, since large strains are often encountered when cracks develop (Goyal, 2002). Assuming a linear stress-strain relation Hookes law is given by:

$$\sigma_{ij} = C_{ijkl}\epsilon_{kl} \quad \text{in } \Omega \quad (3.3.3)$$

Still disregarding the crack, the boundary values are given by:

$$\sigma_{ij}n_j = \tilde{T}_i \quad \text{on } \Gamma_\sigma \quad (3.3.4)$$

$$u_i = v_i \quad \text{on } \Gamma_u \quad (3.3.5)$$

Taking the crack into account, a traction boundary condition is introduced over the boundary represented by  $\Gamma_{coh}$ . Applying Newtons third law and denoting the two crack surfaces by + and - respectively, the boundary condition over the boundary  $\Gamma_{coh}$  can be written

$$\sigma_{ij}^+n_j^+ = T_i^+ = -T_i^- = -\sigma_{ij}^-n_j^- \quad \text{on } \Gamma_{coh} \quad (3.3.6)$$

From (3.3.1) to (3.3.6) it should be noted, that the boundary value problem is a mixed boundary value problem, since both displacements and tractions are prescribed. Letting the crack propagate in the structure, such that the the surface defined by  $\Gamma_c$  is created (as seen in Figure 3.5), the mixed boundary value problem becomes a moving mixed boundary value problem. Introducing the boundary  $\Gamma_c$  means, that the boundary condition given by (3.3.6) must be fulfilled on  $\Gamma_c$  instead of only  $\Gamma_{coh}$ .

### 3.4 Weak Formulation

In order to solve the boundary value problem described in section 3.3 using FEM, the problem is converted to a weak formulation using the principle of virtual work. The principle of virtual work, as opposed to e.g. the principle of total potential energy, is used since it is also valid for nonelastic continua (Shames and Dym, 1985). The following is based on Goyal (2002).

As shown on Figure 3.5, the boundary  $\Gamma_c$  denotes the interface in which the

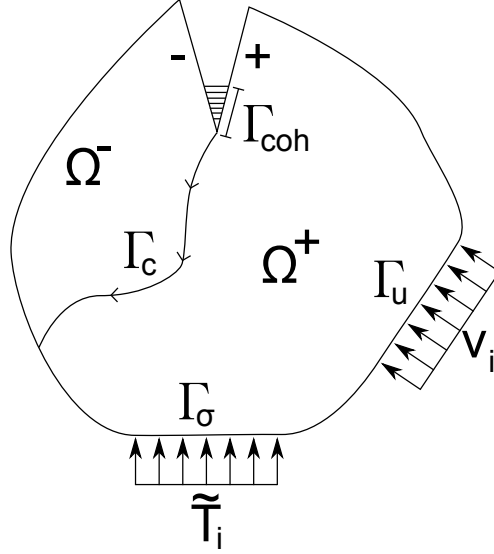


Figure 3.5: The domain divided into two parts separated by the predefined interface,  $\Gamma_c$ , where the crack is allowed to propagate.

crack is allowed to propagate. If the crack is opened, a displacement jump is introduced in the domain  $\Omega$ . This internal boundary restricts displacement variations, and hence variations of displacements cannot be chosen arbitrarily within the domain. A way to work around this, is to divide the domain  $\Omega$  into two subdomains  $\Omega^+$  and  $\Omega^-$ , as seen on Figure 3.5, and formulating the crack opening as a boundary condition. Applying the principle of virtual work on each subdomain the following is obtained:

$$\int_{\Omega^+} b_i \delta u_i d\Omega + \int_{\partial\Omega^+} \tilde{T}_i \delta u_i d\Gamma + \int_{\Gamma_c^+} T_i^+ \delta u_i^+ d\Gamma = \int_{\Omega^+} \sigma_{ij} \delta E_{ij} d\Omega \quad (3.4.1)$$

$$\int_{\Omega^-} b_i \delta u_i d\Omega + \int_{\partial\Omega^-} \tilde{T}_i \delta u_i d\Gamma + \int_{\Gamma_c^-} T_i^- \delta u_i^- d\Gamma = \int_{\Omega^-} \sigma_{ij} \delta E_{ij} d\Omega \quad (3.4.2)$$

Note that for now the linear Cauchy<sup>1</sup> strain ( $E_{ij}$ ) and stress ( $\sigma_{ij}$ ) definitions are used in the equations. Adding (3.4.2) to (3.4.1) and making use of the two boundary conditions on  $\Gamma_c$ , which in (3.3.6) were equated due to Newton's 3rd law, the weak formulation can be stated in one expression given as:

$$\int_{\Omega} b_i \delta u_i d\Omega + \int_{\partial\Omega} \tilde{T}_i \delta u_i d\Gamma = \int_{\Omega} \sigma_{ij} \delta E_{ij} d\Omega - \int_{\Gamma_c^+} T_i^+ (\delta u_i^+ - \delta u_i^-) d\Gamma \quad (3.4.3)$$

At this point a midplane  $\bar{\Gamma}$  is introduced. This plane lies in the middle between the two crack surfaces, and in the case of no displacement difference between

<sup>1</sup>The Lagrange-Green strain tensor in (3.3.2) without the nonlinear terms.

$u_i^-$  and  $u_i^+$  it is simply  $\Gamma_c$ . Using the  $+$  surface as reference, the traction on the midplane by Newtons 3rd law is given as:

$$\bar{T}_i = -T_i^+ \quad (3.4.4)$$

as also shown on Figure 3.6. Substituting this into (3.4.3) the following is

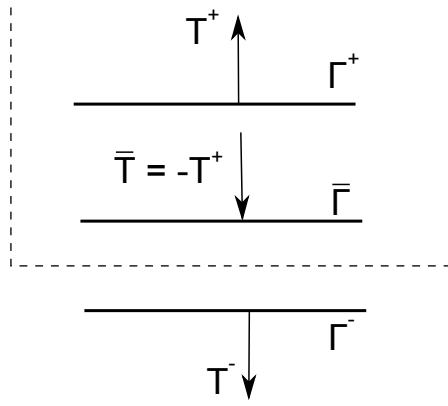


Figure 3.6: Introduction of the midplane and the midplane tractions with the  $+$  surface as reference.

obtained:

$$\int_{\Omega} b_i \delta u_i d\Omega + \int_{\partial\Omega} \tilde{T}_i \delta u_i d\Gamma = \int_{\Omega} \sigma_{ij} \delta E_{ij} d\Omega + \int_{\bar{\Gamma}_c} \bar{T}_i (\delta u_i^+ - \delta u_i^-) d\Gamma \quad (3.4.5)$$

However the constitutive relationship of the crack is formulated with respect to the tangential and normal direction of the midplane. Due to this a local coordinate system is defined with its axes tangential and normal to the midsurface. Transformation from the local to the global coordinate system is done through a rotation matrix,  $R_{ij}$ . How this is defined will be presented in the section 3.5. Using this the midplane tractions can be written as  $\bar{T}_i = R_{ij} T_j$ , which, when substituted, yields:

$$\int_{\Omega} b_i \delta u_i d\Omega + \int_{\partial\Omega} \tilde{T}_i \delta u_i d\Gamma = \int_{\Omega} \sigma_{ij} \delta E_{ij} d\Omega + \int_{\bar{\Gamma}_c} R_{ij} T_j (\delta u_i^+ - \delta u_i^-) d\Gamma \quad (3.4.6)$$

where  $T_j$  are tractions in the local coordinate system. Since crack propagation problems might introduce large deformation gradients, the Green-Lagrange strain tensor (3.3.2) needs to be used to describe the strain in the material. When the Green-Lagrange strain tensor is used, the stress definition must be the second Piola-Kirchhoff Stress,  $S$ , in order for the functional to be work

consistent (Goyal, 2002, p. 27). The second Piola-Kirchhoff stress is defined according to the reference volume,  $\Omega^0$ , such that (3.4.6) becomes:

$$\int_{\Omega} b_i \delta u_i d\Omega + \int_{\partial\Omega} \tilde{T}_i \delta u_i d\Gamma = \int_{\Omega^0} S_{ij} \delta \epsilon_{ij} d\Omega + \int_{\tilde{\Gamma}_c} R_{ij} T_j (\delta u_i^+ - \delta u_i^-) d\Gamma \quad (3.4.7)$$

This is the weak form for the given boundary value problem. In the following section the kinematics needed to establish the rotation matrix  $R_{ij}$  will be described.

### 3.5 Kinematics

The purpose of this section is to arrive at the rotation matrix, used in (3.4.6), which transforms properties from a local curvilinear coordinate system on the mid surface into the global coordinate system. In Figure 3.7 an illustration of the way the transformation works is seen. In this section three different surfaces are considered: +, - and a mid surface denoted with an overbar. These surfaces are considered in two configurations: An undeformed and a deformed configuration. In the undeformed configuration the surfaces are coincident and can thus be represented by a single parametric surface which is denoted  $x_i^0[\xi, \eta]$ , where square brackets denotes "function of". In the deformed configuration the + and - surfaces are denoted by two parametric functions,  $x_i^{\pm}[\xi, \eta]$ , as shown on Figure 3.8.

The undeformed and deformed upper and lower surfaces are related respectively through the displacements  $u_i^+$  and  $u_i^-$ . This is also shown on

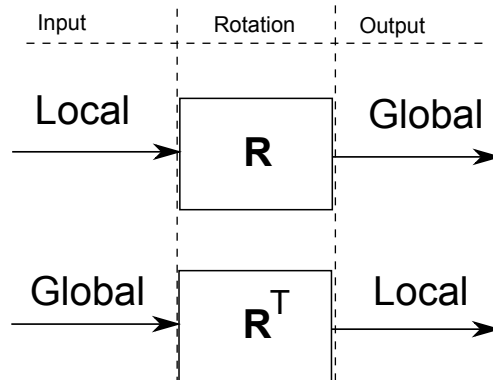


Figure 3.7: Overview of how the transformation matrix maps properties.

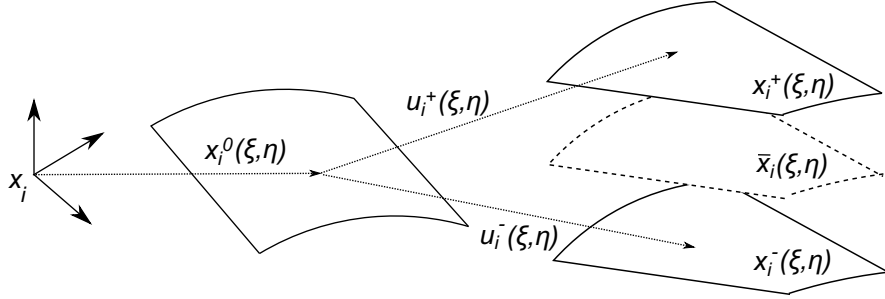


Figure 3.8: Two initially coincident surfaces undergoing deformation, such that an opening displacement inbetween is created.

Figure 3.8 and can be written

$$x_i^\pm = x_i^0 + u_i^\pm \quad (3.5.1)$$

Then the position of the midplane,  $\bar{x}_i$ , can be written as

$$\bar{x}_i = \frac{1}{2} (x_i^+ + x_i^-) = x_i^0 + \frac{1}{2} (u_i^+ + u_i^-) \quad (3.5.2)$$

Vectors tangential to the plane can be found by partial differentiation with regards to the parameters  $\xi$  and  $\eta$  according to e.g. Anton et al. (2012) as shown on Figure 3.9. Using this two vectors tangential to the plane can be found as:

$$\mathbf{e}_\xi = \frac{\partial \bar{x}_i}{\partial \xi} \quad , \quad \mathbf{e}_\eta = \frac{\partial \bar{x}_i}{\partial \eta} \quad (3.5.3)$$

These vectors can then be used to find the normal unit vector and the differential area of the deformed surface. The normal unit vector becomes:

$$\hat{\mathbf{e}}_3 = \frac{\mathbf{e}_\xi \times \mathbf{e}_\eta}{|\mathbf{e}_\xi \times \mathbf{e}_\eta|} \quad (3.5.4)$$

The differential surface area is given by (Anton et al., 2012):

$$d\bar{S} = |\mathbf{e}_\xi \times \mathbf{e}_\eta| d\xi d\eta \quad (3.5.5)$$

where  $|\mathbf{e}_\xi \times \mathbf{e}_\eta|$  is the area scaling denoted  $J$ , to be used later. The vectors  $\mathbf{e}_\xi$  and  $\mathbf{e}_\eta$  are not necessarily orthogonal. To ensure an orthogonal local coordinate system,  $\mathbf{e}_\eta$  is discarded. The unit vector from  $\mathbf{e}_\xi$  is,

$$\hat{\mathbf{e}}_1 = \frac{\mathbf{e}_\xi}{|\mathbf{e}_\xi|} \quad (3.5.6)$$

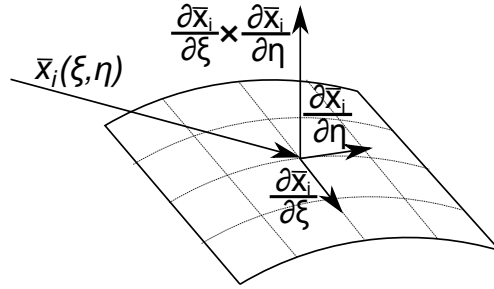


Figure 3.9: Vectors tangential to the surface found by partial differentiation. A vector normal to the surface can be found as the cross product.

and the last orthogonal unit vector is then the cross product of the two already defined unit vectors:

$$\hat{\mathbf{e}}_2 = \hat{\mathbf{e}}_1 \times \hat{\mathbf{e}}_3 \quad (3.5.7)$$

The unit vectors form a rotation matrix that relates the orientation of the local coordinate system of the midsurface,  $\bar{S}$ , to the orientation of the global coordinate system (Turon, 2006),

$$R_{ij} = \mathbf{R} = [\hat{\mathbf{e}}_1, \hat{\mathbf{e}}_2, \hat{\mathbf{e}}_3] \quad (3.5.8)$$

and opening displacements in the local coordinate system,  $\Delta$ , can thus be written in terms of the displacements in the global coordinate system as

$$\Delta = \mathbf{R}^T (\mathbf{u}^+ - \mathbf{u}^-) \quad (3.5.9)$$

It should be noted, that due to the local nature of the formulation of the kinematics, Mode II and Mode III relative displacements cannot be distinguished.

### 3.6 Solvers

The functional given in (3.4.7) is not a linear functional in the displacements  $u_i$ . In order to solve this functional using the FEM, an iterative numerical solution routine has to be used. Rewriting the functional given by (3.4.7) and

denoting the residual with  $I$  gives

$$\begin{aligned} I[u] = & \left( \int_{\Omega^0} S_{ij} \delta \epsilon_{ij} d\Omega + \int_{\bar{\Gamma}_c} R_{ij} T_j (\delta u_i^+ - \delta u_i^-) d\Gamma \right) \\ & - \left( \int_{\Omega} b_i \delta u_i d\Omega + \int_{\partial\Omega} \tilde{T}_i \delta u_i d\Gamma \right) = \delta W^{int}[u] - \delta W^{ext}[u] = 0 \end{aligned} \quad (3.6.1)$$

When an external load is applied (taking a load step), the part of the functional containing  $\delta W^{ext}$  changes, and the functional is no longer zero, which by virtue of the virtual displacement theorem means, that equilibrium is no longer satisfied. The problem is therefore turned into a root finding problem. There are several ways to solve a root finding problem. The most widely used root finding methods used in the FEM are methods, which build upon the classical Newton-Raphson method. The Newton-Raphson Method (NRM) introduces the concept of a tangent stiffness matrix, and therefore the NRM will be described here.

**Newton-Raphson Method** The Newton-Raphson method can be explained in terms of continuous functions, even though it has to be implemented in a discrete way. Hence, the displacement field,  $u$ , in the following is a continuous function, which is valid over the entire domain of computation. Taking the first variation of the functional in (3.6.1) the following is obtained:

$$I[u^{k+1}] = I[u^k] + \left. \frac{\partial}{\partial u} I[u] \right|_{u^k} \delta u^k = 0 \quad (3.6.2)$$

where  $\delta u^k$  is the displacement increment and represents the change in displacements between consecutive iterations. Note that the superscript denotes the iteration number. Rearranging the following is obtained:

$$\left. \frac{\partial}{\partial u} I[u] \right|_{u^k} \delta u^k = -I[u^k] \quad (3.6.3)$$

In implementing the method, the displacement field is described by a finite number of DOF. When this is done, (3.6.3) represents a set of linear equations in the DOF. This is shown in section 3.7. The term  $\left. \frac{\partial}{\partial u} I[u] \right|_{u^k}$  represents the so-called tangent stiffness. It should be noted that, before the solution process can be started, a starting guess for the displacement field is needed. The solution procedure for the Newton-Raphson Method is described in the list below and is sketched in Figure 3.10.



load-displacement curve between points B and C is sought, a solution method called the arc-length method can be used. The arc-length method is capable of capturing negative slopes of the load displacement curve. This is because it is an equilibrium path tracing algorithm, that can vary both loads and displacements. For further information see (ANSYS, Inc, 2010, sec. 15.13.6).

### 3.7 Discretisation

In section 3.6, the solution procedure for the non-linear functional was discussed, and the weak formulation was rearranged to a residual:

$$I[u] = \underbrace{\left( \int_{\Omega^0} S_{ij} \delta \epsilon_{ij} d\Omega + \int_{\bar{\Gamma}_c} R_{ij} T_j (\delta u_i^+ - \delta u_i^-) d\Gamma \right)}_{\delta W^{int}} - \underbrace{\left( \int_{\Omega} b_i \delta u_i d\Omega + \int_{\partial\Omega} \tilde{T}_i \delta u_i d\Gamma \right)}_{\delta W^{ext}} = 0 \quad (3.7.1)$$

Now the domain is discretised into a finite number of elements. Doing this the integrations can be done over each element and then summed up afterwards. However four different domains currently exist in the formulation, i.e.  $\Omega^0$ ,  $\Omega$ ,  $\Gamma$ , and  $\bar{\Gamma}_c$ . The external virtual work consists of an integral in  $\Omega$  and  $\Gamma$  which for the associated element becomes:

$$\delta W^{ext, e_k} = \int_{e_k} b_i \delta u_i d\Omega \quad (3.7.2)$$

$$\delta W^{ext, be_k} = \int_{be_k} \tilde{T}_i \delta u_i d\Gamma \quad (3.7.3)$$

where  $e_k$  denotes internal element in  $\Omega$  number  $k$  and  $be_k$  boundary element in  $\Gamma$  number  $k$ . In this way the external virtual work can be written as the sum over all elements:

$$\delta W^{ext} = \sum_{k=1}^{n_e} \delta W^{ext, e_k} + \sum_{k=1}^{n_{be}} \delta W^{ext, be_k} \quad (3.7.4)$$

where the  $n$ 's denote 'number of'. In the same way the internal virtual work can be written:

$$\delta W^{int, e_k} = \int_{e_k^0} S_{ij} \delta \epsilon_{ij} d\Omega \quad (3.7.5)$$

$$\delta W^{int, ce_k} = \int_{ce_k} R_{ij} T_j (\delta u_i^+ - \delta u_i^-) d\Gamma \quad (3.7.6)$$

where  $ce_k$  denotes cohesive element on  $\bar{\Gamma}_c$  number  $k$ , and  $e_k^0$  denotes the domain of integration for the undeformed geometry of element  $k$ . Similarly by summing up, the total internal virtual work can be written:

$$\delta W^{int} = \sum_{k=1}^{n_e} \delta W^{int,e_k} + \sum_{k=1}^{n_{ce}} \delta W^{int,ce_k} \quad (3.7.7)$$

Writing the full discretised weak form and rearranging a bit:

$$I = \sum_{k=1}^{n_e} (\delta W^{int,e_k} - \delta W^{ext,e_k}) - \sum_{k=1}^{n_{be}} \delta W^{ext,be_k} + \sum_{k=1}^{n_{ce}} \delta W^{int,ce_k} = 0 \quad (3.7.8)$$

This describes that for the sum of all elements, i.e. the full structure, the internal virtual work must equal the external virtual work. However this scalar equation does not reveal much about what happens in each element. Writing out the variations in the expression with respect to the displacements, the following is obtained:

$$\begin{aligned} I = \sum_{k=1}^{n_e} \left( \frac{\partial W^{int,e_k}}{\partial u_j} \delta u_j - \frac{\partial W^{ext,e_k}}{\partial u_j} \delta u_j \right) \\ - \sum_{k=1}^{n_{be}} \frac{\partial W^{ext,be_k}}{\partial u_j} \delta u_j + \sum_{k=1}^{n_{ce}} \frac{\partial W^{int,ce_k}}{\partial u_j} \delta u_j = 0 \end{aligned} \quad (3.7.9)$$

The problem is still posed in an exact fashion above. In order to prepare the problem for numerical treatment, it must be restated in a finite number of degrees of freedom (DOF). In order to do this, the displacement field is now assumed to be described by continuous functions of a finite number of DOF,  $q_i$ . The variation in (3.7.9) can therefore further be written out as:

$$\begin{aligned} I = \sum_{k=1}^{n_e} \left( \frac{\partial W^{int,e_k}}{\partial u_j} \frac{\partial u_j}{\partial q_i} \delta q_i - \frac{\partial W^{ext,e_k}}{\partial u_j} \frac{\partial u_j}{\partial q_i} \delta q_i \right) \\ - \sum_{k=1}^{n_{be}} \frac{\partial W^{ext,be_k}}{\partial u_j} \frac{\partial u_j}{\partial q_i} \delta q_i + \sum_{k=1}^{n_{ce}} \frac{\partial W^{int,ce_k}}{\partial u_j} \frac{\partial u_j}{\partial q_i} \delta q_i \\ = \left( \sum_{k=1}^{n_e} \left( \frac{\partial W^{int,e_k}}{\partial u_j} \frac{\partial u_j}{\partial q_i} - \frac{\partial W^{ext,e_k}}{\partial u_j} \frac{\partial u_j}{\partial q_i} \right) \right. \\ \left. - \sum_{k=1}^{n_{be}} \frac{\partial W^{ext,be_k}}{\partial u_j} \frac{\partial u_j}{\partial q_i} + \sum_{k=1}^{n_{ce}} \frac{\partial W^{int,ce_k}}{\partial u_j} \frac{\partial u_j}{\partial q_i} \right) \delta q_i = 0 \end{aligned} \quad (3.7.10)$$

From the above, and from the definition of the principle of virtual work, it is seen that that the term in parenthesis must be the total force on nodal DOF

number  $i$ , which must be zero since the nodal variation,  $\delta q_i$  is arbitrary. The individual terms in the parenthesis can thus be written as force vectors as:

$$I = \left( \sum_{k=1}^{n_e} \left( r_i^{int,e_k} - r_i^{ext,e_k} \right) - \sum_{k=1}^{n_{be_k}} r_i^{ext,be_k} + \sum_{k=1}^{n_{ce_k}} r_i^{int,ce_k} \right) \delta q_i = 0 \quad (3.7.11)$$

In this project the focus is on CZ elements, and all other elements that might exist in an FE model will be modelled using ANSYS' own elements. The internal force vector in the cohesive zone is given as:

$$r_i^{int,ce_k} = \frac{\delta W^{int,ce_k}}{\delta q_i} \quad (3.7.12)$$

Now the approximated displacement field over each element in the cohesive zone can be defined as:

$$u_j = N_{ji} q_i \quad (3.7.13)$$

where  $N_{ji}$  are shape functions that interpolate the displacements, and  $q_i$  is the displacement in nodal DOF number  $i$ . Using this definition, the variation of the displacements becomes:

$$\delta u_j = \frac{\partial u_j}{\partial q_i} \delta q_i = N_{ji} \delta q_i \quad (3.7.14)$$

Inserting this in (3.7.6) the following is obtained:

$$\delta W^{int,ce_k} = \int_{ce_k} R_{ij} T_j N_{ip} (\delta q_p^+ - \delta q_p^-) d\Gamma \quad (3.7.15)$$

$$= \int_{ce_k} R_{ij} T_j N_{ip} \delta q_p^+ d\Gamma - \int_{ce_k} R_{ij} T_j N_{ip} \delta q_p^- d\Gamma \quad (3.7.16)$$

$$= \delta W^{int,ce_k,top} + \delta W^{int,ce_k,bot} \quad (3.7.17)$$

Using (3.7.12) the internal force vectors on the top and bottom DOF in the cohesive zone respectively becomes:

$$r^{int,ce_k,top} = \frac{\delta W^{int,ce_k,top}}{\delta q_p^+} = \int_{ce_k} R_{ij} T_j N_{ip} d\Gamma \quad (3.7.18)$$

$$r^{int,ce_k,bot} = \frac{\delta W^{int,ce_k,bot}}{\delta q_p^-} = - \int_{ce_k} R_{ij} T_j N_{ip} d\Gamma \quad (3.7.19)$$

The cohesive element will be implemented as a linear element with four nodes in the top layer and four nodes in the bottom layer. The isoparametric formulation is chosen for the element, meaning that shape and displacements are interpolated by the same shape functions. Introducing the natural coordinate system  $(\xi, \eta)$ , the linear Lagrangian shape functions are given as:

$$\begin{aligned} N_1 &= \frac{1}{4}(1 - \xi)(1 - \eta) & N_2 &= \frac{1}{4}(1 + \xi)(1 - \eta) \\ N_3 &= \frac{1}{4}(1 + \xi)(1 + \eta) & N_4 &= \frac{1}{4}(1 - \xi)(1 + \eta) \end{aligned} \quad (3.7.20)$$

Introducing the shape function matrix as:

$$[\mathbf{N}] = \begin{bmatrix} N_1 & 0 & 0 & N_2 & 0 & 0 & N_3 & 0 & 0 & N_4 & 0 & 0 \\ 0 & N_1 & 0 & 0 & N_2 & 0 & 0 & N_3 & 0 & 0 & N_4 & 0 \\ 0 & 0 & N_1 & 0 & 0 & N_2 & 0 & 0 & N_3 & 0 & 0 & N_4 \end{bmatrix}$$

the displacements as functions of the natural coordinates can be written in the matrix-vector form as:

$$\{\mathbf{u}^+\} = [\mathbf{N}]\{\mathbf{q}^+\} \quad (3.7.21)$$

$$\{\mathbf{u}^-\} = [\mathbf{N}]\{\mathbf{q}^-\} \quad (3.7.22)$$

where the vectors  $\{\mathbf{q}^+\}$  and  $\{\mathbf{q}^-\}$  are defined as:

$$\{\mathbf{q}^+\} = \{q_{1x}^+, q_{1y}^+, q_{1z}^+, \dots, q_{4z}^+\}^T \quad (3.7.23)$$

$$\{\mathbf{q}^-\} = \{q_{1x}^-, q_{1y}^-, q_{1z}^-, \dots, q_{4z}^-\}^T \quad (3.7.24)$$

With the above definitions and integrating in the natural coordinate system, (3.7.18) and (3.7.19) can be rewritten in matrix-vector notation as:

$$\{\mathbf{r}^{\text{int,ce}_k,\text{top}}\} = \int_{-1}^1 \int_{-1}^1 [\mathbf{N}]^T [\mathbf{R}] \{\mathbf{T}\} J d\xi d\eta \quad (3.7.25)$$

$$\{\mathbf{r}^{\text{int,ce}_k,\text{bot}}\} = - \int_{-1}^1 \int_{-1}^1 [\mathbf{N}]^T [\mathbf{R}] \{\mathbf{T}\} J d\xi d\eta \quad (3.7.26)$$

Note that in the above, the determinant of the Jacobian,  $J$ , is introduced in the integrals to account for the scaling of area when performing the integration in the natural coordinate system.

The discretisation performed in the above does not make the problem immediately solvable, since the problem is nonlinear. As explained in section

3.6 the NRM needs the functional derivative w.r.t. displacement, denoted the tangent stiffness. Since the functional has been discretised, it is no longer a function of the displacement field but instead a function of the finite number of DOF. In order to obtain the tangent stiffness, equations (3.7.25) and (3.7.26) should therefore be differentiated with regards to the DOF. Introducing the vectors of the collected nodal DOF and displacements:

$$\{\mathbf{q}\} = \begin{Bmatrix} \{\mathbf{q}^+\} \\ \{\mathbf{q}^-\} \end{Bmatrix} \quad \text{and} \quad \{\mathbf{u}\} = \begin{Bmatrix} \{\mathbf{u}^+\} \\ \{\mathbf{u}^-\} \end{Bmatrix} \quad (3.7.27)$$

and carrying out the differentiation for the equations connected to the top surface gives:

$$\begin{aligned} \frac{\partial \{\mathbf{r}^{int,ce_k,top}\}}{\partial \{\mathbf{q}\}} = & \int_{-1}^1 \int_{-1}^1 \left( [\mathbf{N}]^T \frac{\partial [\mathbf{R}]}{\partial \{\mathbf{q}\}} \{\mathbf{T}\} J + [\mathbf{N}]^T [\mathbf{R}] \frac{\partial \{\mathbf{T}\}}{\partial \{\mathbf{q}\}} J \right. \\ & \left. + [\mathbf{N}]^T [\mathbf{R}] \{\mathbf{T}\} \frac{\partial J}{\partial \{\mathbf{q}\}} \right) d\xi d\eta \end{aligned} \quad (3.7.28)$$

The terms in (3.7.28) containing  $\frac{\partial [\mathbf{R}]}{\partial \{\mathbf{q}\}}$  and  $\frac{\partial J}{\partial \{\mathbf{q}\}}$  represents geometric changes due to displacements.  $\frac{\partial [\mathbf{R}]}{\partial \{\mathbf{q}\}}$  represents rotation of the top surface due to displacements and  $\frac{\partial J}{\partial \{\mathbf{q}\}}$  represents stretching of the top surface due to displacements. These terms are often neglected, since they are computationally heavy (Goyal, 2002) and the NRM does not need the correct tangent stiffness in order to converge (Lindgaard, 2011b). If the geometric changes are neglected, the part which is left is:

$$\frac{\partial \{\mathbf{r}^{int,ce_k,top}\}}{\partial \{\mathbf{q}\}} = \int_{-1}^1 \int_{-1}^1 [\mathbf{N}]^T [\mathbf{R}] \frac{\partial \{\mathbf{T}\}}{\partial \{\mathbf{q}\}} J d\xi d\eta \quad (3.7.29)$$

This expression represents a 12-by-24 tangent stiffness matrix. The other half of the tangent stiffness matrix is obtained by differentiating the internal force vector acting on the bottom surface (3.7.25), meaning that the tangent stiffness matrix of the cohesive element is a 24-by-24 matrix. From (3.7.29) it is seen, that for now it is not possible to get any further with the formulation of the tangent stiffness matrix. This is because the term  $\frac{\partial \{\mathbf{T}\}}{\partial \{\mathbf{q}\}}$  represents the constitutive relationship of the cohesive zone, which has not been determined yet. The next section therefore serves to define the constitutive relationship of the cohesive zone as well as the final expression for the tangent stiffness matrix.

### 3.8 Constitutive Relation

As stated above, in order to complete the expression for the tangent stiffness, the constitutive relation for the cohesive zone must be determined. The constitutive law has the purpose of relating opening displacements with tractions in the cohesive zone. In order to have a complete constitutive model for the cohesive zone, some different parts are needed. First of all a traction-displacement relation is needed. This is the part of the constitutive model that, for any given state of a particular point in the cohesive zone, relates tractions to opening displacements. The traction-displacement relation will be treated in subsection 3.8.1. Since the cohesive zone model must be able to describe damage evolution, the next part of the constitutive description deals with this. The damage evolution model defines if and when damage evolution will occur, and when damage is complete. The damage evolution model is presented in subsection 3.8.2. Since the damage evolution model is a one-dimensional model based on equivalent properties, a model for finding these equivalent properties is needed. Hence the last part of the constitutive description concerns interaction criteria used to provide equivalent properties for the damage evolution model depending on the mode mixity of the problem and the material properties. This part is presented in subsection 3.8.3. Finally, when all the individual parts of the constitutive description has been provided, the final expression for the tangent stiffness matrix can be found. This is done in section 3.9.

#### 3.8.1 Traction-Displacement Relation

The continuum damage model used by Turon (2006) is taken, where the energy potential per unit surface is given as function of the scalar damage parameter  $d$ :

$$\psi [\Delta, d] = (1 - d)\psi^0 \quad (3.8.1)$$

where  $\psi^0$  is a convex function of the opening displacements  $\Delta_i$ :

$$\psi^0 [\Delta] = \frac{1}{2}\Delta_i D_{ij}^0 \Delta_j \quad (3.8.2)$$

Note that the opening displacements were defined in (3.5.9), and recall that  $\Delta_3$  is the normal displacement (opening), whereas the shear displacements are  $\Delta_1$  and  $\Delta_2$ . The mentioned damage parameter,  $d$ , ranges from a value of

$d = 0$  (no damage) to  $d = 1$  (full damage). The undamaged stiffness tensor,  $D_{ij}^0$ , is defined as

$$D_{ij}^0 = \delta_{ij}E \quad (3.8.3)$$

with  $E$  as a penalty stiffness. It should be noted that (3.8.2) is simply the expression for the stored elastic energy in a material following Hookes law for linearly elastic materials. In order to ensure that damage has no effect when interfacial penetration occurs, a term which only depends on  $\Delta_3$  is introduced in order to cancel the damage term when  $\Delta_3 < 0$ :

$$\psi[\Delta, d] = (1 - d)\psi^0 + d\psi^0 [\delta_{3i} \langle -\Delta_3 \rangle] \quad (3.8.4)$$

Note that brackets  $\langle \dots \rangle$  denotes the McCauley operator, which is defined as  $\langle x \rangle = \frac{1}{2}(x + |x|)$ . The traction-displacement relation is now found through differentiating the energy potential w.r.t. opening displacements, according to the first Castigliano theorem (Shames and Dym, 1985, p. 140):

$$T_i = \frac{\partial \psi}{\partial \Delta_i} = (1 - d)D_{ij}^0 \Delta_j - dD_{ij}^0 \delta_{3j} \langle -\Delta_3 \rangle \quad (3.8.5)$$

### 3.8.2 Damage Evolution

As mentioned in the introduction, the damage evolution model will be based on equivalent properties and parameters, such that the mode interaction can be handled separately in some interaction criterion. Therefore an opening displacement norm is defined as (Turon, 2006):

$$\lambda = \sqrt{\langle \Delta_3 \rangle^2 + \Delta_s^2} \quad (3.8.6)$$

where  $\Delta_s$  is defined as the norm of both mode II and mode III shear opening displacements as

$$\Delta_s = \sqrt{\Delta_1^2 + \Delta_2^2} \quad (3.8.7)$$

With the opening displacement norm, a single parameter describing the opening displacement is found, and the damage evolution law can be set up in one dimension. The bilinear material law is chosen since it, according to Turon (2006, p. 37), gives a good compromise between accuracy and computational cost. The one dimensional bilinear material law is shown schematically in Figure 3.11. From the figure it is seen, that an initial elastic region exists, and

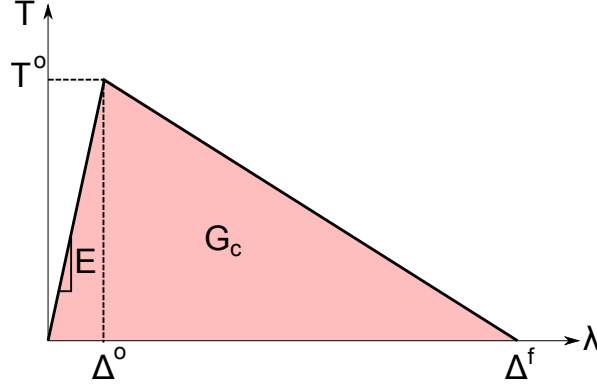


Figure 3.11: The bilinear model with onset traction/opening  $(T^0, \Delta^0)$ , and the opening at which full damage is reached,  $\Delta^f$ .

that damage should only develop beyond the onset  $(\Delta^0, T^0)$ . According to the figure it is seen that, beyond the onset displacement, the displacement-traction relation should be of the linear form:

$$T[\lambda] = \frac{T^0 (\Delta^f - \lambda)}{\Delta^f - \Delta^0} \quad \text{for } \Delta^0 \leq \lambda \leq \Delta^f \quad (3.8.8)$$

Using that the onset traction can be defined from the penalty stiffness,  $E$ , and the onset displacement,  $\Delta^0$  as:

$$T^0 = E\Delta^0 \quad (3.8.9)$$

Equation (3.8.8) can further be written as:

$$T[\lambda] = \frac{E\Delta^0 (\Delta^f - \lambda)}{\Delta^f - \Delta^0} \quad \text{for } \Delta^0 \leq \lambda \leq \Delta^f \quad (3.8.10)$$

Noting that the traction-displacement relation found in subsection 3.8.1 should always hold, (3.8.5) and (3.8.10) are equated and solved for the damage,  $d$ , to obtain:

$$d[\lambda] = \frac{\Delta^f (\lambda - \Delta^0)}{\lambda (\Delta^f - \Delta^0)} \quad \text{for } \Delta^0 \leq \lambda \leq \Delta^f \quad (3.8.11)$$

Note that when using (3.8.5), the extra term that is introduced in order to disregard compressive  $\Delta_3$  is not included above, since negative  $\Delta_3$  is already disregarded in (3.8.6). In actual use of the damage evolution model, the onset displacement will change with damage evolution, such that damage can never

decrease. Hence the model will be used in the following form:

$${}^{(t)}d = \begin{cases} {}^{(t-1)}d & \text{for } 0 \leq \lambda < {}^{(t)}\tilde{\Delta}^0 \\ \frac{\Delta^f(\lambda - \Delta^0)}{\lambda(\Delta^f - \Delta^0)} & \text{for } {}^{(t)}\tilde{\Delta}^0 \leq \lambda \leq \Delta^f \\ 1 & \text{for } \Delta^f < \lambda \end{cases} \quad (3.8.12)$$

where the preceding superscripts denote time step. Note that time  $t-1$  refers to a converged iteration, but that time  $t$  not necessarily does so. Since the onset displacement  $\tilde{\Delta}^0$  is a function of the damage it is denoted with tilde to distinguish it from the material property onset displacement  $\Delta^0$ . The current onset displacement,  ${}^{(t)}\tilde{\Delta}^0$ , is calculated from the previous damage as:

$${}^{(t)}\tilde{\Delta}^0 = \frac{\Delta^0 \Delta^f}{\Delta^f - {}^{(t-1)}d(\Delta^f - \Delta^0)} \quad (3.8.13)$$

which is found by isolating  $\lambda$  in (3.8.11).

### 3.8.3 Mode Interaction

In order to use the damage evolution model presented above, the used equivalent properties  $\Delta^0$ ,  $\Delta^f$  and  $T^0$  must be determined for a given mode mixity. The reason why the properties are called equivalent properties is, that the properties are typically known for the pure crack modes, modes I, II and III, but not for general mixed mode cracks. The relation between the properties for the pure modes and the equivalent properties for a given mode mixity is sketched in Figure 3.12. In Chapter 2 the mode mixity parameter was defined from stress intensity factors. However since the FEM is displacement based, a mode mixity parameter defined in displacements is used instead. This is defined as:

$$\beta = \frac{\Delta_s}{\langle \Delta_3 \rangle + \Delta_s} \quad (3.8.14)$$

Below the mentioned three equivalent properties are found.

**Finding  $\Delta_f$ :** Propagation of a crack occurs when the energy release rate,  $G$ , surpasses the critical energy release rate  $G_c$  such that

$$G = G_I + G_{II} + G_{III} \geq G_c \quad (3.8.15)$$

For a mixed mode crack a variety of interaction criteria exist to estimate  $G_c$ . Camanho et al. (2003) found the Benzeggagh-Kenane (BK) criterion to

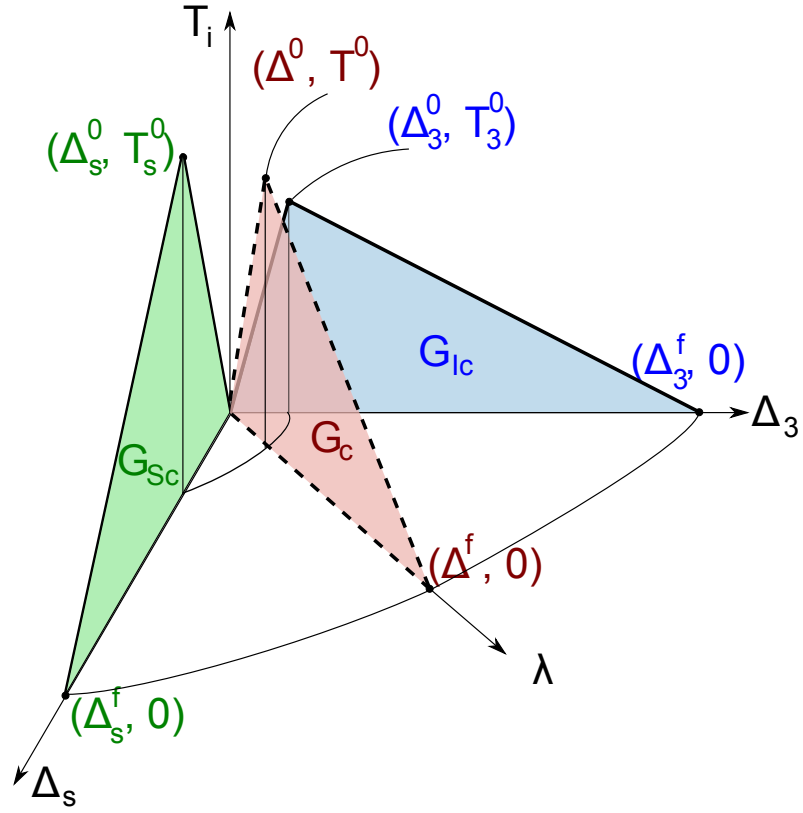


Figure 3.12: Illustration of traction opening displacement surface along with critical energy release rate for a given mode mixity.

perform well. The BK criterion is given as (Camanho et al., 2003):

$$G_c = G_{Ic} + (G_{IIc} - G_{Ic}) \left( \frac{G_s}{G_I + G_s} \right)^\eta \quad (3.8.16)$$

where  $G_s = G_{II} + G_{III}$  and  $\eta$  is a constant found by curvefitting material data. The critical energy release rates can be written in terms of displacements as:

$$G_{Ic} = \frac{1}{2} E \Delta_3^0 \Delta_3^f \quad (3.8.17)$$

$$G_{IIc} = \frac{1}{2} E \Delta_1^0 \Delta_1^f \quad (3.8.18)$$

The effective critical energy release rate  $G_c$  at some mode mixity,  $\beta$ , is:

$$G_c = \frac{1}{2} E \Delta^0 \Delta^f \quad (3.8.19)$$

Inserting (3.8.17) to (3.8.19) in (3.8.16) and solving for  $\Delta^f$  the following is obtained:

$$\Delta^f = \frac{\Delta_3^0 \Delta_3^f + \left( \Delta_1^f \Delta_1^0 - \Delta_3^0 \Delta_3^f \right) \left( \frac{G_s}{G_I + G_s} \right)^\eta}{\Delta^0} \quad (3.8.20)$$

Now it only remains to find an expression for the last term in the numerator above. For any given situation, the values of  $\beta$  and  $\lambda$  are known from the expressions in (3.8.6) and (3.8.14). By solving these two equations for  $\Delta_3$  and  $\Delta_s$ , the following is obtained:

$$\Delta_s = \frac{\beta \lambda}{\sqrt{2\beta^2 - 2\beta + 1}} \quad \text{and} \quad \Delta_3 = \frac{\lambda(\beta - 1)}{\sqrt{2\beta^2 - 2\beta + 1}} \quad (3.8.21)$$

From the above the displacement components of the equivalent onset/final displacements can be expressed. This is done by inserting  $\lambda = \Delta^0$  and  $\lambda = \Delta^f$  respectively:

$$\Delta_{sm}^0 = \frac{\beta \Delta^0}{\sqrt{2\beta^2 - 2\beta + 1}} \quad \text{and} \quad \Delta_{3m}^0 = \frac{\Delta^0(\beta - 1)}{\sqrt{2\beta^2 - 2\beta + 1}} \quad (3.8.22)$$

$$\Delta_{sm}^f = \frac{\beta \Delta^f}{\sqrt{2\beta^2 - 2\beta + 1}} \quad \text{and} \quad \Delta_{3m}^f = \frac{\Delta^f(\beta - 1)}{\sqrt{2\beta^2 - 2\beta + 1}} \quad (3.8.23)$$

Note that indices  $m$  serve to emphasise, that these properties are the components for a given mode mixity. From these expressions, the energy release rate components at full damage can be expressed as:

$$G_{Im} = \frac{1}{2} E \Delta_{3m}^0 \Delta_{3m}^f \quad (3.8.24)$$

$$G_{sm} = \frac{1}{2} E \Delta_{sm}^0 \Delta_{sm}^f \quad (3.8.25)$$

Inserting the found expressions for  $\Delta_{3m}^0$ ,  $\Delta_{3m}^f$ ,  $\Delta_{sm}^0$ , and  $\Delta_{sm}^f$  into equations (3.8.24) and (3.8.25) the following is obtained:

$$G_{Im} = \frac{E \Delta^0 \Delta^f (\beta - 1)^2}{4\beta^2 - 4\beta + 2} \quad \text{and} \quad G_{sm} = \frac{E \Delta^0 \Delta^f \beta^2}{4\beta^2 - 4\beta + 2} \quad (3.8.26)$$

Finally inserting these energy release rate components into (3.8.20) the following is obtained:

$$\Delta^f = \frac{\Delta_3^0 \Delta_3^f + \left( \Delta_1^f \Delta_1^0 - \Delta_3^0 \Delta_3^f \right) B^\eta}{\Delta^0} \quad (3.8.27)$$

with  $B$  only being dependent on  $\beta$ :

$$B = \frac{G_{sm}}{G_{Im} + G_{sm}} = \frac{\beta^2}{1 + 2\beta^2 - 2\beta} \quad (3.8.28)$$

**Finding  $\Delta^0$**  Initiation in a pure mode loading occurs, when the traction reaches the onset traction, e.g. for mode I when  $T_3 = T_3^0$ . When interaction is taken into account, the criterion proposed by Turon (2006) is used, which suggests that initiation occurs when:

$$T_1^2 + T_2^2 + T_3^2 = T^0{}^2 \quad (3.8.29)$$

Furthermore it is proposed to find the onset traction using a criterion similar to the one used for finding the propagation displacement. Doing this one ends up with:

$$T^0 = \sqrt{T_I^0{}^2 + (T_{II}^0{}^2 - T_I^0{}^2) B^\eta} \quad (3.8.30)$$

Inserting (3.8.30) into (3.8.29), expressing the result in displacements ( $T_i = E\Delta_i$ ) and solving for the onset displacement we get:

$$\Delta^0 = \sqrt{\Delta_I^0{}^2 + (\Delta_{II}^0{}^2 - \Delta_I^0{}^2) B^\eta} \quad (3.8.31)$$

### 3.8.4 Constitutive Tangent Tensor

The expression in (3.8.5) relates tractions and displacements for a constant damage  $d$ . The constitutive tangent tensor is then given as  $(1-d)D_{ij}^0$  (denoted  $D_{ij}^{\tan 1}$ ), as long as  $\lambda \leq {}^{(t)}\tilde{\Delta}^0$  for positive  $\Delta_3$ . We now proceed to find the constitutive tangent tensor when  $\lambda > {}^{(t)}\tilde{\Delta}^0$  (denoted  $D_{ij}^{\tan 2}$ ). The different constitutive tangent tensors are shown on Figure 3.13 for the case of pure mode  $j$  displacement.

Consider (3.8.5) to be changing with some pseudo-time, because both the damage parameter,  $d$ , and the opening displacements,  $\Delta_j$ , can evolve. If we define the stiffness tensor as:

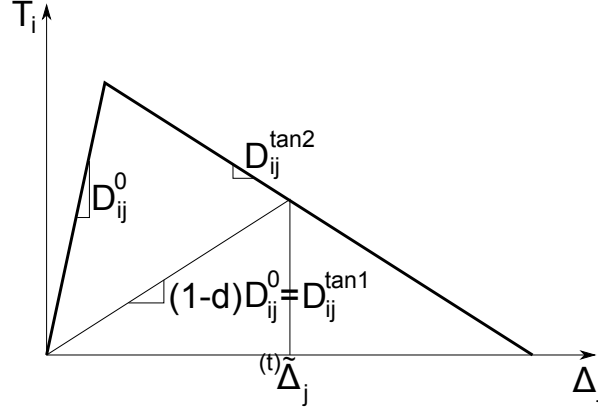
$$D_{ij} = \delta_{ij}E \left( 1 - d \left( 1 + \delta_{3j} \frac{\langle -\Delta_j \rangle}{\Delta_j} \right) \right) \quad (3.8.32)$$

then (3.8.5) can be written compactly as:

$$T_i = D_{ij}\Delta_j \quad (3.8.33)$$

The rate dependance can now be found by taking the total derivative of (3.8.33):

$$\dot{T}_i = D_{ij}\dot{\Delta}_j + \dot{D}_{ij}\Delta_j \quad (3.8.34)$$

Figure 3.13: Constitutive tangents for a pure  $j$  displacement.

Now the derivative of the stiffness tensor is:

$$\dot{D}_{ij} = -\delta_{ij}E \left( 1 + \delta_{3j} \frac{\langle -\Delta_j \rangle}{\Delta_j} \right) \dot{d} \quad (3.8.35)$$

Inserting this in (3.8.34) we obtain:

$$\dot{T}_i = D_{ij} \dot{\Delta}_j - \delta_{ij}E \left( 1 + \delta_{3j} \frac{\langle -\Delta_j \rangle}{\Delta_j} \right) \Delta_j \dot{d} \quad (3.8.36)$$

In order to finally obtain the material tangent stiffness, we need an expression for the rate of change of the damage,  $\dot{d}$ . Taking the total derivative of (3.8.12) we can write:

$$\dot{d} = \frac{\partial d}{\partial \Delta^0} \dot{\Delta}^0 + \frac{\partial d}{\partial \Delta^f} \dot{\Delta}^f + \frac{\partial d}{\partial \lambda} \dot{\lambda} \quad (3.8.37)$$

In the above it is seen that the rate of change of the damage parameter is dependent on both the equivalent onset and final displacements, which again are functions of the mode mixity according to subsection 3.8.3. Turon (2006) though argues that the mode mixity often changes relatively slowly and therefore the first two terms of (3.8.37) are neglected. Differentiating (3.8.6) we obtain:

$$\dot{\lambda} = \frac{\partial \lambda}{\partial \Delta_k} \dot{\Delta}_k = \frac{\Delta_k}{\lambda} \left( 1 + \delta_{3k} \frac{\langle -\Delta_k \rangle}{\Delta_k} \right) \dot{\Delta}_k \quad (3.8.38)$$

Furthermore, expanding (3.8.37) using (3.8.12) we obtain:

$$\dot{d} = \begin{cases} 0 & \text{for } 0 \leq \lambda < {}^{(t)}\tilde{\Delta}^0 \\ \frac{\Delta^0 \Delta^f}{\lambda^2 (\Delta^f - \Delta^0)} \dot{\lambda} & \text{for } {}^{(t)}\tilde{\Delta}^0 \leq \lambda \leq \Delta^f \\ 0 & \text{for } \Delta^f < \lambda \end{cases} \quad (3.8.39)$$

Finally by collecting (3.8.36), (3.8.38) and (3.8.39), we get the rate equation for the traction:

$$\dot{T}_i = D_{ij}^{tan} \dot{\Delta}_j \quad (3.8.40)$$

with the material tangent stiffness

$$D_{ij}^{tan} = \begin{cases} D_{ij} & \text{for } 0 \leq \lambda < \tilde{\Delta}^0 \\ D_{ij} - E \left( 1 + \delta_{3i} \frac{\langle -\Delta_i \rangle}{\Delta_i} \right) \left( 1 + \delta_{3j} \frac{\langle -\Delta_j \rangle}{\Delta_j} \right) H \Delta_i \Delta_j & \text{for } \tilde{\Delta}^0 \leq \lambda \leq \Delta^f \\ 0 & \text{for } \Delta^f < \lambda \end{cases} \quad (3.8.41)$$

and  $H$  defined as:

$$H = \frac{\Delta^f \Delta^0}{(\Delta^f - \Delta^0) \lambda^3} \quad (3.8.42)$$

Now that both the tangent stiffness in (3.8.41), and the displacement-traction relation in (3.8.5) have been found, the element formulation can be finalised.

### 3.9 Finalising the Element Formulation

In section 3.7 an expression for the element tangent stiffness of a cohesive element was presented. The found expression is repeated here for convenience:

$$\frac{\partial \{\mathbf{r}^{int,ce_k,top}\}}{\partial \{\mathbf{q}\}} = \int_{-1}^1 \int_{-1}^1 [\mathbf{N}]^T [\mathbf{R}] \frac{\partial \{\mathbf{T}\}}{\partial \{\mathbf{q}\}} J d\xi d\eta \quad (3.9.1)$$

As it was mentioned, in order to finalise the above expression for implementation, the constitutive relation was needed to determine the term,  $\frac{\partial \{\mathbf{T}\}}{\partial \{\mathbf{q}\}}$ . Since the constitutive tangent stiffness found in subsection 3.8.4 is a function of the opening displacements,  $\Delta_i$ , we can write out the derivative of the term in question as:

$$\frac{\partial \{\mathbf{T}\}}{\partial \{\mathbf{q}\}} = \frac{\partial \{\mathbf{T}\}}{\partial \{\Delta\}} \frac{\partial \{\Delta\}}{\partial \{\mathbf{u}\}} \frac{\partial \{\mathbf{u}\}}{\partial \{\mathbf{q}\}} \quad (3.9.2)$$

In the above, the first term represents the material tangent stiffness given in (3.8.41) and is a three by three matrix. The second term can be written out

from (3.5.9) as:

$$\frac{\partial \{\Delta\}}{\partial \{\mathbf{u}\}} = \frac{\partial [\mathbf{R}]^T}{\partial \{\mathbf{u}\}} (\{\mathbf{u}^+\} - \{\mathbf{u}^-\}) + [\mathbf{R}]^T \frac{\partial (\{\mathbf{u}^+\} - \{\mathbf{u}^-\})}{\partial \{\mathbf{u}\}} \quad (3.9.3)$$

$$\approx [\mathbf{R}]^T \frac{\partial (\{\mathbf{u}^+\} - \{\mathbf{u}^-\})}{\partial \{\mathbf{u}\}} \quad (3.9.4)$$

$$= [\mathbf{R}]^T \left[ [\mathbf{I}] , -[\mathbf{I}] \right] \quad (3.9.5)$$

As seen above the term containing the derivative with respect to displacements of the rotation matrix is discarded, since rotations are assumed to change slowly. Thus we have:

$$\frac{\partial \{\Delta\}}{\partial \{\mathbf{u}\}} = \left[ [\mathbf{R}]^T , -[\mathbf{R}]^T \right] \quad (3.9.6)$$

The last term in (3.9.2) can, considering (3.7.21) and (3.7.22), easily be seen to give the six by twentyfour matrix:

$$\frac{\partial \{\mathbf{u}\}}{\partial \{\mathbf{q}\}} = \begin{bmatrix} [\mathbf{N}] , & [\mathbf{0}] \\ [\mathbf{0}] , & [\mathbf{N}] \end{bmatrix} \quad (3.9.7)$$

Thus collecting equations (3.9.1), (3.9.6) and (3.9.7) we obtain:

$$\frac{\partial \{\mathbf{r}^{int,ce_k,top}\}}{\partial \{\mathbf{q}\}} = \int_{-1}^1 \int_{-1}^1 \left[ [\mathbf{M}] , -[\mathbf{M}] \right] J d\xi d\eta \quad (3.9.8)$$

where

$$[\mathbf{M}] = [\mathbf{N}]^T [\mathbf{R}] [\mathbf{D}^{tan}] [\mathbf{R}]^T [\mathbf{N}] \quad (3.9.9)$$

As mentioned in subsection 3.8.4, the above only gives the top half of the tangent stiffness matrix. The other half is given by  $\frac{\partial \{\mathbf{r}^{int,ce_k,bot}\}}{\partial \{\mathbf{q}\}}$ . Thus the full tangent stiffness matrix becomes:

$$[\mathbf{K}^{tan}] = \int_{-1}^1 \int_{-1}^1 \begin{bmatrix} [\mathbf{M}] , & -[\mathbf{M}] \\ -[\mathbf{M}] , & [\mathbf{M}] \end{bmatrix} J d\xi d\eta \quad (3.9.10)$$

### 3.10 Conclusion

In this chapter the necessary theory for implementing a CZ element has been presented. This was done by starting from the governing equations, rewriting

them to their weak form and discretising the problem. After discretisation of the full problem, only the CZ elements were taken further. A bilinear material law and the BK interaction criterion were chosen. For ease of computation some terms of the derived tangent stiffness were disregarded, since it was argued, that they will not be necessary. Finally the element internal force vector and tangent stiffness matrix were assembled, thereby providing the needed constituents for implementation of the element.

## Chapter 4

# Implementation and Verification

In this chapter a few comments regarding the implementation of the theory presented in Chapter 3, in the user programmed CZ element, are given. This is done in section 4.1. The rest of the chapter concerns verification of the implementation as well as studying the influence of some different parameters of the CZ model on the results. The verification is performed in two steps: First the kinematics and the constitutive model of the element are checked using a model containing only one element. This is done in section 4.2. Second the overall behaviour of the element is checked by using it in models of the different tests (DCB, ENF and MMB), which were presented in Chapter 2. Results obtained with the implemented element can then be compared to results obtained using the ANSYS CZ element as well as the LEFM solutions, and it can be verified, that it provides the expected results and shows reasonable convergence rates. This is done in section 4.3. Throughout the use of CZ elements, both the ANSYS element and the user programmed element, it has been found, that the magnitude of the onset tractions has a tremendous effect on model convergence. Therefore it is often necessary to use low onset tractions to obtain convergence. Hence this chapter is concluded by examining the influence of the onset traction on obtained results, in order to clarify the effect of the compromise, that has to be made in order to obtain convergence. This is done in section 4.4.

## 4.1 Implementation of CZ Element

A flowchart for the solution procedure of the NRM, described in section 3.6, can be seen in Figure 4.1. The red box indicates in which part of the solution procedure the element formulations are needed. It should be noted that the red box contains both the computation of the structural finite elements as well as the CZ elements. ANSYS controls the bookkeeping and ensures that the right element formulation is called for a given element. Based on the theory from Chapter 3 a user programmed element has been implemented in ANSYS. This element will from this point on be referred to as the UPF, due to the ANSYS abbreviation of User Programmable Feature. The ANSYS built in 3D CZ element, which is the INTER205 element (ANSYS, Inc, 2010), will be referred to as ANS. The UPF has been programmed in FORTRAN, but is in this thesis only documented by the use of pseudocode. The pseudocode can be found in Appendix B. The focus in the pseudocode is mainly to document the element logic along with important numerical checks.

By implementing the UPF, it is possible to obtain functionalities that the ANSYS implementation does not have. Among features that have been implemented in the UPF can be mentioned the possibilities of outputting and plotting the average mode mixity, the dissipated and stored energy, as well as the current damage (calculated as the ratio between the energy put into the element and the critical energy release rate in the current mode mixity). These features are documented in Appendix B.

## 4.2 Element Verification

In this section a model, containing only a single element, will be used to verify the implementation of the CZ element. The files needed for generating the data in this section, including the FE model, can be found on the attached CD in the folder 'Model\Element Verification'. A sketch of the model is shown in Figure 4.2. As seen the model is very simple as it consists of only one CZ element. The CZ element to be used can be chosen as either ANS or UPF for comparison. The model works in conjunction with a MATLAB script, that can generate nodal displacements for the element according to prescribed rigid body rotations and rigid body translations, as indicated on the right side of the figure. Opening displacements are always applied relative to the element

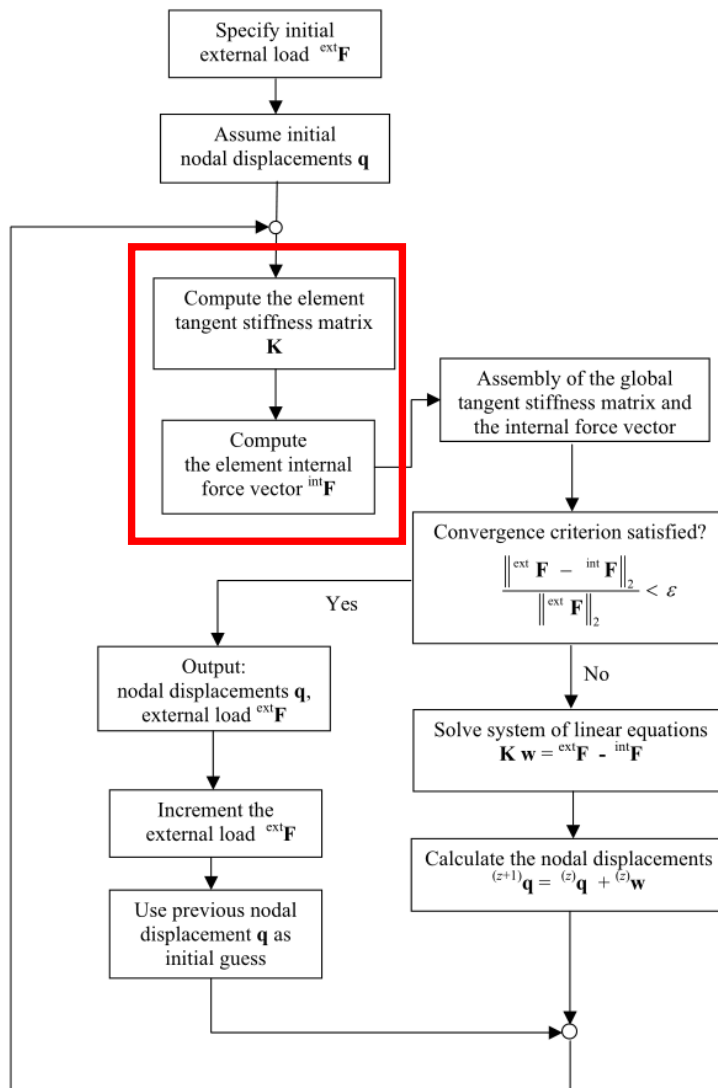


Figure 4.1: Flowchart of the NRM. The figure stems from Goyal (2002, p.96) but has been altered.

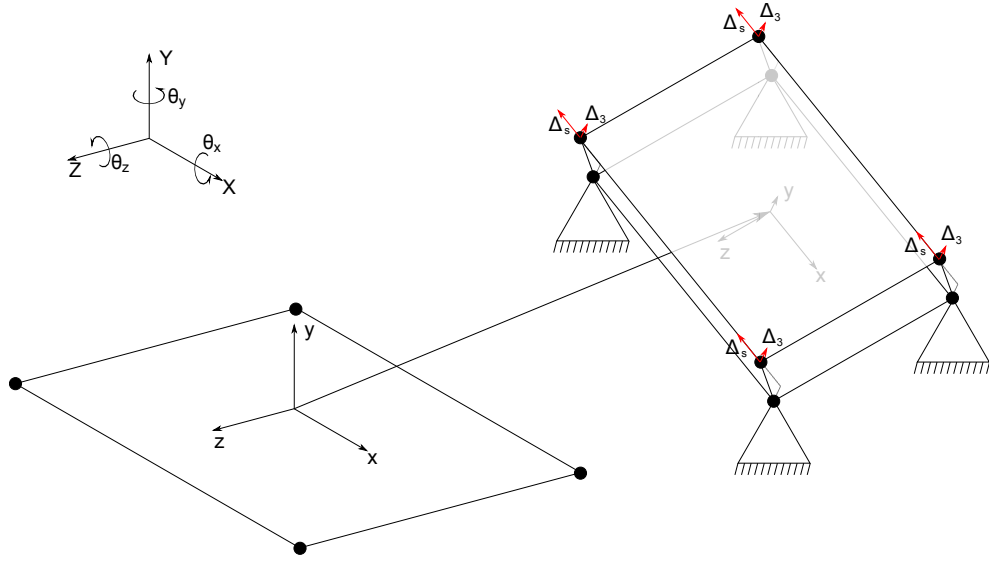


Figure 4.2: Sketch of the one element model along with the element and global coordinate systems.

orientation, so that the element should always provide the same results. In this way it can be verified, whether the formulation of the element kinematics has been implemented correctly. In order to also verify the implementation of the material model, complete sweeps of the  $(\Delta_3, \Delta_s)$  opening displacement space (normal, shear opening) are made. This is done by running a series of analyses specified as:

$$\theta = [-\pi; \pi] \quad (4.2.1)$$

$$\Delta_3 = \Delta_{3max}^t \cos \theta \quad \text{for} \quad |\theta| < \frac{\pi}{2} \quad (4.2.2)$$

$$\Delta_3 = \Delta_{3max}^c \cos \theta \quad \text{for} \quad |\theta| > \frac{\pi}{2} \quad (4.2.3)$$

$$\Delta_s = \Delta_{1max} \sin \theta \quad (4.2.4)$$

where  $\Delta_{3max}^t$  and  $\Delta_{3max}^c$  are the maximum applied normal opening displacements in tension (opening) and compression (closing) respectively, and  $\Delta_{1max}$  is the maximum applied shear opening displacement. The maximum opening displacements are chosen, such that complete element damage is obtained no matter the angle  $\theta$ . An exception to this is for negative  $\Delta_3$  where  $\Delta_{3max}^c$  is chosen so small, that traction norms end up in the same magnitude

as the material onset traction. The used material data is shown in Table 4.1. For each choice of direction an analysis is performed, and data is recorded for each substep in the solution. Using this procedure the following plots have been produced. In Figures 4.3a and 4.3b, the traction norm given as

Material Data				
$G_{Ic}$	$G_{IIc}$	$T_3^0$	$T_s^0$	$E$
969 J/m <sup>2</sup>	1717 J/m <sup>2</sup>	4 MPa	5 MPa	10 <sup>6</sup> N/mm <sup>3</sup>

Table 4.1: Material data used for the one element model.

$$T = \sqrt{T_3^2 + T_s^2} \quad (4.2.5)$$

is plotted on a surface plot for different mode mixities with positive  $\Delta_3$  for the UPF and the ANS respectively. In Figures 4.3c and 4.3d the domain with negative  $\Delta_3$  of the plots is shown. Note that the plots should only be compared qualitatively, since the UPF uses the B-K criterion, whereas the ANS uses some other interaction criterion (which by testing is believed to be a power law criterion). It is not apparent from the ANSYS documentation which criterion is used. The plots are seen to be very similar. For easier comparison contour plots of the same data have been produced. These plots are shown in Figures 4.3e and 4.3f. In the contour plots it is easier to see the difference between the different interaction criteria of the two elements, and it is noted, that the differences are indeed minor. In Figure 4.4a, the difference in traction norms between the theoretical material model and the results provided from the UPF is plotted. It is readily seen, that the differences are very minor (less than 1 Pa), and can be attributed to numerical rounding.

The above described figures were produced for an unrotated/translated element. The tests have been repeated for several combinations of rigid body rotations and rigid body translations. This has not given any changes except for expected numerical differences. The plots presented so far will not be repeated for the rotated and translated test, but in Figure 4.4b the difference between the theoretical material model and the element implementation for

the case, where the element has been translated and rotated as:

$$\theta_y = 13^\circ \quad (4.2.6)$$

$$\theta_x = 55^\circ \quad (4.2.7)$$

$$\theta_z = 27^\circ \quad (4.2.8)$$

$$\mathbf{x} = [3.2 \ 4.4 \ 1.4]^T \quad (4.2.9)$$

is shown. Note that the rotations are performed in the shown succession (Y-X-Z Fixed angles). From the figure it is seen, that the differences are still very minor. It is though noticed, that the errors are four orders of magnitude higher than for the unrotated case seen on Figure 4.4a. The reason for this has not been found, but is believed to stem from rounding in the MATLAB to ANSYS interface, or when performing calculations in the APDL script of the one element model.

Several conclusions can be made from the present study. First it is seen from Figures 4.4a and 4.4b, that the differences between predicted traction norm and the results provided by the UPF are orders of magnitude larger in the regions close to zero normal opening regardless of the magnitude of the shear opening displacement. This is because in this region the full penalty stiffness, which is chosen very large, is used in the element and hence even small differences in opening displacements can cause high differences in traction norm. This has also been verified by separately changing the penalty stiffness and observing the effect on the error. This shows, why the penalty stiffness cannot be chosen arbitrarily large. Second it was found through the examination, that use of the mm – MPa unit system should be recommended as opposed to the m – Pa unit system, since the latter led to unexpectedly large mismatches due to bad conditioning of the problem (compare with figures 4.4c and 4.4d). Through this study it has been verified, that the implementation of the kinematics and the constitutive model of the UPF has been made correctly. In the following section the calculation of the element tangent stiffness matrix will be tested by using the element in more physical problems.

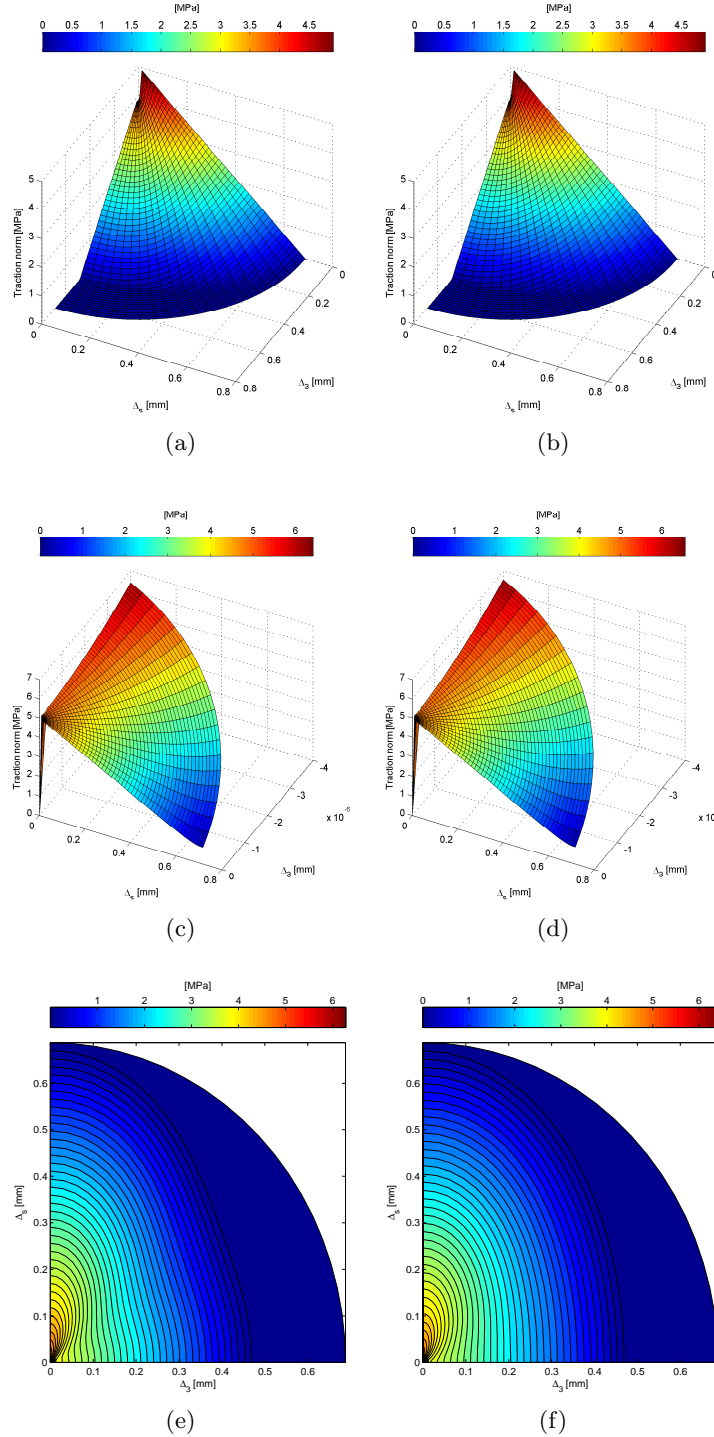


Figure 4.3: Plots of the traction norm for different mode mixities. **Top row:** Surface plot of the part of the domain with positive normal opening displacements for a) the UPF, and b) for the ANS. **Middle row:** Surface plot of the part of the domain with negative normal opening displacements for c) the UPF, and d) for the ANS. **Bottom row:** Contour plots for e) the UPF, and f) for the ANS.

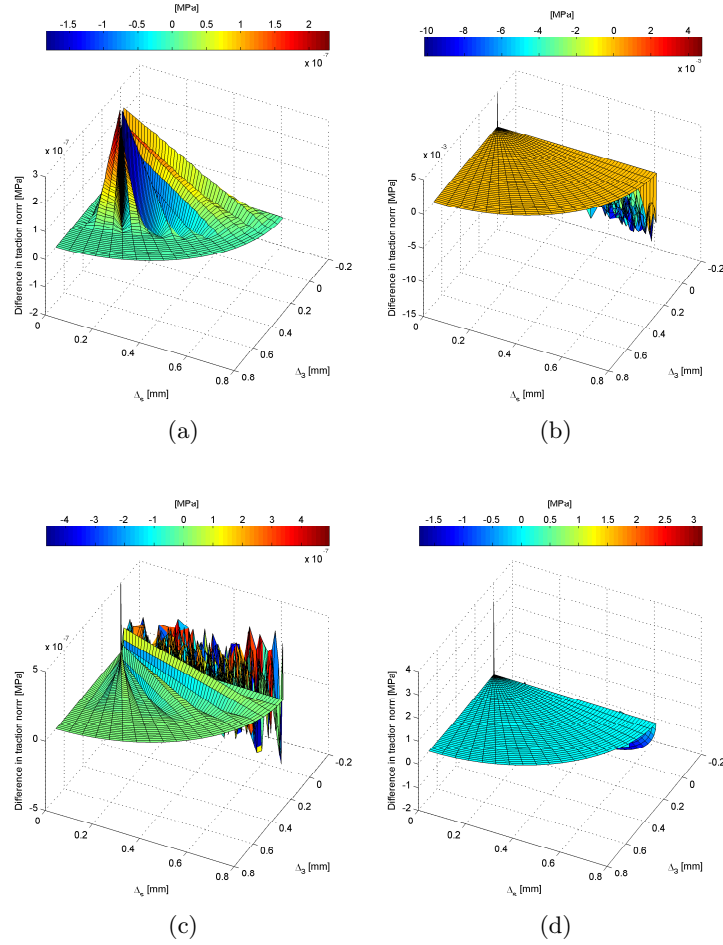


Figure 4.4: The difference in traction norm between the UPF and the theoretical constitutive law. **Top row:** Calculated in the mm-MPa unit system for a) the standard case and b) the rotated and translated case. **Bottom row:** Calculated in the m-Pa unit system for c) the standard case and d) the rotated and translated case.

### 4.3 Application on Specimen Models

The purpose of this section is to further verify the implementation through FE simulations of the tests (DCB, ENF, MMB) presented in section 2.2. These three tests ensure, that both mode I and shear mode and a combination hereof can be represented by the element, and also serve to verify, that the tangent stiffness matrix is correctly implemented. The three models are shown again on Figure 4.5. The verification is done by comparing FE results obtained using the UPF with results from Camanho et al. (2003), and with LEFM beam solutions as well as results obtained using the ANS.

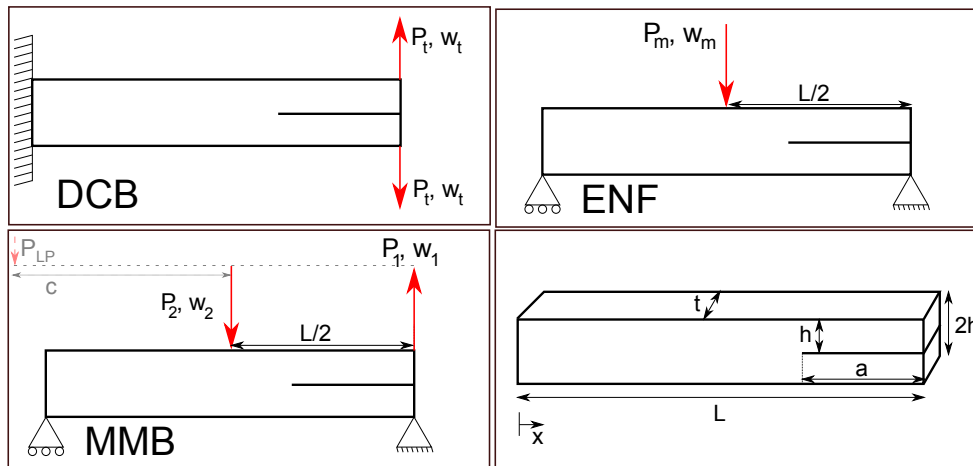


Figure 4.5: The DCB-, ENF-, and MMB specimen models and dimensions. Loads and displacements are now denoted with subscripts, so that they can be distinguished.

#### 4.3.1 The FE model

The FE model is written in APDL (ANSYS Parametric Design Language) and is working in combination with MATLAB where all relevant parameters can be set. All needed files to reproduce the results can be found on the attached CD in the folder 'Models\Specimen Tests'.

#### Material and Dimensions

The specimen models are given the same material properties and geometry as used in Camanho et al. (2003). The used data, which all models have in common, is listed in Table 4.2. Dimensions are shown on Figure 4.5. The

models have different initial crack lengths. Furthermore a change in the MMB ratio  $\theta$  yields a different lever arm length  $c$ . Initial crack lengths and lever arm lengths are shown in Table 4.3.

Material Data and Dimensions				
$E_{11}$ 122.7 GPa	$E_{22} = E_{33}$ 10.1 GPa	$G_{12} = G_{13}$ 5.5 GPa	$G_{23}$ 3.7 GPa	$\nu_{12} = \nu_{13}$ 0.25
$\nu_{23}$ 0.45	$G_{Ic}$ 969 J/m <sup>2</sup>	$G_{IIc}$ 1717 J/m <sup>2</sup>	$T_3^0$ 80 MPa	$T_s^0$ 100 MPa
$L$ 102 mm	$h$ 1.56 mm	$t$ 25.4 mm	E 10 <sup>6</sup> N/mm <sup>3</sup>	

Table 4.2: Material data and dimensions are taken from Camanho et al. (2003) and are for 24-ply unidirectional AS4/PEEK (APC2) carbon fibre reinforced composite specimens.

Model Specific Dimensions					
	DCB	MMB $\theta = 4$	MMB $\theta = 1$	MMB $\theta = 1/4$	ENF
$a$	32.9 mm	33.7 mm	34.1 mm	31.4 mm	39.3 mm
$c$	-	109.89 mm	44.59 mm	28.47 mm	-

Table 4.3: Model specific parameters from Camanho et al. (2003).

### Element Types and Mesh

In the bulk material (i.e. outside the interface), 3D 8-node structural solid elements, named SOLID185 in ANSYS, are used with enhanced strain formulation enabled. The enhanced strain formulation is enabled to avoid shear locking, which is important, since bending will be present in all specimens. In the cohesive zone either the 3D 8-node cohesive element named INTER205, or the UPF is used. In both cases a bilinear material law is used.

In the ENF model contact elements are used in order to prevent the bar above the crack from going through the lower bar. Contact elements are only used in the initial crack, i.e.  $L - a_0 \leq x \leq L$ . An alternative to contact elements would be fully damaged cohesive elements. However the ANS does not have this feature.

The used mesh is listed in Table 4.4 in relation to dimensions as shown on

Figure 4.5. A large number of  $n_{\text{elem},L}$  is required for the model to be able to converge, when unstable crack propagation begins. The onset of unstable crack propagation is of course the point on the load-displacement curve, where the slope turns negative. This point will from here on be denoted the limit point. It was found that 1600 elements gave good results w.r.t. convergence beyond the limit point, and that further increasing the number of elements did not help. With regards to  $n_{\text{elem},h}$ , two elements worked well. Furthermore increasing or decreasing  $n_{\text{elem},h}$  did not influence load/displacement results due to the large amount of  $n_{\text{elem},L}$  and the enabled enhanced strain formulation.

Mesh			
	L	h	t
Element Size (elem)	0.064 mm	0.78 mm	25.4 mm
No. of Elements ( $n_{\text{elem}}$ )	1600	2	1

Table 4.4: Mesh used in all specimen models. Dimensions are shown on Figure 4.5.

### Loading and Solving

The boundary conditions can either be given in terms of forces or displacements. If displacements are applied, the reaction force is measured to create a load-displacement curve. The type of boundary condition has an influence on the choice of solver, since the part of the load-displacement curve with a negative slope cannot be traced with the Newton-Raphson solver for a force boundary condition, as explained in section 3.6. Since the theory of the MMB test is based on applied forces, a force boundary condition will be used in all cases. Therefore, in order to solve the models, an equilibrium path tracing algorithm is used. ANSYS offers an arc-length method, which will hence be used. The reference arc-length radius is determined from the ratio of load and substeps, see (ANSYS, Inc, 2010). It is estimated, that load steps of around 3 N will allow to capture the load-displacement curve with satisfactory precision. Using a load of 1000 N this results in approximately 333 substeps. The arc-length radius is allowed to change within some limits, and the upper limit factor is simply chosen as 1 in order to get consistent load steps, while the lower limit is chosen to 0.01, i.e. load steps of down to  $\approx 0.03$  N are allowed. Nonlinear geometry setting is not enabled, since this caused convergence issues when used in combination with CZ elements. The option

'SOLCONTROL' is set to on, since a more stable arc-length algorithm is then used (ANSYS, Inc, 2010).

### 4.3.2 DCB Test

The FE results for the DCB test are seen on Figure 4.6a and are also tabulated in Table 4.5 together with the maximum load found by Camanho et al. (2003) and LEFM beam solution. It can be seen, that it was not possible to achieve the same maximum load as Camanho et al. (2003), which is also higher than the LEFM predicted max load. However the element type and  $n_{\text{elem},h}$ , used by Camanho et al. (2003), are not known. This is critical due to shear locking and could explain the different results, if e.g.  $n_{\text{elem},h} = 1$  have been used. With regards to the LEFM comparison it is seen, that LEFM gives a stiffer response, and that FE results go towards a point on the LEFM propagation curve. The reason for this is investigated in section 4.3.5.

The FE results using respectively ANS and UPF are seen to match well. The analyses are set to terminate at a tip displacement of 4 mm, and hence the cumulative amount of equilibrium iterations can be compared. In Table 4.4 it can be seen, that the solver needs less equilibrium iterations when using the UPF element for approximately the same amount of substeps.

The length of the cohesive zone,  $L_{cz}$ , is also interesting, since it, according to Turon et al. (2007), is a critical measure w.r.t. mesh size.  $L_{cz}$  is defined as the distance from the physical crack tip to the point where the cohesive traction is at its maximum (Turon et al., 2007). In order to estimate the length of the cohesive zone, the interface tractions are plotted along the length-direction of the DCB specimen on Figure 4.6b for the last converged substep. This reveals, that the cohesive zone is approximately 0.9 mm, which corresponds to 14 elements. Turon et al. (2007) found, that at least two elements should be present in the cohesive zone for decent results, and this is hence well above.

### 4.3.3 ENF Test

The results for the ENF test are seen on Figure 4.7a and are also given in Table 4.6. It is seen, that approximately the same max load as Camanho is reached. Compared to LEFM, the FE results match very well initially, but deviate slightly as the limit point is approached. On the propagation curve

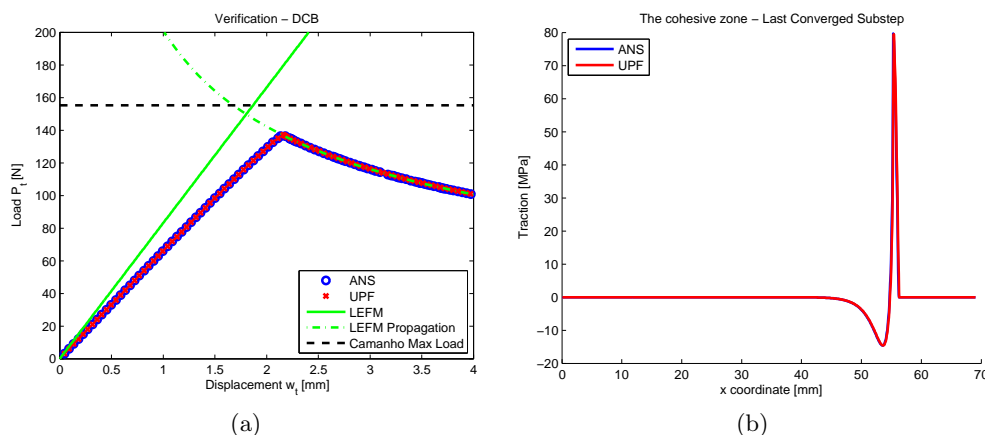


Figure 4.6: DCB test. a) Comparison of FEM, LEFM and Camanho. b) Plot of traction along the length in order to determine the length of the cohesive zone.

Post Analysis DCB					
Dataset	Max Load [N]	Error [%]	Iterations	Substeps	$L_{cz}$ [mm]
ANS	137.1	-6.8	624	109	0.9
UPF	136.3	-7.3	367	95	0.9
LEFM	149.6	1.7	-	-	-
Camanho FE	155.3	5.6	-	-	-
Experimental	147.1	-	-	-	-

Table 4.5: Post analysis comparison of DCB results. Error is vs. Experimental. Datasets 'Camanho' and 'Experimental' are from Camanho et al. (2003).

the FE results are also seen to deviate beyond  $w_m \approx 4$  mm, but this is due the LEFM propagation solution not being valid for  $a > L/2$ .

Comparing ANS and UPF, it is seen, that the ANS element converges longer than UPF, which stops converging not long after the limit point. For some reason, when using the UPF element, the arc-length solver starts 'drifting back', i.e. retraces steps along the un-loading curve. This is not shown on the plot, but is the reason, why UPF stops before ANS. Due to this it is also difficult to compare the number of equilibrium iterations used. The number of iterations used to reach the limit point can be compared, but is less interesting, since convergence before the limit point is not a problem. The amount

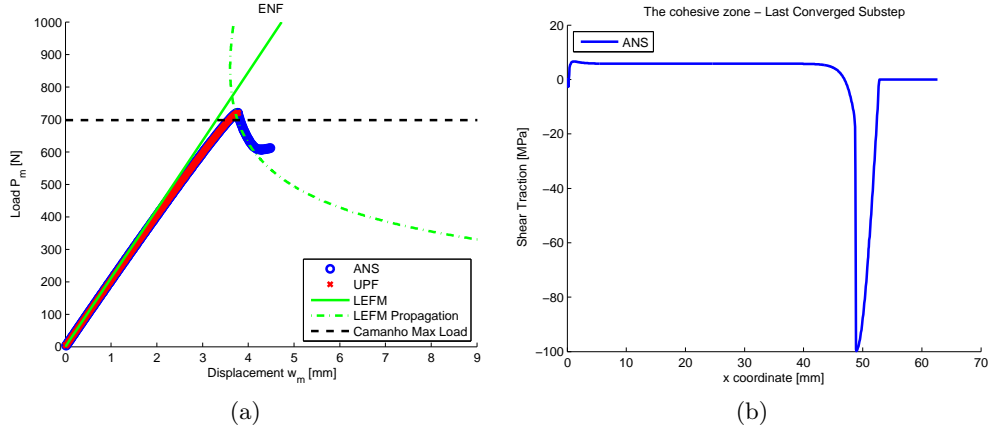


Figure 4.7: ENF test. a) Comparison of FEM, LEFM and Camanho. b) Plot of shear traction along the length in order to determine the length of the cohesive zone.

of iterations at this point are almost equal with 203 for UPF and 187 for ANS.

The cohesive shear traction for the last converged substep using ANS is plotted on Figure 4.7b. It can be seen that the crack has indeed extended beyond  $x = L/2$ . Furthermore it has a cohesive zone of 3.9 mm, corresponding to approximately 60 elements. Inspecting the UPF solution around the limit point, it is found, that the cohesive zone is approximately the same size.

Post Analysis ENF			
Dataset	Max Load [N]	Error vs. Experimental [%]	$L_{cz}$ [mm]
ANS	720.3	-1.9	3.9
UPF	720.4	-1.9	3.9
LEFM	771.1	5.0	-
Camanho FE	697.8	-4.9	-
Experimental	734.0	-	-

Table 4.6: Post analysis comparison of ENF results. Datasets 'Camanho' and 'Experimental' are from Camanho et al. (2003).

#### 4.3.4 MMB Test

From the results on Figure 4.8 it can be seen, that the ANS and UPF results are very similar up until near the limit point. It can also be seen, that the limit

points are no longer exactly the same, which is probably due to the different interaction criteria used in the ANS and the UPF. For all ratios but  $\theta = 4$ , solving much longer than the limit point was not possible. Beyond this, the same happened as in the ENF UPF run, i.e. the solver retraces steps along the unloading-curve and drifts back. This happened for all cases except when  $\theta = 4$ , where especially UPF converged longer.

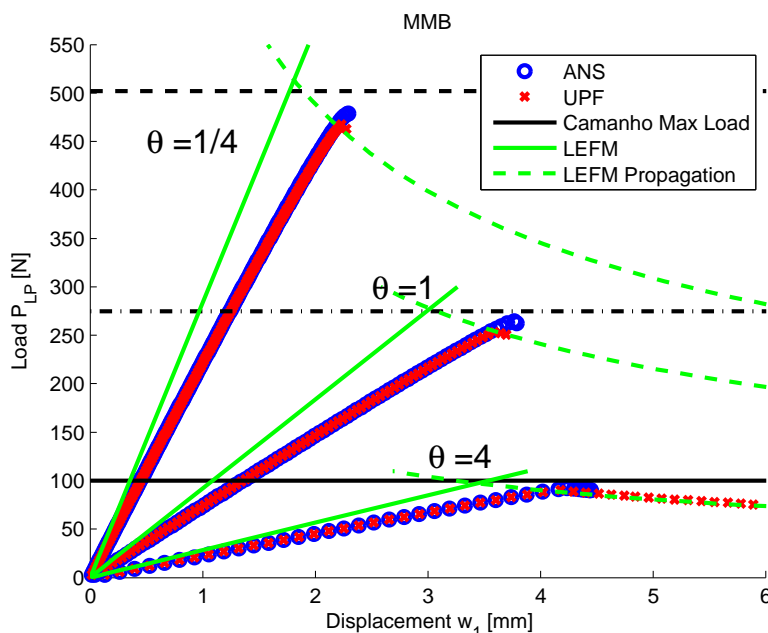


Figure 4.8: Load-displacement curves for the MMB test for three different ratios,  $\theta$ .

In Figure 4.9 the cohesive shear tractions are plotted for  $\theta = 1$ . Although both shear and normal tractions are present in the cohesive zone, it was found, that only the shear tractions reach the required onset traction and hence determines the length of the cohesive zone. The reason that the ANS and UPF data is seen to deviate in the beginning, is due to the chosen substeps respectively not being identical, and it is seen, that the crack has propagated a bit more for the UPF. The cohesive zone length data in Table 4.7 is obtained for termination displacements such that it is ensured, that similar substeps with similar crack lengths are being compared. It should be noted, that the peaks at  $x = 51$  correspond to where the load is applied, and a constant shear traction symmetric about this point can be seen.

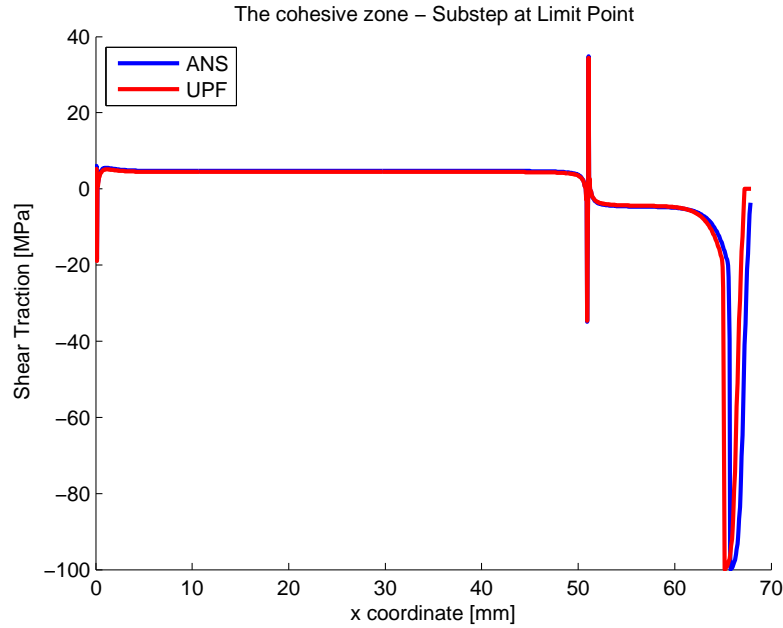


Figure 4.9: Cohesive traction plot for  $\theta = 1$  with ANS and UPF. Data is from substeps close to the limit point.

### 4.3.5 DCB Stiffness Explanation

The difference in stiffness between the LEFM beam model and the FE model of the DCB specimen can be attributed to the boundary conditions and the cohesive zone. This is clarified in the following, where an experiment on an FE model of a single beam (one arm of the test specimen) is carried out. Note that in order to compare with the LEFM solution, which is derived for an isotropic material, this model is using an isotropic material with  $E=122.7$  GPa and  $\nu = 0.25$ . In the LEFM beam model the load-displacement relation is based on a simple cantilever beam as seen on Figure 4.10a. In the FE model, the fixed end is not placed as in Figure 4.10a. Instead vertical supports are placed inbetween the fixed end and the crack tip due to symmetry, as seen in Figure 4.10b. This however influences the stiffness, and the tip displacement is approximately 8% larger due to this change in boundary conditions. The FE model is also more compliant due to the cohesive zone. Recall from Table 4.5 that the length of the cohesive zone is 0.9 mm. By inspection it is furthermore found that the maximum opening displacement in this zone is 0.02 mm. The effect of the cohesive zone is then estimated by removing

Post Analysis MMB					
$\theta = 4$	Max Load [N]	Error [%]	Iterations	Substeps	$L_{cz}$ [mm]
ANS	92.21	-14	276	32	1.5
UPF	89.99	-16	128	32	1.5
LEFM	97.25	-10	-	-	-
Camanho FE	99.9	-7.5	-	-	-
Experimental	108.1	-	-	-	-
$\theta = 1$	Max Load [N]	Error [%]	Iterations	Substeps	$L_{cz}$ [mm]
ANS	264.3	-4.0	390	87	1.9
UPF	253.1	-8.0	189	86	1.9
LEFM	277.5	0.8	-	-	-
Camanho FE	274.5	-0.3	-	-	-
Experimental	275.4	-	-	-	-
$\theta = 1/4$	Max Load [N]	Error [%]	Iterations	Substeps	$L_{cz}$ [mm]
ANS	478.5	-7.7	457	162	2.9
UPF	467.5	-9.9	387	161	2.9
LEFM	513.5	-1.0	-	-	-
Camanho FE	502.0	-3.2	-	-	-
Experimental	518.7	-	-	-	-

Table 4.7: Post analysis comparison of MMB results. Error is vs. Experimental. Datasets 'Camanho' and 'Experimental' are from Camanho et al. (2003). Iterations and substeps refer to the cumulative amount required to reach a  $w_1$  displacement of 4.2 mm, 3.58 mm, and 2.24 mm for  $\theta = 4$ ,  $\theta = 1$ , and  $\theta = 1/4$  respectively.

the vertical support over the 0.9 mm that would have been a cohesive zone, and then instead applying a vertical displacement of 0.02/2 mm at the end of this 'zone'. The factor of a half is due to symmetry. The partly removal of support and application of an 'opening displacement' is seen on Figure 4.10c and yields a difference of approximately 17%.

From these simple experiments, the load-displacement stiffnesses can be compared. The linear LEFM DCB curve has a slope of 83 N/mm, while ANS/UPF results yield a slope of 64 N/mm. The FE model in Figure 4.10c resulted in a slope of 68 N/mm. This was however found for the mentioned isotropic material. Using the full set of material parameters from Table 4.2, the configuration seen in Figure 4.10c yields 64 N/mm, which corresponds nicely to the seen stiffnesses in the FE simulations.

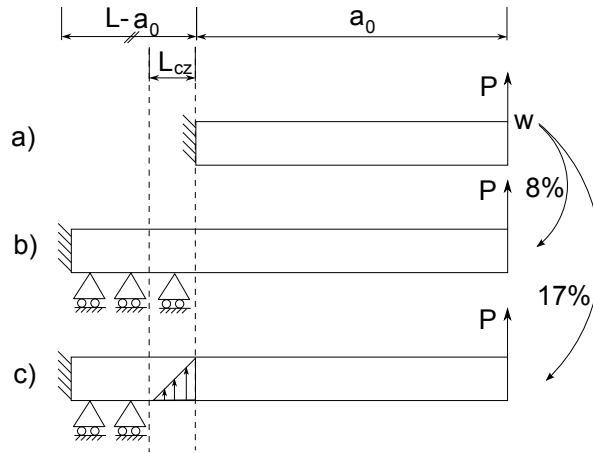


Figure 4.10: Effects of boundary conditions and cohesive zone on tip displacement. Lengths are not shown with true proportions.

#### 4.4 Influence of Onset Traction

In the above studies on the test specimens it was seen, that in order to use the high onset tractions used by Camanho et al. (2003), it was necessary to use a very fine mesh to obtain convergent models. This approach is a possibility in simple models, such as the specimen models, but for larger, more complex models, using an equally fine mesh will result in unacceptably time demanding analyses. In order to be able to use a more coarse mesh, the compromise that has to be made is to lower the onset traction. Therefore, in this section, the influence of the onset traction on results is examined in order to clarify, what this compromise means. In order to examine the influence of the choice of onset traction, the DCB specimen is used. The model is solved with the arc-length solver under load control, and the solution is set to automatically stop, when the crack has grown a specific distance. Referring to Figure 4.11, the solver is stopped, when the crack has grown so much, that the tip lies in a distance of  $L_{stop}$  from the clamped end. Here the crack tip is defined as the point in which full damage is evident. Hence in this test setup the solver is stopped, when the normal opening displacement,  $d_{stop}$ , in the distance,  $L_{stop}$ , from the clamped end first reaches  $\Delta_3^f$  (the opening displacement for full damage). The model is solved for different values of the onset traction, and the load-displacement data is stored. Furthermore, for the final solution (when the solver is stopped), the elastic energy in the structure (including the non-physical elastic energy in the cohesive elements) is recorded, and the energy dissipated in the cohesive

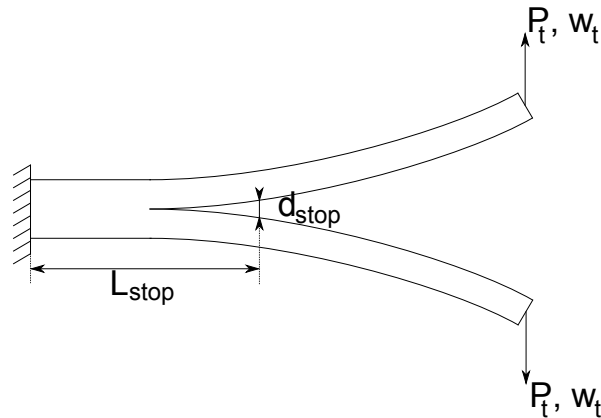


Figure 4.11: Additional measures used for the DCB model in examining the influence of the onset traction.

zone in the partially damaged cohesive elements during damage development is noted. The material data and geometry used for these tests are those from Camanho et al. (2003), which can also be seen in Table 4.2. Furthermore  $L_{stop} = L/7$ . The used discretisation is shown in Table 4.8. In Figure 4.12 the

Discretisation		
$n_{elem,L}$	$n_{elem,h}$	$n_{elem,t}$
1000	2	1

Table 4.8: The used discretisation.

force-displacement curves for the simulations performed using different values of the onset traction are shown. It is seen, that in the center region of the curves, all of the curves are coincident, meaning that the global response is identical here. However, in the beginning and end of the curves, differences are seen. It can be noted that generally, for lower values of the onset traction, unstable crack growth (occurring when the load supersedes the peak load) sets in at a lower external force as would be expected, but also for a larger displacement. On the figure, the endpoints of the load-displacement curves are connected to origo of the coordinate system, to make the endpoints visible. Here it is seen, that for lower onset tractions, the crack reaches its final length for larger displacements. From these two observations it seems, that lowering the onset traction provides for more compliant responses, but that the global responses over most of the curves are identical. This shows, that the value of the onset traction is less important w.r.t. crack propagation. In order

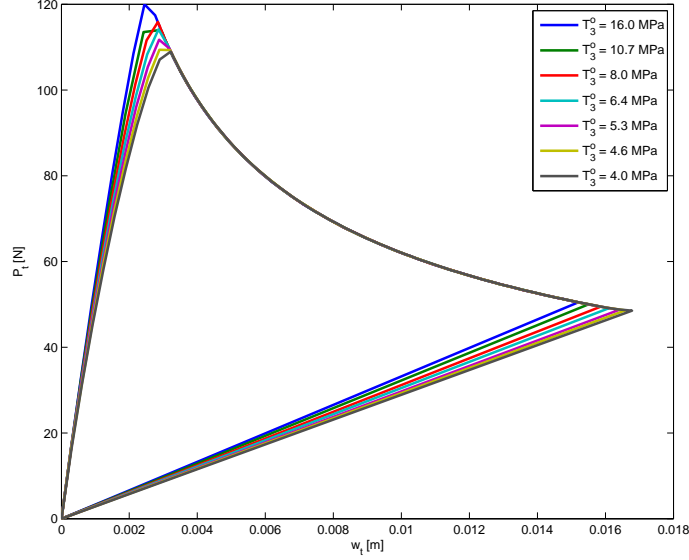


Figure 4.12: Force-displacement curves for different values of the onset traction.

to further investigate the influence, the critical energy release rate for each simulation is calculated as

$$G_c = \frac{2 \int P_t dw_t - U}{A_{crack}} \quad (4.4.1)$$

where  $A_{crack}$  is half the developed crack face area (the projected crack area), and  $U$  is the remaining elastic energy in the model, that would be retrieved upon unloading. This energy release rate is compared to the critical energy release rate of the material, and the relative error is plotted in Figure 4.13a. Here it is seen, that lower onset tractions give higher errors in  $G_c$ . This can be explained by looking at the energy dissipated (during damage development) in the cohesive zone,  $E_{dis}$ .  $E_{dis}$  is calculated as shown in Appendix B. This energy is plotted in Figure 4.13b. Comparing Figures 4.13a and 4.13b it is seen, that the two curves are much alike, which serves to show, that this energy is to blame for the error. This can also be seen by considering the corrected critical energy release rate which is calculated as

$$G_{c,corrected} = \frac{2 \int P_t dw_t - U - E_{dis}}{A_{crack}} \quad (4.4.2)$$

The corrected critical energy release rate is also plotted on Figure 4.13a. Here it is seen, that the critical energy release rate is almost exactly met as expected, and also that it seems to be independent of the onset traction. As

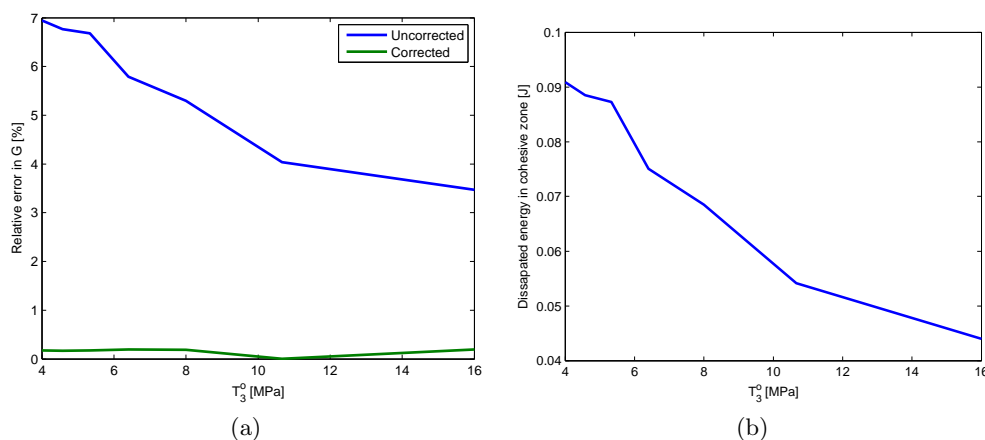


Figure 4.13: a) The relative error in critical energy release rate for both uncorrected and corrected calculations. b) The dissipated energy in the cohesive zone.

seen on Figure 4.13b, the lower the onset traction, the more energy is dissipated in the cohesive zone, which must mean, that the cohesive zone is larger. A larger cohesive zone also means a larger number of CZ elements in the cohesive zone, and this shows why convergence is improved by lowering the onset traction (Turon et al., 2007).

In order to draw further conclusions on the influence, another experiment has been performed on the DCB specimen. Here the force needed for unstable crack development is recorded for different combinations of initial specimen crack length and onset traction. A plot of the data obtained from this experiment is shown in Figure 4.14. In this figure it is seen, that at small crack lengths the onset load is very dependent on the onset traction, whereas at large crack lengths the onset load is practically independent of the onset traction. This again indicates, that the onset traction has less importance for crack propagation. It furthermore shows that, at least for the DCB specimen, crack initiation is highly dependent of the onset traction, since crack initiation can be seen as the limit case of decreasing crack length. This has the implication, that care must be taken, if crack initiation is to be examined using CZ elements.

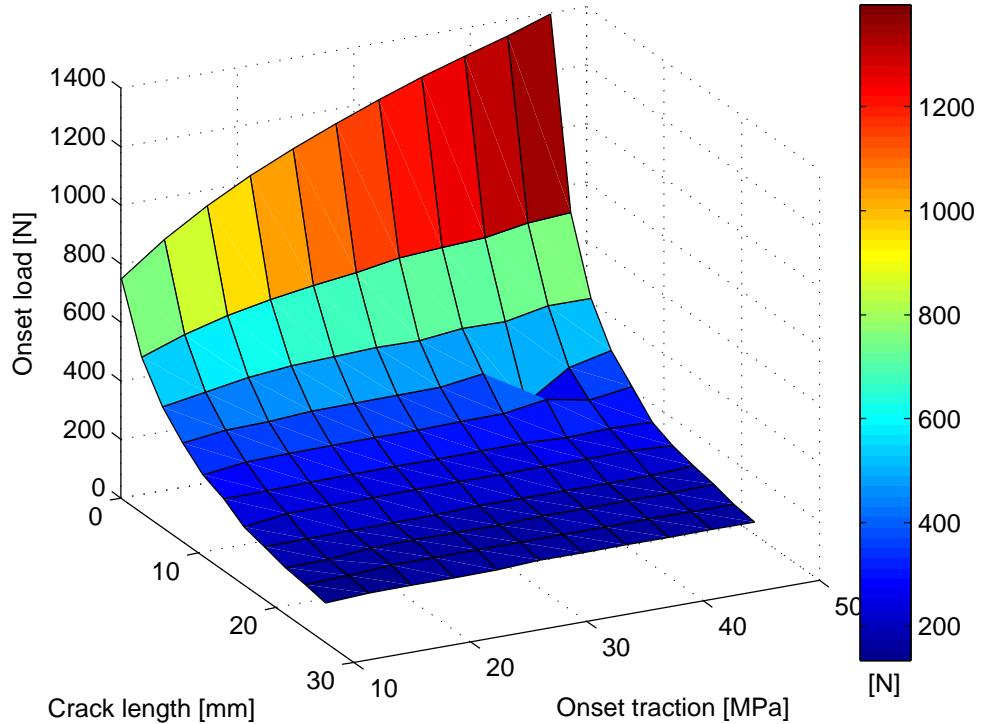


Figure 4.14: Predicted load for unstable crack growth as function of crack length and onset traction.

## 4.5 Conclusion

In this chapter it has been verified, that the UPF is working as expected. In examining the one element model it has been found, that the results from the element are invariant under rigid body translations and rotations, and that the correct traction-opening response is obtained. This shows, that the constitutive model and the element kinematics are correctly implemented. By comparing FE results with results obtained analytically and those obtained by Camanho et al. (2003), it is also verified, that the modelling approach (e.g. how the model is meshed with cohesive elements) is working, and it is demonstrated, that the computation of the element tangent stiffness matrix is correct. Finally the influence of the onset traction on obtained results was also investigated, and it was found, that the onset traction has a big influence on the onset load for crack growth for small crack lengths, but that the influence becomes insignificant for long cracks.

## **Part II**

# **Analysis of Wrinkle Defect**



## Chapter 5

# Verification of FE Wrinkle Model

The overall purpose of this part of the thesis is to create an FE model of a sandwich wrinkle defect, which is capable of accurately predicting failure loads. This chapter serves to describe the used FE model, and to verify it through linear analyses. This is done by comparing FE results with Digital Image Correlation (DIC) measurements performed by Leong (2012) on an undamaged specimen. The load distribution in the wrinkle is also explained using a simple beam model.

### 5.1 Parametrisation

In the following section different parts of the wrinkle geometry will be discussed. The naming of the different parts can be seen in Figure 5.1a, and will be referred to in italic. Note that in the figure the names *FM1 Interface* and *FM2 Interfaces* occur. These interfaces are named according to the failure modes that Leong (2012) observed. Hence in Failure Mode 1 (FM1) debonding occurred, between the facesheet containing a wrinkle defect and the core, in the *FM1 Interface*. In Failure Mode 2 (FM2) debonding occurred, between the individual plies of the aforementioned facesheet, in the *FM2 Interface*. The naming presented in the figure will be used in the rest of the thesis.

The changeable parameters of the FE model were chosen as those listed in Table 5.1. Parameters coupled to the global geometry are illustrated in Fig-

ure 5.1b. The ply numbering is used for the ordering of data in the arrays  $\{m\}$  and  $\{\theta\}$ , which are described in Table 5.1. Besides the parameters seen on Figure 5.1b, the parameters coupled to the geometry of the *Epoxy Inclusion* are shown in Figure 5.2. Even though they are not listed in Table 5.1, CZM properties can also be changed. The amount of parameters allows for adjusting the wrinkle defect geometries to be similar to those examined by Leong (2012), as well as studying the influence of selected parameters on specimen strengths.

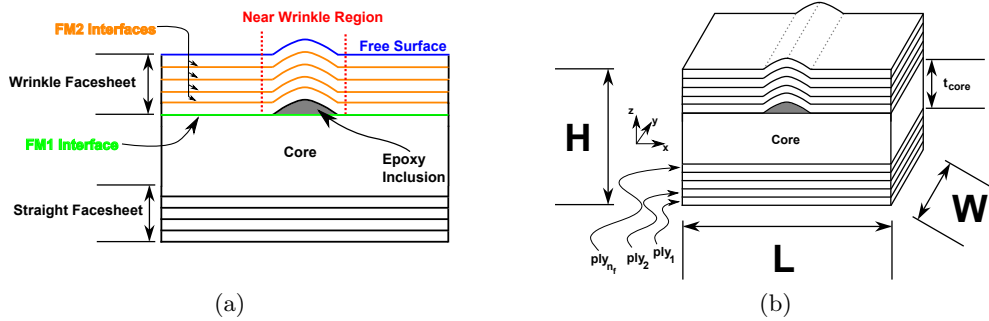


Figure 5.1: Illustration of a) the different terms used when parts of the wrinkle geometry are discussed and b) the ply numbering in the FE model along with some of the geometrical parameters.

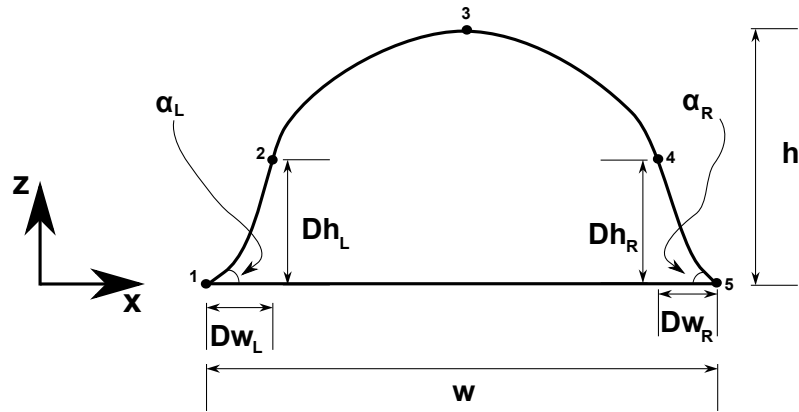


Figure 5.2: Illustration of changeable geometrical parameters modelling the geometry of the *Epoxy Inclusion*.

Parameters	Shown on Figure 5.1b
$L$	Length of specimen.
$W$	Width of specimen.
$H$	Height of specimen.
$t_{core}$	Thickness of core material.
$n_f$	Number of layers in facesheet.
Shown on Figure 5.2	
$w$	Width of wrinkle.
$h$	Height of wrinkle.
$Dw_L$	Distance in x-direction from point 1 to point 2.
$Dh_L$	Distance in z-direction from point 1 to point 2.
$\alpha_L$	Starting angle of spline 123
$Dw_R$	Distance in x-direction from point 4 to point 5.
$Dh_R$	Distance in z-direction from point 4 to point 5.
$\alpha_R$	Ending angle of spline 345
Not Illustrated	
$\{m\}$	Array containing material type of layer $n$ .
$\{\theta\}$	Array containing fiber orientation according to the global x-axis of layer $n$ .

Table 5.1: Changeable variables in the FE model.

## 5.2 Modelling

The wrinkle geometry is modelled by two splines. One spline from point 1 through point 2 to point 3 seen on Figure 5.2, and another spline connecting point 3-4-5. By using splines for the wrinkle geometry it is possible to create various wrinkle shapes, and it is judged that the geometry for a wide range of wrinkles/epoxy inclusions can be approximated in this way. A comparison of the geometry for the FE model and the physical specimen investigated by Leong (2012) is shown in Figure 5.3. As seen the geometry of the *Epoxy Inclusion* seems well approximated. The splines used for modelling the *Epoxy Inclusion* are then scaled outwards in order to create the geometry of the facesheet plies. The splines can then be connected by lines, such that the splines and connecting lines encircle closed areas. These areas are then extruded in order to create volumes. All volumes in the model consist of six areas, such that the mapped meshing function of ANSYS can be used along with built in features for properly orienting the element coordinate systems. Boundary conditions used to simulate the compression test carried out by

Leong (2012) can be seen in Figure 5.4. This type of boundary condition is different from the one used by Leong (2012) for his FE analysis. Leong (2012) modelled the compression test by attaching a steel block to the FE model, and then applying a pressure on the steel block. In this way Leong (2012) could apply a given pressure directly to the model. By applying a displacement boundary condition, as done here, the pressure applied to the model can be computed after the simulation is done by obtaining the reaction loads. A displacement boundary condition was chosen, since it makes the problem computationally more easy to solve, because the Newton-Raphson algorithm can be used to trace the entire equilibrium path.

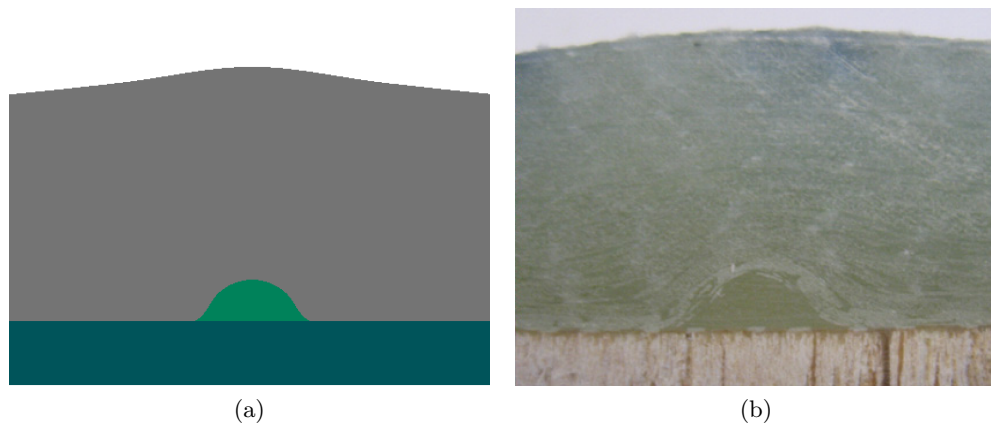


Figure 5.3: Comparison of test specimen geometry with modelled geometry. a) Shows modelled geometry and b) shows geometry of wrinkle in physical specimen.

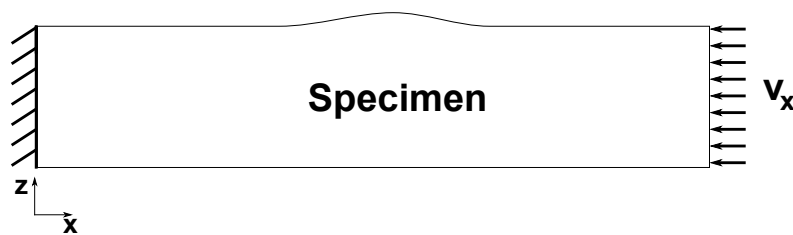


Figure 5.4: Illustration of the applied boundary conditions.

### 5.3 Meshing

The entire model is meshed with a compatible mesh. In order to limit the influence from a changing mesh when changing the geometrical parameters, the number of elements on all lines in the model is specified. Nine parameters regarding the number of elements on different lines can be set. These parameters are listed in Table 5.2 and sketched on Figure 5.5. An illustration of what the mesh looks like in the *Near Wrinkle Region* can be seen in Figure 5.6a. As seen a structured mesh is obtained. It has been verified, that the element coordinate systems have been oriented properly. After meshing with structural solid elements, CZ elements can be added in the FM1 and FM2 interfaces. CZ elements will however not be used in the present chapter. A plot of the CZ elements in the FE model can be seen on Figure 5.6b.

Parameters	Shown on Figure 5.5	Name
	Elements in the width of the specimen.	CE1
	Elements in straight part of plies.	CE2
	Elements in the thickness of each ply.	CE3
	Elements in the thickness of the core.	CE4
	Elements in bottom of <i>Epoxy Inclusion</i> .	CE5
1	Elements on spline 1.	CE6
2	Elements on spline 2.	CE7
3	Elements on spline 3.	CE8
4	Elements on spline 4.	CE9

Table 5.2: Changeable variables that influence the mesh in different regions of the FE model. The last column represents the names of the variables used for referencing later on in the thesis.

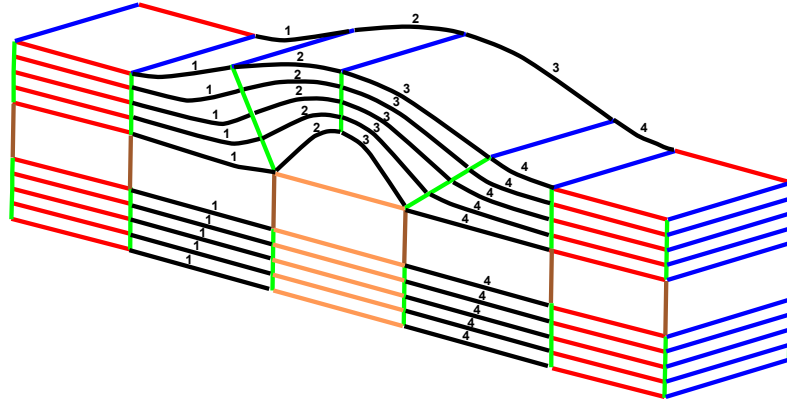


Figure 5.5: Illustration of the different lines with mesh control.

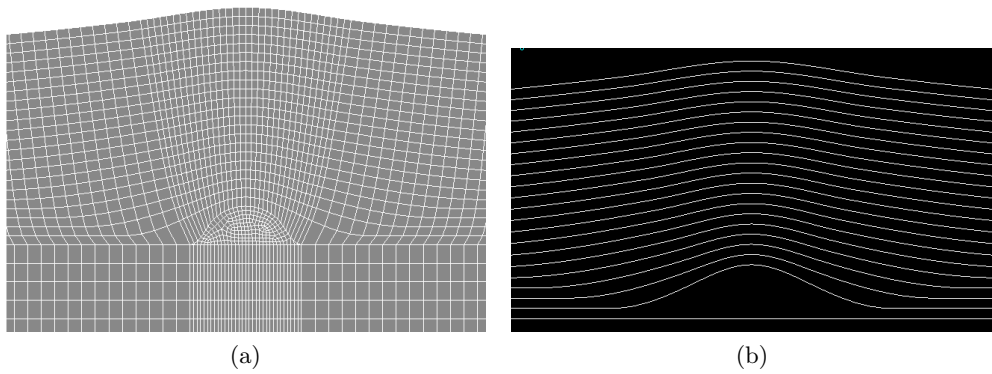


Figure 5.6: Illustration of a) structural mesh and b) CZ elements in the FM1 and FM2 interfaces.

## 5.4 Comments to Leong (2012)

In order to simulate the results obtained by Leong (2012) in the best possible way, the author has been contacted to get additional details for the content of the article. In the below list, a compilation of additional details and corrections for the articles is given:

- The DIC measurements are given for specimen 5.
- The failure loads in Leong (2012, Table 4) were misprinted. The correct loads are given in Table 5.3. Note that the pressures given are the face sheet pressures.
- The widths of the tested specimens,  $W$ , were 40 mm, not 30 mm.
- Some values in the material data were misprinted. The correct values are given in Table 5.4.

The authors of this thesis would like to thank Martin Leong for kindly providing these corrections and additional details.

Failure Loads			
Specimen	FM2 Load (MPa)*	FM2 Load (kN)	FM1 Load $\approx 0.8$ FM2 (kN)
1	188	154	123
2	174	143	114
3	208	170	136
4	164	134	107
5	163	133	107
6	195	160	128
7	197	162	129
8	164	134	107

Table 5.3: Specimen failure loads from Leong (2012). \* means corrected w.r.t. to the width misprint. The loads are calculated from the facesheet area of  $40 \text{ mm} \cdot (30 \text{ mm} - 9.5 \text{ mm})$ .

Updated Balsa Properties								
$E_{11}$	$E_{22}$	$E_{33}$	$G_{12}$	$G_{13}$	$G_{23}$	$\nu_{12}$	$\nu_{13}$	$\nu_{23}$
0.4 GPa	0.4 GPa	4 GPa	1.6* GPa	1.6* GPa	1.6* GPa	0.1	0.2*	0.2*
Updated UD Properties								
$E_{11}$	$E_{22}$	$E_{33}$	$G_{12}$	$G_{13}$	$G_{23}$	$\nu_{12}$	$\nu_{13}$	$\nu_{23}$
43 GPa	14 GPa	14 GPa	4.5 GPa	4.3 GPa	2.0 GPa	0.3	0.3*	0.1

Table 5.4: Material properties for the balsa core and UD plies. \* denotes a corrected value, recieved from the author of Leong (2012).

## 5.5 Comparison with DIC before FM1

The FE model will in this section be compared to experimental DIC results obtained by Leong (2012) for an undamaged specimen. All the needed files for the FE model used in this chapter can be found on the attached CD in the folder 'Models\Linear Wrinkle'. As mentioned previously, CZ elements are not used in this FE model. The mesh and geometrical parameters used for the FE model can be seen in Table 5.5. Note that in the FE model  $W = 10$  mm is used, whereas the real specimen width is  $W = 40$  mm. It was checked, that decreasing the thickness to 10 mm and only having one element in this direction did not have any significant influence on the obtained strain fields. The facesheet layup is  $[(\text{Biax} @ \pm 45), (\text{UD} @ 0)]_s$  (Leong, 2012). All DIC strain plots are normalised w.r.t. the far field strain (Leong, 2012). The value of this far field strain is however not known. Therefore it is chosen to normalise FE strain results w.r.t. the average value of the normal strain, i.e. applied displacement divided by specimen length.

Geometric Parameters					
$L$	$H$	$W$	$t_{core}$	$h$	$w$
143 mm	30 mm	10 mm	9.5 mm	2.25 mm	6.25 mm
$n_f$	$Dw_L = Dw_R$	$Dh_L = Dh_R$	$\alpha_L = \alpha_R$	$v_x$	
22	0.288 mm	1.25 mm	10 °	-0.1 mm	
Mesh Parameters					
CE1	CE2	CE3	CE4	CE5	CE6
1	20	4	20	100	200
CE7	CE8	CE9			
100	100	200			

Table 5.5: Parameters used for the FE model.

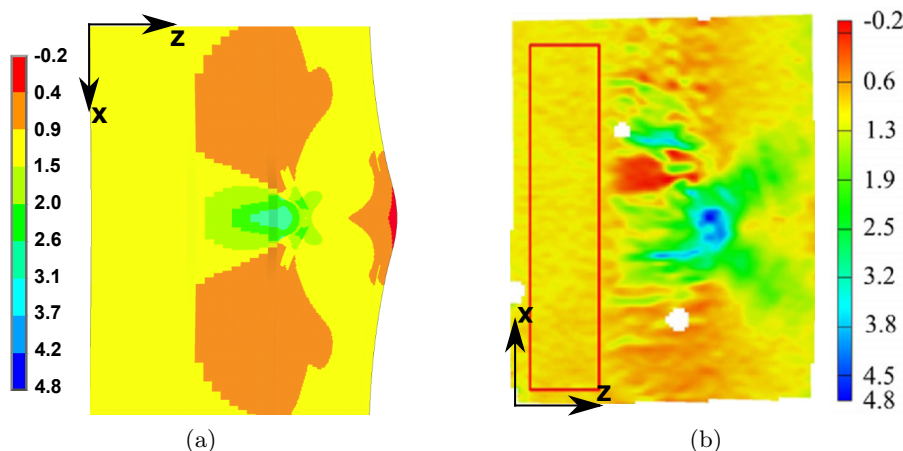


Figure 5.7: Plot of the normalised normal strain ( $\epsilon_x$ ) for a) FEA and b) DIC results from Leong (2012).

Figures 5.7a and 5.7b show a comparison of the normal strain in the x-direction. The results seem to correlate well in terms of values. Some trends are however not seen in the FE model, e.g. the "green arms" do not extend as far as in the DIC measurements. This is mainly due to using the same contour limits, and the same trends are thus seen on automatically adjusted contours.

In Figures 5.8a and 5.8b a comparison of the transverse normal strain can be seen. The transverse normal strain is lower in the FE model, which is why different contour limits have been used. Having different limits, the same trends can however be seen. The strain around the *Epoxy Inclusion* seems to be approximately a factor of two lower in the FEA compared to DIC.

In Figures 5.9a and 5.9b a comparison of the transverse shear strain can be seen. The values and distribution seem to match the DIC measurements well. The DIC measurements have a spot of large transverse shear strain, which is not caught by the FE model. The reason for this is expected to be an error in the measurement.

The minor differences in normalised strain values of  $\epsilon_x$  and  $\gamma_{xz}$  might be attributed to the limited precision of the DIC measurements, as Leong (2012) states himself. Furthermore some uncertainty is also associated with the given material properties. An explanation for the fact that  $\epsilon_z$  does not correspond

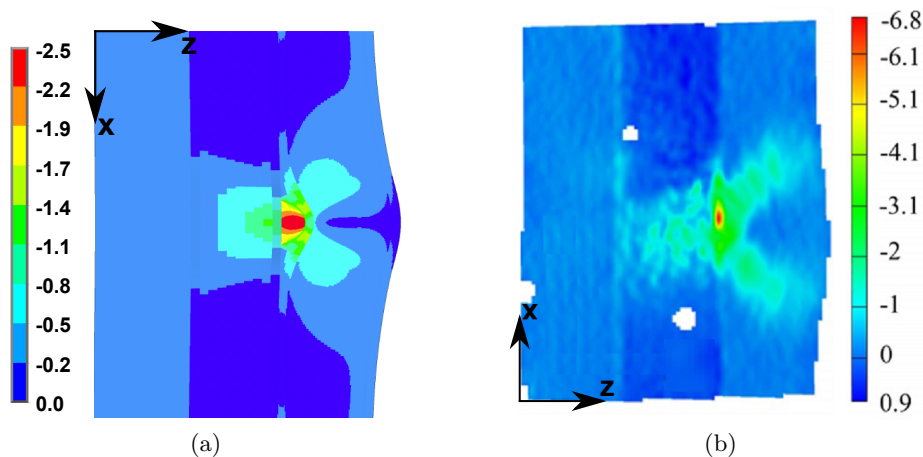


Figure 5.8: Plot of the normalised transverse normal strain ( $\epsilon_z$ ) for a) FEA and b) DIC results from Leong (2012).

as well as  $\epsilon_x$  and  $\gamma_{xz}$  has not been found. Possible reasons include the mentioned inaccurate material properties, differences in geometry and difference in normalisation.

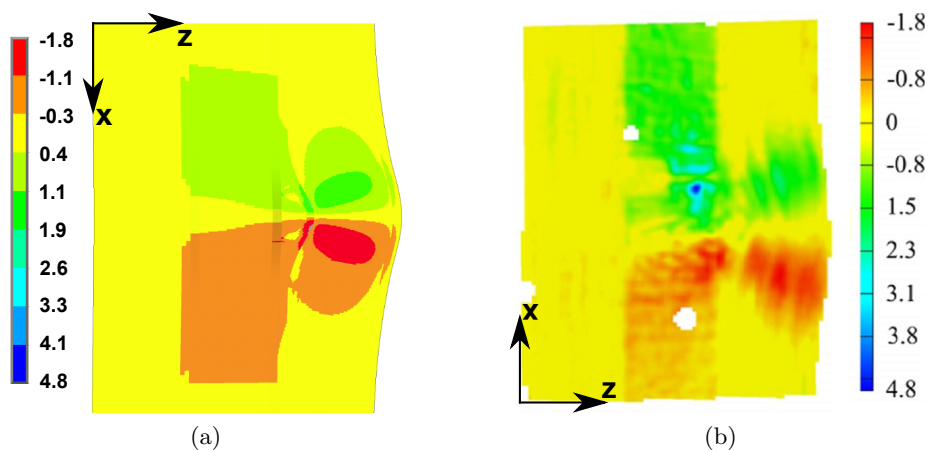


Figure 5.9: Plot of the normalised transverse shear strain ( $\gamma_{xz}$ ) for a) FEA and b) DIC results from Leong (2012).

## 5.6 Physical Interpretation

This section serves to provide an explanation of the strain distributions seen in the *Near Wrinkle Region* in section 5.5, and thus also serves as an intuitive check on the validity of the FE model. The strain distribution will be explained by the use of a simplified model of the wrinkle defect. A symmetric sandwich laminate under compression can be considered as three springs connected in parallel, where the facesheets constitutes two stiff springs, and the core material constitute one compliant spring. When a wrinkle defect is inherent in the *Wrinkle Facesheet*, the *Near Wrinkle Region* will not have the same stiffness as the rest of the *Wrinkle Facesheet* nor the stiffness of the *Straight Facesheet*. This is because the inplane stiffnesses of the plies are no longer in the same direction as the load in the *Near Wrinkle Region*. The *Near Wrinkle Region* will therefore constitute a slightly more compliant spring. A symmetric sandwich laminate containing a wrinkle defect can therefore be modelled as the spring system shown in Figure 5.10. If a displacement boundary condition

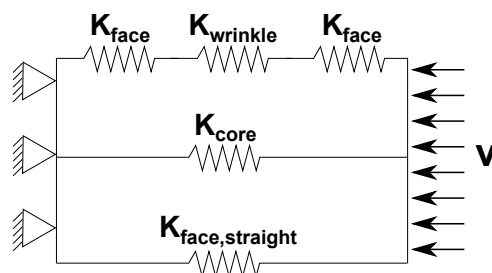


Figure 5.10: Illustration of a simple equivalent spring model.

as the one described in section 5.2 is applied to the sandwich laminate, the result is, that the *Straight Facesheet* will carry more load than the *Wrinkle Facesheet*. In the following a closer look is taken at the *Wrinkle Facesheet* in order to determine, how loads are transferred within this facesheet. It will be assumed, that the *Wrinkle Facesheet* can be approximated as four connecting beams as sketched by the red line in Figure 5.11a, and that the influence of the *Epoxy Inclusion* can be disregarded. The two beams parallel to the global x-axis will not be considered further. From the beams non-parallel to the global x-axis it is seen, that they are not aligned with the load, and therefore they have to act as beams, meaning that they will be affected by a shear force, normal force, and a bending moment. Assuming a symmetric wrinkle and denoting the load and geometric parameters as done in Figure 5.11b, the

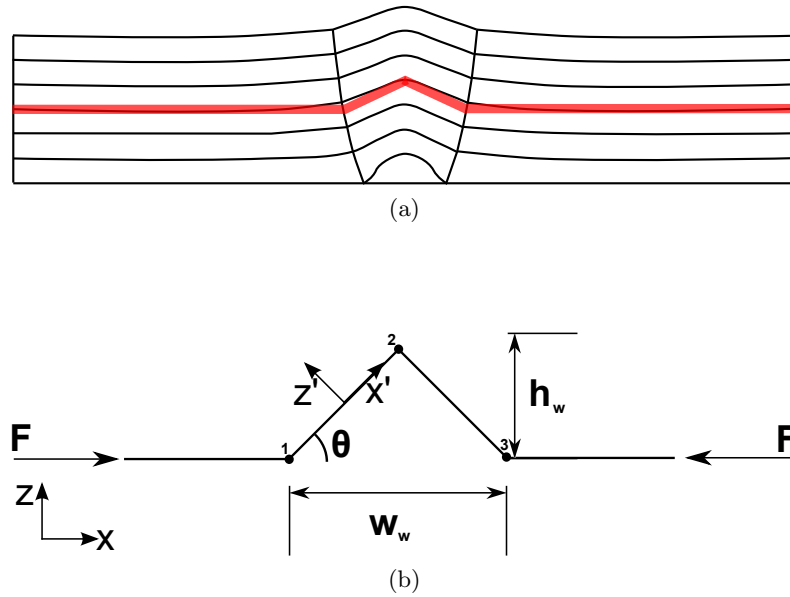


Figure 5.11: Illustration of a) how dimensions for the beam model are determined and b) parameters used for beam calculations.

angle  $\theta$  between the load,  $F$ , and the beam 1-2 and 2-3 on Figure 5.11b can be determined as:

$$\theta = \tan^{-1} \left( \frac{2h_w}{w_w} \right) \quad (5.6.1)$$

Since the problem is symmetric, only the beam 1-2 will be considered in the following. The beam will be modelled as a fixed-end beam like the one shown in Figure 5.12. In the figure it is seen that the compressional loading force  $F$

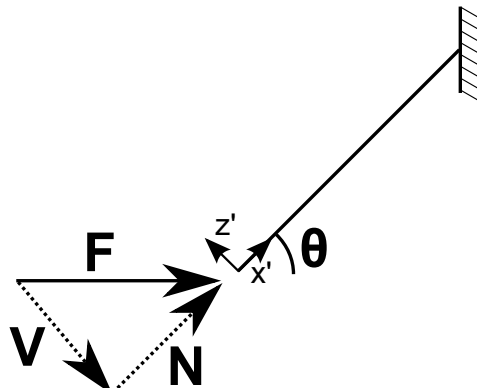


Figure 5.12: Illustration of the beam model from point 1 to 2 on Figure 5.11b.

will be transferred in the *Near Wrinkle Region* as a normal force,  $N$ , and a shear force,  $V$ , given by:

$$N = \cos(\theta)F \quad (5.6.2)$$

$$V = \sin(\theta)F \quad (5.6.3)$$

The normal force will act in the in plane direction of the plies and will be less than in the regions, where the facesheet is parallel to the loading direction. Therefore it is not judged as detrimental. The shear force however act out of plane, where the plies have a low stiffness as well as strength and is therefore expected to be detrimental for sufficiently big angles  $\theta$ . In order to verify that the above provided physical reasoning in the *Near Wrinkle Region* is capable of describing the overall physics of the wrinkle defect, the strains obtained from the validated FE model and the simple beam model will be compared in the following. Note that the angle is taken as  $17^\circ$ . The average strain, to be used for normalising results, is taken as:

$$\epsilon_x^{avg} = \frac{v_x}{L} \quad (5.6.4)$$

The compressional force,  $F$ , transferred in the top facesheet is found by reading off the reaction load in the facesheet. The normal strain due to the normal force and bending respectively can be calculated as:

$$\epsilon_x^N = a_{11} \frac{N}{W} \quad (5.6.5)$$

$$\epsilon_x^B[z'] = \kappa_{x'} z' = d_{11} \frac{M_{x'}}{W} z' = d_{11} \frac{V x'}{W} z' \quad (5.6.6)$$

where  $a_{11}$  and  $d_{11}$  are respectively the 11 entry and 44 entry of the CLT compliance matrix. The shear strain will be assumed uniform through the cross section (even though this of course is not physically possible due to the fact, that equilibrium will not be satisfied on the *free surface*). The shear stiffness is taken as a weighted average of the out of plane shear stiffness for the UD and Biax plies. The shear strain can therefore be calculated as

$$\gamma_{x'z'} = \frac{V}{h_{beam} W \left( \frac{n_{UD}}{n_{plies}} G_{xz}^{UD} + \frac{n_{BIAx}}{n_{plies}} G_{xz}^{BIAx} \right)} \quad (5.6.7)$$

where  $h_{beam}$  is the height of the *Wrinkle Facesheet* in the *Near Wrinkle Region*. In Figure 5.13 contour plots of the normal strain,  $\epsilon_{x'}$ , and the shear strain,  $\gamma_{x'z'}$ , in the *Near Wrinkle Region* are shown. The path sketched on

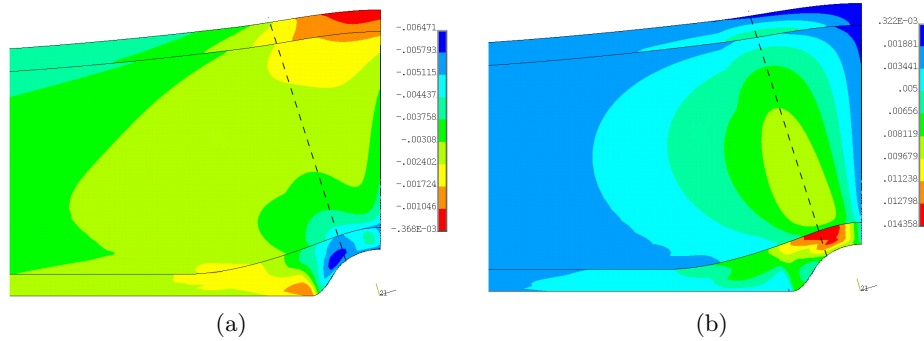


Figure 5.13: Contour plot of a) the normal strain and b) the shear strain in the coordinate system  $x'z'$ . Furthermore the path used for obtaining through thickness strains is shown with a dashed line.

both pictures is the path used for obtaining through thickness strains for the comparison of the two models. Plots of the through thickness strains in the two models can be seen in Figures 5.14a and 5.14b. From these figures it is seen, that the normal strain correlates decently in terms of both values and trend. The constant shear strain approximation is close to the maximum shear strain. An obvious flaw in the beam model is, that it does not take the curved nature of the plies close to the wrinkle into account. The curved nature of the plies means that the angle,  $\theta$ , changes through the plies. Although the beam model does not provide accurate results, it gives a physical explanation of the strain distribution seen in the specimens, and gives an intuitive understanding of the influence of key geometrical parameters of the wrinkle defect.

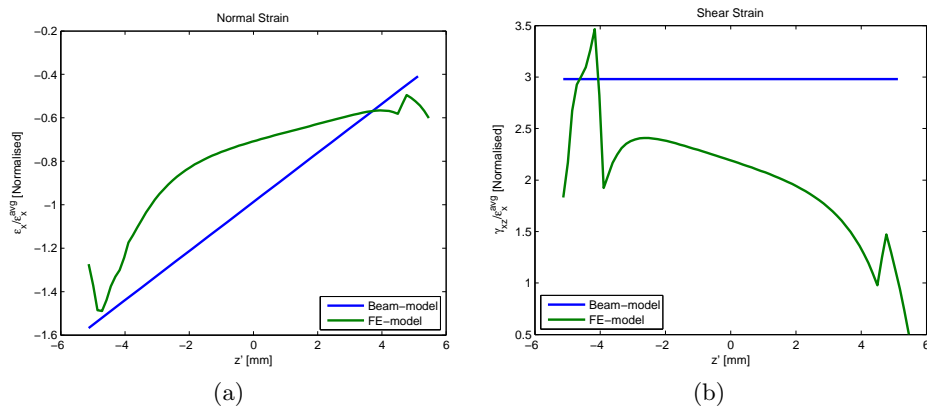


Figure 5.14: Graph of through thickness strains. a) Shows the normal strain and b) shows the transverse shear strain.

## 5.7 Conclusion

In this chapter the parametrisation and the modelling of the wrinkle defect were described. It was found, that the way the wrinkle model was build made it possible to approximate the wrinkle geometries of the test specimens tested in Leong (2012) well. Further on when comparing results obtained from the FE model with results obtained from DIC an acceptable correlation was found. In the end of the chapter a phenomenological explanation of the load distribution was given using a simple beam model. It was found, that a simple beam model could explain the tendencies seen in strains in the *Near Wrinkle Region*. However as expected it was also found, that a beam model is overly simple in order to analyse a wrinkle defect thoroughly.



## Chapter 6

# Delamination in a Wrinkle Defect

This chapter serves to describe analyses of the wrinkle defect using CZ elements, as well as the results obtained from the analyses. The CZM properties used are given in Appendix A, and have been obtained from delamination tests such as those described in Chapter 2. In order to ensure, that the model represents the physical phenomena seen by Leong (2012), the model is verified in a two step procedure, which is sketched in the flowchart on Figure 6.1. First CZ elements are introduced in the model only in the *FM1 Interface* seen on Figure 5.1a. The results obtained from this model will then be compared to those found by Leong (2012), to see if the strain fields match. Second CZ elements are introduced in the *FM2 Interfaces* to see, whether the delamination between plies at the FM2 Load can be simulated. It was not possible to simulate the delamination at the FM2 load, since the required onset tractions were too high and therefore gave nonconvergent solutions. Instead of simulating delamination at the FM2 load, the strength of the specimen will be characterised using the Max Stress Criterion. A short discussion of the damage process and the mode mixity in the *FM1 Interface* and the *FM2 Interfaces* are also to be found in this chapter.

### 6.1 Modeling FM1

CZ elements are included in the *FM1 Interface*. Using the CZM properties for laminated glass-epoxy given in Appendix A, Table A.1, in the *FM1 Interface*

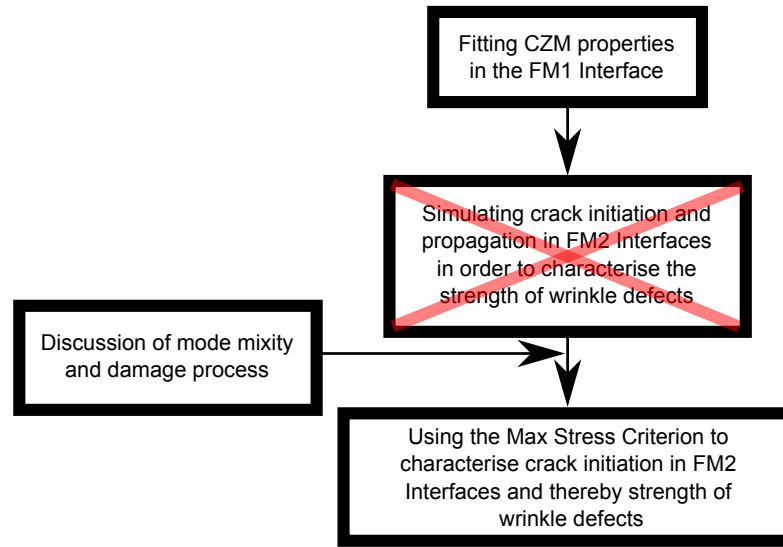


Figure 6.1: Flowchart of the approach taken in order to adjust material parameters, such that the FM1 and FM2 loads can be simulated properly.

results in delamination initiating at too high loads. It is assessed, that this is due to the used interface properties being obtained from UD/UD tests, whereas the *FM1 Interface* is balsa/Biax. Due to this the CZM properties will be fitted, until reasonable results are obtained, by a trial and error process. From Leong (2012) it is known, that the FM1 load lies in the range of 70% – 90% of the FM2 load. Using 80%, this gives an FM1 load of 107 kN for specimen 5. However the FM1 load is defined as the load where a visible crack has developed in the *FM1 Interface*, and hence the length of the debond or when debonding initiates is not known. From correspondance with the author of Leong (2012) it is known, that the crack has a significant length at approximately 100 kN. A significant length is subjectively interpreted as 8 mm. A crack length of 8 mm was obtained at 100 kN by using the reduced CZM properties listed in Table 6.1. These properties resulted in delamination initiation at 90 kN, and a crack length of 19.5 mm at the FM2 load. Note that the definition of crack length used here is the length of the interface, where complete delamination has occurred, meaning that  $\Delta^f$  has been exceeded. The fitted CZM properties are reduced a lot compared to those in Table A.1 and may be based on wrong assumptions, e.g. the 8 mm crack length. However the large reduction might be justified as being due to residual stresses or microcracks between the *Epoxy Inclusion* and the core.

All parameters used in the model for the following comparison with DIC are listed in Table 6.1, and the used FE model can be found on the attached CD in the folder 'Models\FM1 Wrinkle'.

Geometric Parameters					
$L$ 143 mm	$H$ 30 mm	$W$ 10 mm	$t_{core}$ 9.5 mm	$h$ 2.25 mm	$w$ 6.25 mm
$n_f$ 22	$Dw_L = Dw_R$ 0.288 mm	$Dh_L = Dh_R$ 1.25 mm	$\alpha_L = \alpha_R$ 10 °	$v_x$ -0.58 mm	
Fitted FM1 CZM Properties					
$G_{Ic}$ 88 J/m <sup>2</sup>	$G_{IIc}$ 320 J/m <sup>2</sup>	$T_3^0$ 3 MPa	$T_s^0$ 5.5 MPa	K 10 <sup>5</sup> N/mm <sup>3</sup>	$\eta$ 1.4
Mesh Parameters					
CE1 1	CE2 20	CE3 2	CE4 10	CE5 100	CE6 200
CE7 100	CE8 100	CE9 200			

Table 6.1: Parameters used in the FE model.

In order to further verify, that the fitted CZM properties give comparable results, contour plots of the strain distributions obtained from the FE analysis beyond FM1 can be seen in Figures 6.2 to 6.4. In these figures the DIC measurements obtained by Leong (2012) after FM1 are also seen. Both the FE and DIC plots are normalised as described in section 5.5. From the contour plots it is seen, that in terms of values the strain fields from the FE model for the normal strain  $\epsilon_x$  and the transverse shear strain  $\gamma_{xz}$  fit the results obtained by DIC well. The strain field for the transverse normal strain,  $\epsilon_z$ , is, as also seen in section 5.5, a bit lower in the FE model than in the DIC measurements. This might be attributed to unprecise material data and the difference in normalisation. In general it is however seen, that the presence of a crack in the *FM1 Interface* increases the strains in the *Near Wrinkle Region*. This means, that the simulation of crack propagation between balsa and the *Wrinkle Facesheet* provides more reliable results, since a linear analysis does not provide these increased strains. In terms of the distribution of the different strain fields, all plots are seen to fit the DIC measurements well. It is therefore judged, that with the fitted CZM properties the model is capable of simulating the failure process of a wrinkle defect up to and beyond the FM1 load.

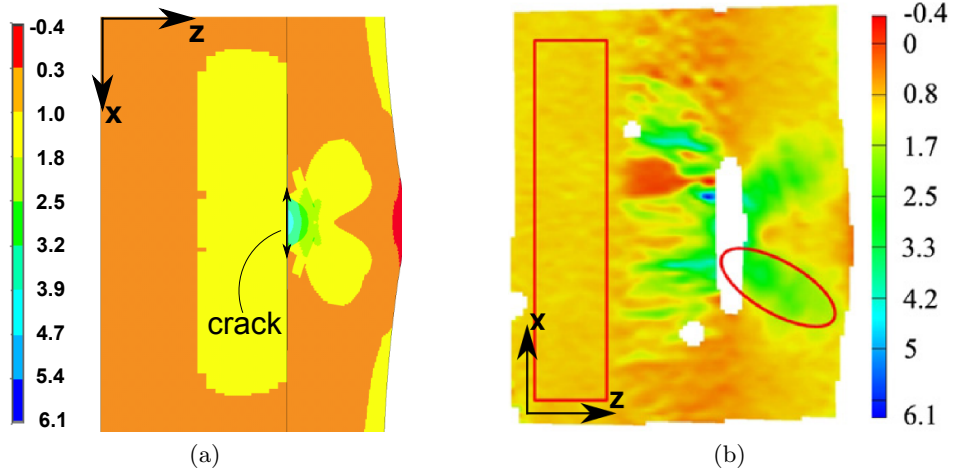


Figure 6.2: Plot of the normal strain ( $\epsilon_x$ ) after FM1 as a) obtained from FEA and b) obtained with DIC (Leong, 2012). Both plots are normalised with respect to the far field normal strain  $\epsilon_x^{avg}$ .

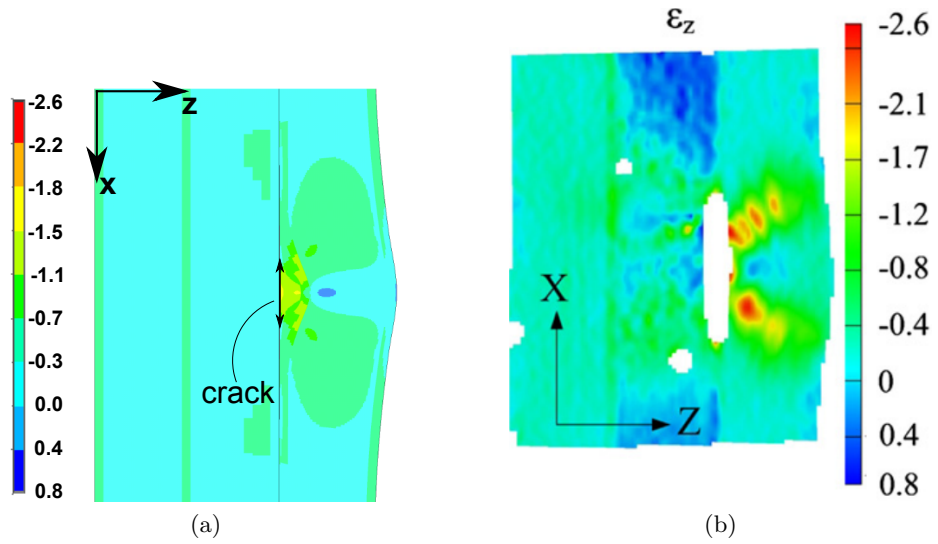


Figure 6.3: Plot of the transverse normal strain ( $\epsilon_z$ ) after FM1 as a) obtained from FEA and b) obtained with DIC (Leong, 2012). Both plots are normalised with respect to the far field normal strain  $\epsilon_x^{avg}$ .

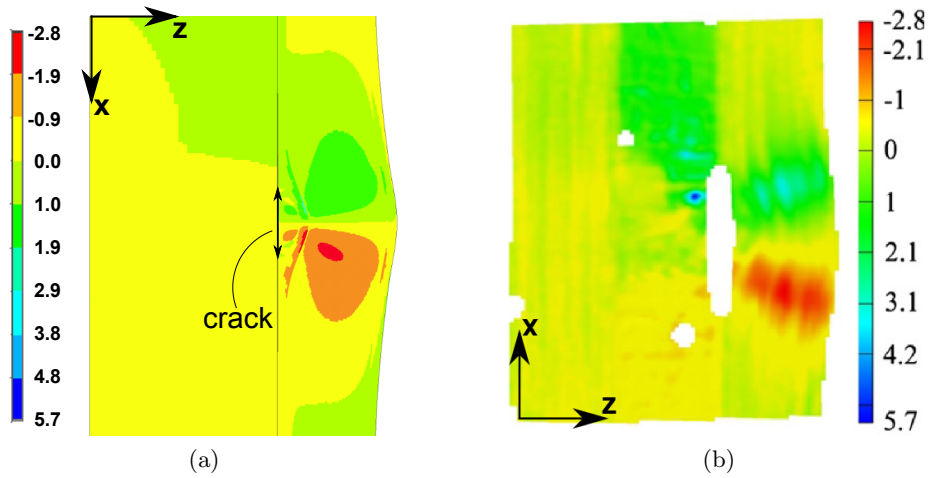


Figure 6.4: Plot of the transverse shear strain ( $\gamma_{xz}$ ) after FM1 as a) obtained from FEA and b) obtained with DIC (Leong, 2012). Both plots are normalised with respect to the far field normal strain  $\epsilon_x^{avg}$ .

It should furthermore be noted, that the load-displacement curve seen in Figure 6.5 is linear up to and beyond the FM1 load, meaning that the crack propagation in the *FM1 Interface* does not affect the normal stiffness in the global x-direction of the specimen.

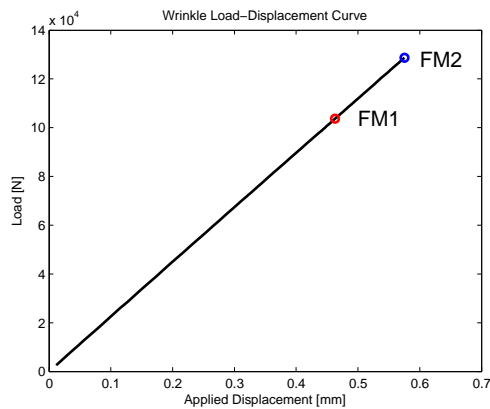


Figure 6.5: Graph of the load displacement curve obtained from the FE model.

## 6.2 Modeling FM2

This section serves to describe the problems encountered when trying to simulate delamination in the *FM2 Interfaces*. The model was meshed with CZ elements in the *FM2 Interfaces* as well as in the *FM1 Interface* as seen in Figure 5.6b on page 82. The CZM properties given in Table A.1 in Appendix A were first used for the CZ elements in the *FM2 Interfaces*. These parameters have relatively high onset tractions, and this gave convergence difficulties. In order to obtain a convergent solution the CZM properties listed in Table 6.2 were used instead. The FE model used in this section can be found on the attached CD in the folder 'Models\FM2 Wrinkle'.

FM2 CZM Properties					
$G_{Ic}$	$G_{IIc}$	$T_3^0$	$T_s^0$	K	$\eta$
613 J/m <sup>2</sup>	2252 J/m <sup>2</sup>	6 MPa	11 MPa	10 <sup>5</sup> N/mm <sup>3</sup>	1.4

Table 6.2: Parameters used in the FE model.

A contour plot of the normal strain,  $\epsilon_x$ , at the FM1 load can be seen in Figure 6.6a. From this plot it can be seen, that the normalised strain values and distributions obtained from the FE results do not match those found by DIC measurements, which are plotted in Figure 6.6b. Looking closer at Figure 6.6a it is seen, that a varying normal strain over each ply is present, indicating bending in the individual plies. This does not make physical sense, since this can only occur if delamination has occurred before FM1. Plotting the damage in the cohesive elements in the FE model at the FM1 load, as done in Figure 6.7, it is seen, that damage has evolved in a large part of the *Near Wrinkle Region*. This means, that the onset traction has been exceeded in these parts of the *Near Wrinkle Region*. The result is, that the stiffness of the interface layers is lowered so much, that the physics of a real wrinkle defect is no longer simulated correctly by the FE model. In order to simulate the crack propagation at the FM2 load, the onset traction has to be increased, such that damage only evolves after FM1.

In Figure 6.8 plots of the transverse shear stresses in the material coordinate system are shown at the FM1 and FM2 loads respectively. Note that these plots are obtained from a model with CZ elements in the *FM1 Interface* only. The plots indicate that, in order to properly capture the delamination occurring

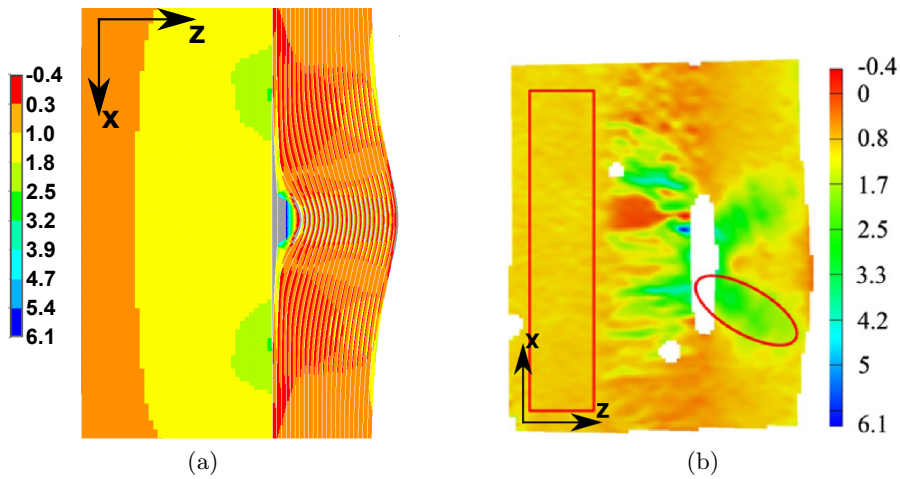


Figure 6.6: Plot of the normal strain ( $\epsilon_x$ ) after FM1 as a) obtained from FEA and b) obtained with DIC (Leong, 2012). Both plots are normalised with respect to the far field normal strain  $\epsilon_x^{avg}$ .

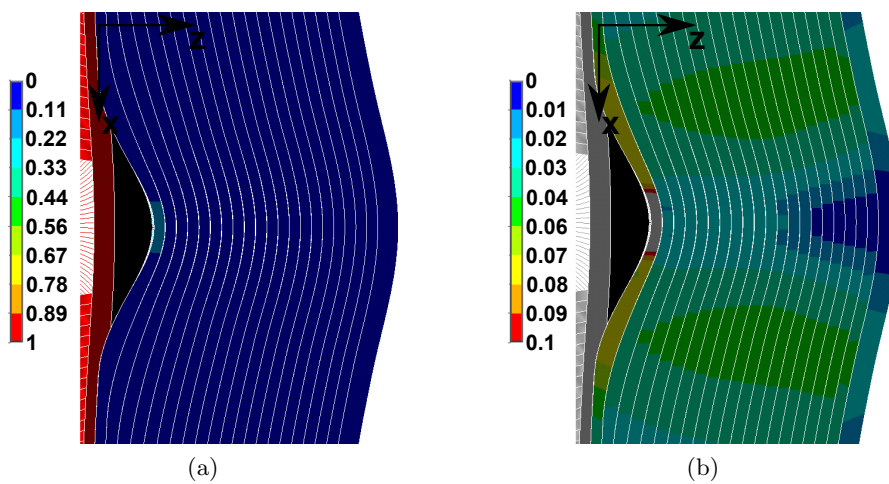


Figure 6.7: Plots of the damage at a) full scale b) narrowed scale.

after the FM1 load, the onset shear traction should be between 37.4 MPa and 48.7 MPa. This fits well with the modified CZM properties that were suggested by assistant supervisor, Brian Bak, and Martin Leong, which can be seen in Appendix A. One way to overcome the convergence difficulties associated with high onset tractions, as mentioned in section 4.3, is to refine the mesh. This approach was attempted by solving the model with a fine mesh of approximately one million nodes, which proved not to be adequate. Refining the mesh further makes the problem too time consuming to solve, and therefore other methods to overcome convergence difficulties have to be attempted. The authors of this thesis did not go any further with this.

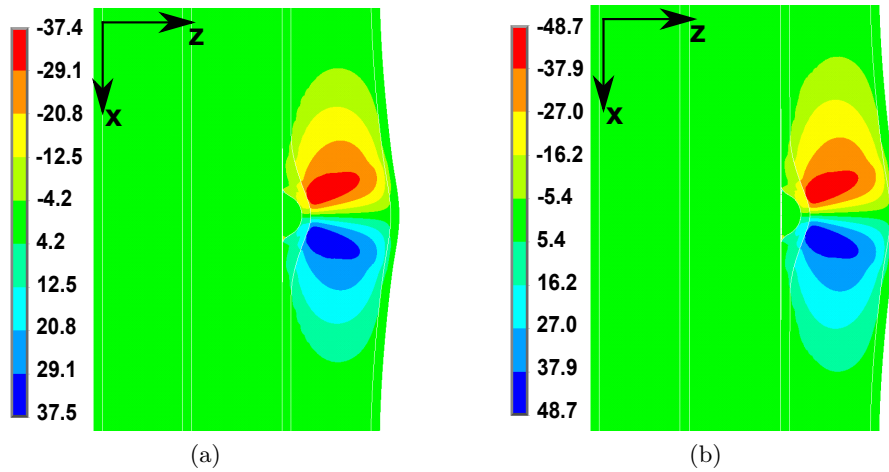


Figure 6.8: Plot of the transverse shear stress,  $\sigma_{xz}$ , in MPa in the material coordinate system a) at the FM1 load and b) at the FM2 load.

### 6.3 Mode Mixity and Damage

Even though delamination of the *Wrinkle Facesheet* after FM1 could not be simulated due to convergence difficulties, important insight in the failure process can still be obtained. From the contour plots of the damage in Figure 6.7 it is seen, that delamination in the *FM1 Interface* has occurred. Furthermore it is seen, that the greatest damage between the plies in the *Wrinkle Facesheet* occurs in the region with the largest transverse shear stresses (see Figure 6.8). This indicates, that the transverse shear stress cause the delamination and is hence detrimental to the structural integrity.

In Figure 6.9 a plot of the mode mixity, calculated according to section B.4, is seen. Noting that a value of 0 means pure mode I and a value of 1 refers to pure shear mode, it is seen, that the *FM1 Interface* is mode I dominated. The *FM2 Interfaces* are dominated by a shear mode. The mode mixity in the *FM2 Interfaces* furthermore confirms the indication, that the delaminations at the FM2 load are caused by the transverse shear stress.

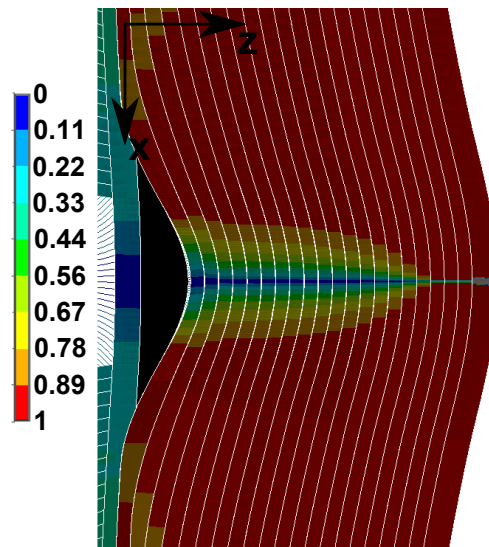


Figure 6.9: Plot of the mode mixity parameter,  $\beta$ , at the FM1 load.

## 6.4 Failure Criterion for FM2

Since it was not possible to simulate the delamination in the *FM2 Interfaces*, a different way of predicting this failure has to be used for the parametric studies carried out in Chapter 7. The Max Stress Criterion is chosen for predicting delamination and thereby failure in the *Wrinkle Facesheet*. The used failure properties are the ones given in Leong (2012), which are repeated in Table 6.3.  $F_{13}$  has though been set to 48.7 MPa, since this is the transverse shear stress observed in the FE model at the FM2 load as seen in Figure 6.8b. Note that this strength is within the range of the strength parameters given in Table A.2 in Appendix A.

In sections 6.2 and 6.3 it was argued, that the transverse shear stress was the

Max Stress Properties				
UD	$F_1$ (t/c) (MPa) 914/525	$F_2$ (t/c) (MPa) 42/121	$F_3$ (t/c) (MPa) 42/123	$F_{12/13/23}$ (MPa) 36/48.7*/10
Biax	$F_1$ (t/c) (MPa) 150/150	$F_2$ (t/c) (MPa) 150/150	$F_3$ (t/c) (MPa) 40/570	$F_{12/13/23}$ (MPa) 144/48.7*/39

Table 6.3: Parameters used for the Max Stress Criterion to predict failure in the *Wrinkle Facesheet* (Leong, 2012). \* denotes modified values.

primary cause for the delamination and subsequent failure. In Figure 6.10a a contour plot of the failure index of the Max Stress Criterion is shown, and in Figure 6.10b the failure index for the max transverse shear stress criterion (defined as  $FI_{\text{shear}} = \frac{|\sigma_{13}|}{F_{13}}$ ) is seen. The figures are very similar, showing that the Max Stress Criterion will predict failure due to the transverse shear stress. Since Leong (2012) found no load carrying capacity beyond the point, where delamination in the *Wrinkle Facesheet* started, this method is believed to be appropriate for the characterisation of the strength for a given wrinkle defect.

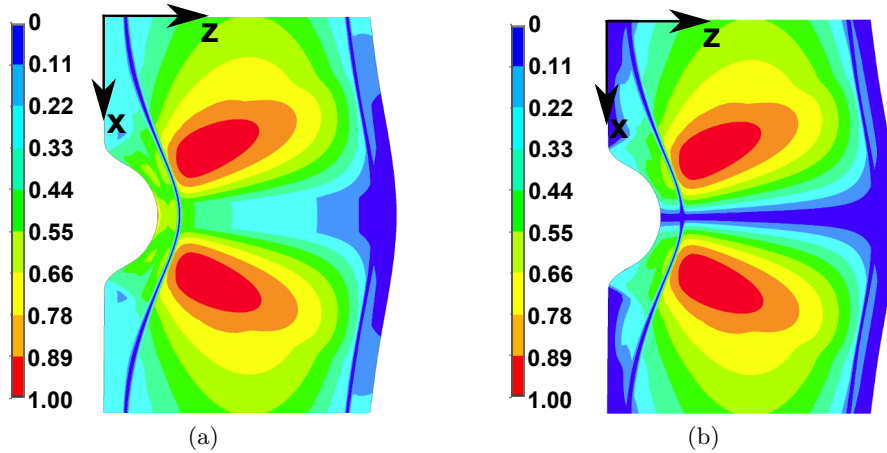


Figure 6.10: Plot of the failure indices obtained from a) the Max Stress Criterion and b) the max transverse shear stress criterion.

## 6.5 Conclusion

In section 6.1 it was found, that by the use of fitted CZM properties, FM1 could be properly simulated. Through comparisons of DIC measurements with results from the FE model it was found, that delamination in the *FM1*

*Interface* increased the strains in the *Near Wrinkle Region*. This showed the need for simulating this delamination in order to obtain a precise model for failure prediction. Due to convergence difficulties, it was not possible to simulate the delamination in the *FM2 Interfaces*. Instead it was argued, through an analysis of the mode mixity and the distribution of damage, that the transverse shear stress is the primary cause for delamination. Due to the failure being dominated by transverse shear stress, the non-interacting Max Stress Criterion was chosen to predict this delamination and thereby ultimate failure of the specimen.



## Chapter 7

# Parametric Studies

In the previous chapters the FE model was verified, and a choice of a suitable criterion for predicting specimen failure was suggested. In this chapter, first comparisons with experimental data will be carried out. Through this comparison the model will be further verified. Some mismatch between experimental data and results from the FE model is found, and therefore a discussion on the reason for this is also provided. Following this the influence of the geometry of the wrinkle defect on the failure load will be investigated through FE analyses. This is done by performing a parametric study, where the geometry is varied, and considering the resulting failure loads. Finally a suggestion for a simple failure criterion based on key geometric wrinkle defect dimensions will be given. Note that the FE model as well as macros for data extraction and MATLAB scripts can be found on the attached CD in the folder 'Models\FM1 Wrinkle Parametric'.

### 7.1 Approach

In this section the overall approach to modelling and postprocessing will be presented in brief terms, before the results from the parametric studies are presented.

#### 7.1.1 Performing the Analyses

The model used for the parametric studies has dimensions and discretisation as shown in Table 7.1. As seen both the wrinkle height, wrinkle width and total specimen height are given in intervals. This is because these are

the parameters to be varied. The limits for these intervals are found by subjectively evaluating for which values the resulting wrinkle defect looked physically plausible. The elastic properties of the plies are as given in Table 5.4. CZ elements are used in the *FM1 Interface*, and the used CZ properties are as given in Table 6.1. The strength properties of the plies are as given in Table 6.3, but the transverse shear strength ( $F_{13}$ ) is altered and will be varied in the interval 30-70 MPa, as suggested in Appendix A, since this strength is required to represent the shear delamination strength. As seen in the table the

Geometric Parameters					
$L$	$H$	$W$	$t_{core}$	$h$	$w$
143 mm	19.8-50.5 mm	10 mm	9.5 mm	1.0-3.0 mm	4.5-7.0 mm
$n_f$	$Dw_L = Dw_R$	$Dh_L = Dh_R$	$\alpha_L = \alpha_R$	$v_x$	
22	0.288 mm	1.25 mm	10 °	-1.32 mm	
Mesh Parameters					
CE1	CE2	CE3	CE4	CE5	CE6
1	20	4	10	200	200
CE7	CE8	CE9			
50	50	200			

Table 7.1: Parameters used for the FE model.

analyses are performed with a rather large prescribed displacement resulting in a reaction force of approximately 325kN. This serves to ensure, that the specimen will fail for all the tested wrinkle geometries. The problem is solved with the Newton-Raphson solver, automatic time-stepping and a minimum of 85 substeps. Results are saved for every substep.

### 7.1.2 Data Extraction

For extracting data an APDL macro has been written. This macro reads a results file and then loops through all substeps to find the last substep with a maximum failure index less than one. In principle, results from a substep with a max failure index of exactly one (the specimen is at its failure load) are wanted, but no simple method for stopping the solution depending on the maximum failure index is found. This is the reason, that the analyses are performed for a large prescribed displacement and a minimum number of substeps are set. It is judged, that by picking the last substep with a max failure index less than one, results are acceptably close to the results at failure. For the found substep, the maximum failure index, the maximum and minimum

transverse shear stress ( $\sigma_{13}$ ), the force applied to the specimen (the reaction force at the displacement BC), and the length of the crack in the *FM1 Interface* is output.

From the above approach a lot of analyses have been performed. This has been done by running ANSYS in batch mode, with the model parameters and settings as well as data manipulation handled by MATLAB. This has provided for a highly automated approach for data generation. In order to make sure that all the performed analyses make physical sense, the geometry for each wrinkle defect geometry has been checked. In Figure 7.1 a select set of the analysed geometries, which are chosen so they span the treated parametric space, are shown. As a note to the geometries it should be mentioned, that

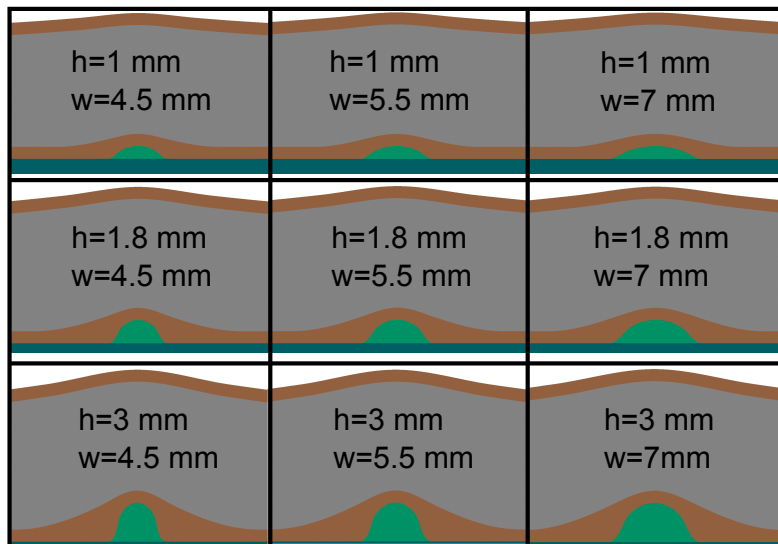


Figure 7.1: The wrinkle geometries for some of the analysed wrinkle defects.

the FE model starts to break down for wrinkle defects with high height to width ratios. This is due to the way the geometry is constructed, that leads to the plies closest to the *Epoxy Inclusion* becoming very thick as seen in the figure. It is unclear what really happens in this inner region of a wrinkle defect due to lack of experimental data, but it is recognised that results from the FE model may be less reliable for these geometries.

## 7.2 Analyses in Absolute Parameters

The analyses are performed with the wrinkle height and wrinkle width varying independently in the intervals presented in Table 7.1 in a six by six grid. The specimen height is kept constant at 30 mm and the value of the ply transverse shear strength has been chosen as  $F_{13} = 48.7$  MPa in order to provide the correct failure load for the previously examined specimen (specimen 5 in Leong (2012)). In Figure 7.2 a surface plot of the failure loads for the examined wrinkle defect geometries is seen from two different perspectives. In

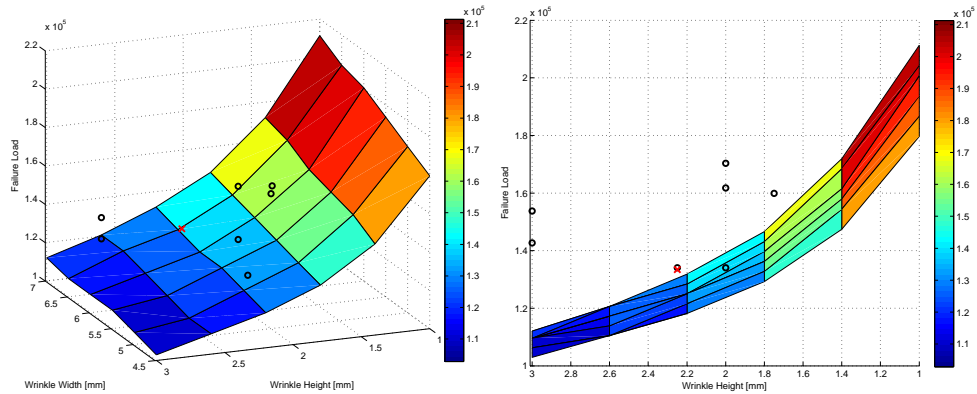


Figure 7.2: Surface plot of the failure loads as a function of the width and height of the wrinkle defect seen from two different perspectives. The failure loads from Leong (2012) are marked with circles (specimen 5 marked with red cross). Note that the absolute value of the failure load is shown.

the figure, the failure loads obtained by Leong (2012) are also shown with circles. It is seen, that specimen 5 almost lies on the surface, and it is noted, that for the chosen shear strength, the obtained surface plot is conservative with respect to the rest of the data points. Specimen 5 is not exactly on the surface, as should be the case, due to the results not being read exactly for  $FI=1$ , as mentioned in section 7.1.2. Some agreement in the tendencies between the data points from Leong (2012) and the surface plot is hinted, but it would require a lot more experimental data to properly verify this agreement. The need for more experimental data is also evident from the surface plot, in that especially small measurement errors in the height of the wrinkle defect can result in large differences in the predicted failure load, due to the high slope of the surface. Thus a data set of sufficient size to provide for a sta-

tistical treatment is necessary. Furthermore the transverse shear strength in Appendix A is given in a rather large range. In Figure 7.3 surface plots of the failure load calculated from the max transverse shear criterion for the bounds on the transverse shear strengths are seen. From these surface plots it is seen, that all failure loads obtained by Leong (2012) lies between the two surfaces. If the transverse shear strength varies as much as given in Appendix A from specimen to specimen, this might explain the scatter in the data from Leong (2012). It should be noted, that at a transverse shear strength of 70 MPa, failure due to transverse shear is no longer the governing failure mode.

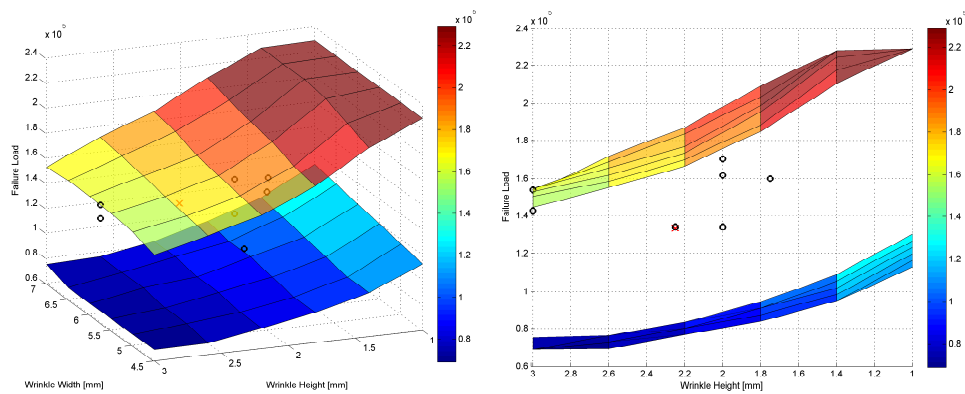


Figure 7.3: Surface plot of the failure loads as a function of the width and height of the wrinkle defect seen from two different perspectives. The failure loads from Leong (2012) are marked with circles (specimen 5 marked with red cross). Note that the absolute value of the failure load is shown.

Considering the tendencies in Figure 7.2, it is seen that the failure load is only slightly affected by the width of the wrinkle defect, and that a greater width increases the failure load. On the other hand, the failure load appears to be highly sensitive to the height of the wrinkle defect, with greater height leading to lower failure loads. This indicates that it is critical, in order to accurately predict the failure load, to be able to precisely measure the wrinkle height.

In order to ensure, that the plots in Figure 7.2 are governed by the transverse shear strength, it is checked if the critical failure mode for any of the analyses has changed. In Figures 7.4a and 7.4b the maximum failure indices from the Max Stress Criterion and the max transverse shear stress criterion

are plotted respectively. It is seen that the two plots are identical. This again shows, that the transverse shear stress is indeed governing for the failure of all the analysed geometries. From the figures it can also be noticed, that the surfaces are slightly wavy, even though all failure indices should be 1. This is due to the way the results are read from the analyses, as described in section 7.1, which does not guarantee results at the failure load. It is however seen that the lowest failure index has a value above 0.96, which is considered to be acceptably close to the failure load.

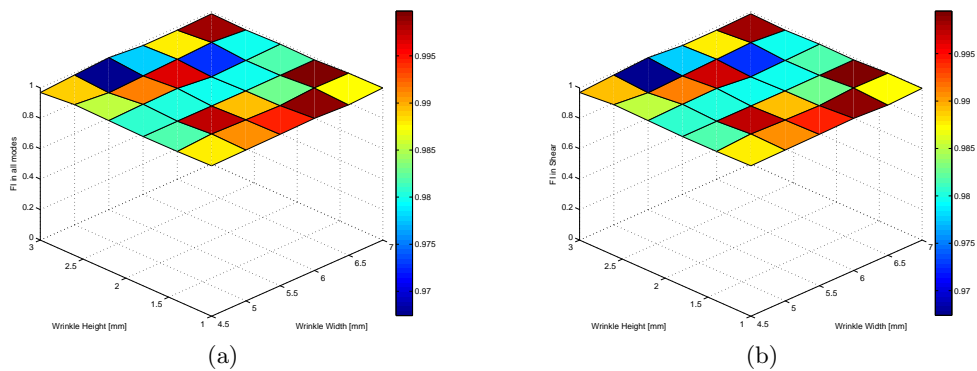


Figure 7.4: Plot of the maximum failure index for a) the Max Stress Criterion and b) for the max transverse shear stress criterion.

In Figure 7.5 a surface plot of the length of the crack in the *FM1 Interface* at specimen failure is shown. Here it is again seen, that the crack length is more affected by the height of the wrinkle defect than the width. It is also seen that increasing either dimension of the wrinkle defect, will increase the length of the crack. It is worth noticing, that this stands in contrast to the behaviour of the failure loads, where the failure load increased for larger wrinkle widths. This indicates, that a large *FM1 Interface* crack is not necessarily detrimental to the load carrying capability of the structure for a static compressional loading.

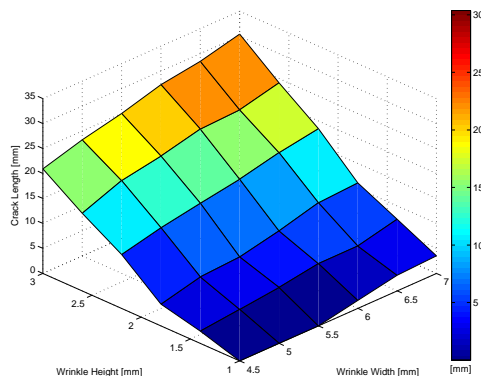


Figure 7.5: Surface plot of the length of the *FM1 Interface* crack at the failure load as a function of the width and height of the wrinkle defect.

### 7.3 Analyses in Normalised Parameters

In order to provide for a more general applicability of the conclusions obtained from the parametric studies, normalised studies are carried out. In these studies, the following dimensionless quantities are considered:

- $\alpha = t_{facesheet}/t_{core}$  in the range [0.54:2.16]
- $\beta = h_{wrinkle}/t_{facesheet}$  in the range [0.1:0.3]
- $\gamma = w_{wrinkle}/h_{wrinkle}$  in the range [1.5:7]

where the ranges of each variable are obtained from the intervals in Table 7.1. As it might be noticed in the table,  $t_{core}$  is kept constant. Thus by varying  $t_{facesheet}$  it can be shown, whether the relative core thickness has any influence on the specimen strength. Furthermore plots in the following are created for constant  $\beta$ . This is done in order to examine if the absolute dimensions of the wrinkle defect has any influence on the failure index for a given displacement BC. Independence of overall dimensions is of course a prerequisite for a meaningful normalisation of the problem. In order to have a normalised description, the strength of the specimen can of course not be described by a failure load, which is size dependent. One option would be to consider the far field stress at failure, but here it is chosen to simply consider the maximum failure index for a given average specimen strain. It should be noted, that that all results in this section are obtained with a prescribed displacement boundary condition of 0.53 mm.

In Figure 7.6 surface plots of the maximum failure index are shown from two different perspectives. As seen three surfaces, corresponding to  $\beta = 0.1$ ,  $\beta = 0.2$ , and  $\beta = 0.3$  respectively, are present in the figure. Several conclusions can be drawn from the figures. It is seen, that the three surfaces are well separated, meaning that  $\beta$  has a significant influence on the load carrying capacity of the specimen. Increasing  $\beta$  increases the failure index meaning that the specimen strength is reduced. This is of course expected, since increasing  $\beta$  will lead to a larger part of the *Wrinkle Facesheet* being severely affected by the geometric disturbance of the wrinkle defect. It is also seen, that increasing  $\gamma$  lowers the failure index. This again shows the tendency, found in section 7.2, that increasing wrinkle height or decreasing wrinkle width is detrimental to the load carrying capability of the specimen.

Finally it is seen, in the side view of Figure 7.6, that for lower values of  $\beta$  there is almost no dependence on  $\alpha$ . It was found that for  $\beta = 0.1$  and  $\beta = 0.2$  the deviation along the  $\alpha$  direction was within  $\pm 1.2\%$  of the mean value. This indicates that, for low values of  $\beta$ ,  $\alpha$  has little to no effect on the failure index, which again indicates that the size of the core does not significantly affect the strength of a specimen containing a wrinkle defect, as long as the wrinkle defect is small compared to the facesheet thickness. It should be noted that the authors did not investigate why  $\alpha$  had an influence on the failure index for  $\beta = 0.3$ . The above results indicate size independence

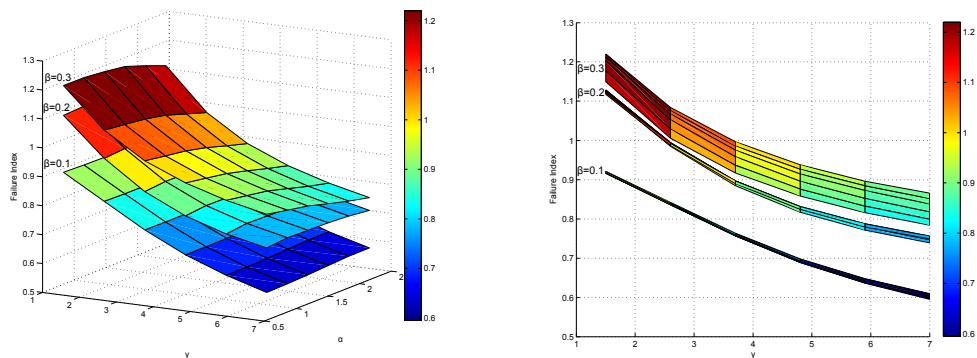


Figure 7.6: Surface plots of the failure index as a function of  $\alpha$  and  $\gamma$  for three different values of  $\beta$ .

and also shows that the load carrying capability of a specimen containing a

wrinkle defect varies in a smooth and predictable way, provided the used FE model gives representable results. Therefore a simple criterion for predicting the failure load of a wrinkle defect based on normalised geometric parameters, will be suggested in the following section.

## 7.4 A Simple Criterion

In the previous section it was shown that within some limits, the behaviour of specimens seemed to be smooth and independent on absolute sizes. Therefore a new parametric study is performed within these limits, in order to produce a simple failure criterion by curve fitting. The analyses and data extraction for the study are performed according to section 7.1, except for the following differences: The analyses are performed with the standard specimen height, as used by Leong (2012), of  $H = 30$  mm. Furthermore the analyses are performed in a six by six grid in the following normalised space:

$$0.1 \leq \beta \leq 0.2 \quad (7.4.1)$$

$$1.5 \leq \gamma \leq 7.0 \quad (7.4.2)$$

This results in the wrinkle height and width varying in the intervals  $h = [1.03; 2.05]$  mm and  $w = [1.54; 14.35]$  mm respectively. Note that the value of  $\beta$  is taken to a maximum of 0.2 only, because it was shown in section 7.3 that above this value, the results started to show dependence on  $\alpha$ . In this section the considered normalised (size independent) specimen strength is taken as the far field facesheet normal stress,  $\sigma_x^{farfield}$ , at specimen failure.

A simple criterion for finding the specimen strength, within the above parametric space, is obtained by creating a polynomial curvefit from the analysis results. This is done using MATLAB's 'cftool'. It was found, that a polynomial surface of second degree in both  $\beta$  and  $\gamma$  provided a good fit with

$$R = 0.9978$$

$$RMSE = 1.518 \text{ MPa}$$

The resulting function for predicting the specimen strength is:

$$\sigma_x^{farfield}[\beta, \gamma] = p_0 + p_1\beta + p_2\gamma + p_3\beta^2 + p_4\gamma^2 + p_5\beta\gamma \quad (7.4.3)$$

with

$$p_0 = -190.3 \text{ MPa}$$

$$p_1 = 768.4 \text{ MPa}$$

$$p_2 = -27.46 \text{ MPa}$$

$$p_3 = -1917 \text{ MPa}$$

$$p_4 = 0.83 \text{ MPa}$$

$$p_5 = 44.44 \text{ MPa}$$

In Figure 7.7 the data points obtained from the FE analyses are shown together with a surface plot of the fitted polynomial surface. As the goodness of fit parameters indicate, the surface accurately fits the data points. In Figure 7.8, Figure 7.2 is reproduced, and an additional surface plot, generated with the found polynomial fit, is added. It is seen that the curve fit deviates from the FE results for  $\beta > 0.2$  (corresponding to wrinkle heights  $h > 2$  mm), as would be expected, and that it coincides with the FE results in the region of validity. More importantly, it is seen that the curvefit provides conservative estimates of the failure loads for the specimens examined by Leong (2012).

It is recognised that the found criterion most likely is not suited for actual failure prediction at SWP for several reasons: First of all, the FE model used for generating it, has not been properly verified due to lack of experimental data. Second it is not known how representative the artificially created wrinkle defects in the specimens, examined by Leong (2012), are for wrinkle defects inherent in SWP blades. Finally, in this thesis as well as in the work of Leong (2012), only a compressive load has been considered. However the above curvefit is presented in order to demonstrate, that it might be possible, with a sufficient amount of experimental data, to produce a relatively simple failure criterion, that can be used for quick and inexpensive estimates of the strength of laminated sandwich panels of various sizes and compositions containing wrinkle defects of different sizes and geometries.

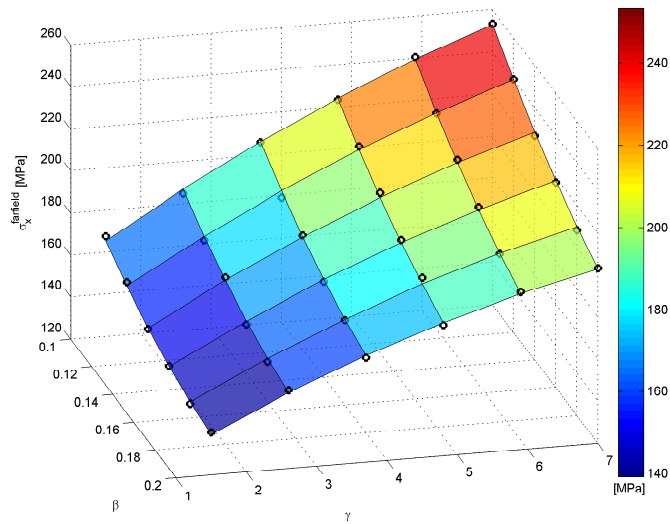


Figure 7.7: Data points obtained from FE analysis shown as circles, together with the polynomial surface obtained by curvefitting. Note that the absolute value of the resulting stress is plotted.

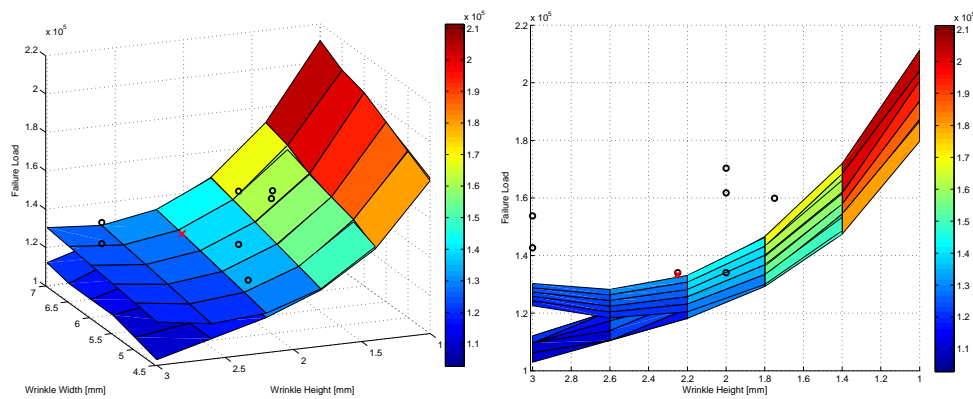


Figure 7.8: Surface plot of the failure loads as a function of the width and height of the wrinkle defect seen from two different perspectives. The failure loads from Leong (2012) are marked with circles (specimen 5 marked with red cross). Note that the absolute value of the failure load is shown.

## 7.5 Conclusion

In this chapter various parametric studies have been conducted. First the FE model was compared to all test results given in Leong (2012). From this comparison it was difficult to conclude, if the trends seen in the FE model were representative for real specimens due to the limited number of experiments. A rather large range of scatter was seen in the experimental results, which might be attributed to measurement uncertainties of the wrinkle geometries as well as varying transverse shear strengths. Provided that the FE model represents phenomena seen in real specimens, it was concluded, that increasing the height of a wrinkle had a detrimental influence on the strength of the laminate, whereas increasing the width of the wrinkle increased the strength. In the end of the chapter a study on normalised parameters was conducted. From this study a simple failure criterion for estimation of the strengths of laminated sandwich panels of various sizes and compositions containing wrinkle defects of different sizes and geometries was proposed.

## Chapter 8

# Conclusions

In this master thesis, the CZM method has been used to simulate delamination failure of a wrinkle defect in glass-epoxy laminate specimens. In order to approach the CZM method, LEFM was treated briefly. During this treatment, analytical solutions for the load-displacement curves for the DCB, ENF and MMB tests were found. Use of LEFM in the FEM was also shortly discussed, and from this discussion, it was concluded that LEFM has some advantages, but also some shortcomings that needs to be addressed. First of all LEFM requires only linear FEA's, which makes it computationally attractive. On the other hand it provides no means for predicting crack initiation. Thus it was concluded, that LEFM may not be a sufficient tool for fracture mechanical analysis, if location and size of existing cracks in a structure are not known and cannot be measured.

The discussion about LEFM provided the motivation for considering CZM, since this method can model both crack initiation and crack propagation. Therefore the CZM method was introduced next. To be able to have full control over the used CZ element within an FE package, a user programmed element was implemented. In order to do this, the theory behind a CZ element was treated in detail. A variety of choices was made, e.g. it was chosen to use a bilinear constitutive law along with the BK interaction criterion. Based on the theory, the element was implemented in ANSYS and verified through a number of analyses, where good agreement between experimental data, LEFM solutions and results provided by the use of the element was seen. The influence of selected parameters and properties was also discussed, and it was found, that the onset traction in combination with small crack lengths have

a large influence on the load, at which unstable crack growth occurs, whereas the influence is less significant for larger cracks.

Next, specimens containing artificially created wrinkle defects, which have been tested in the literature, was modelled using the FEM. The modelled geometry was compared to pictures of the actual test specimens, and good agreement was seen. The created FE model was then validated by comparing linear analyses (i.e. with no cohesive elements), with DIC measurements performed by Leong (2012) on non-delaminated specimens. In most cases the FE results matched the DIC results well, and in all cases the same trends were seen. It was furthermore found, that a simple beam model could explain some of the tendencies seen in strains in the *Near Wrinkle Region*. After validation CZ elements were introduced in the *FM1 Interface*. However the CZM properties in this interface were not known and were therefore fitted to match the experimentally seen phenomena. With the fitted properties, a post FM1 load comparison with DIC measurements was performed, and it was seen, that the model simulates FM1 failure reasonably accurate. In order to simulate delamination at the FM2 load, CZ elements were introduced between all plies. However it was found, that in order to make the model converge, the onset tractions had to be reduced significantly. This resulted in premature damage development in the *FM2 Interfaces*, which led to a structural behaviour very different from what was seen in experiments. It was argued that the reason for the delamination in the *Wrinkle Facesheet* was the transverse shear stress present in this facesheet. Therefore a different approach was taken in order to predict the FM2 load. The suggested approach was to use the Max Stress Criterion in the *Wrinkle Facesheet*, in combination with CZ elements in the *FM1 Interface*.

By the use of the developed FE model, a parametric study on absolute geometrical parameters regarding the height and width of the wrinkle was conducted. The absolute geometrical parameters were chosen, such that they covered the geometries tested in Leong (2012). The failure loads, found through the Max Stress Criterion, was of course dependent on the material strengths. The transverse shear strength was given in the interval of 30 to 70 MPa. Finding the failure loads for each of these bounds and comparing with experimentally obtained failure loads from Leong (2012), it was found that experimental

results lay inbetween those bounds. From the parametric study it was furthermore found, that the height of a wrinkle has a strong influence on the strength of a sandwich specimen in the way, that a high wrinkle decreases the strength compared to a low wrinkle. The width of the wrinkle did not influence the strength of the sandwich specimen much, but it was found, that a wide wrinkle increases the strength compared to a thin wrinkle. A parametric study on normalised geometric parameters regarding the wrinkle defect was also conducted. From this study it was found, that the strength of sandwich specimens containing a wrinkle defect was not dependent on absolute geometric parameters within some bounds on the normalised parameters. Finally a curve fitted failure criterion for normalised parameters was proposed, and it was confirmed, that the criterion corresponded to the results obtained from the parametric study using absolute geometric parameters.

## 8.1 Suggestions for Future Work

As discussed above, both strengths and weaknesses of CZM in the FEM are evident. During the study of wrinkle defects using CZM it has been found, that when the initiation of cracks is of concern, the fracture mechanical properties that are required, makes the problem difficult to solve. In order to solve using the available solvers in ANSYS, the analyses are run with an impractically fine mesh and sometimes lowered onset tractions. To deal with this either the element formulation or the solving could be looked into.

On the parametric analyses of different wrinkle defects, experimental verification is needed in order to confirm the trends seen in the FE analyses. The tested wrinkle geometries should vary more than those tested by Leong (2012) in order to validate the trends seen in the FE model. It would also be preferable to have a greater number of experiments performed for the same geometry, such that a statistical treatment of the scatter due to e.g. production precision and material changes could be carried out.

The wrinkle geometry itself also plays an important role, and should be looked into from both an experimental and a simulation aspect. From the experimental point of view precise measurement of the wrinkle is needed, since a change in height of just 0.5 mm has a big impact on the failure load, according to the

FE model. Measurements could e.g. be performed using image measuring. On the simulation side, a more precise comparison between the modelled wrinkle and a real wrinkle could be beneficial, and would be possible if close-up images from image measuring were available. This could e.g. alleviate the problem in the developed FE model, where the inner plies, close to the *Epoxy Inclusion*, becomes very thick if high height to width ratios are used.

Assuming that the above mentioned problems had been solved, the suggestion for producing a curvefit, to be used as a quick tool for estimation of strengths of sandwich panels containing wrinkle defects, could be further developed. In order to do this, further experimental work would have to be conducted, where a comparison of the artificially created wrinkle defects in the specimens, used in Leong (2012), and the wrinkle defects that arise during production of the SWP blades should be carried out. This has to be done in order to establish if the test specimens are representable for a real wrinkle defect. Furthermore experimental as well as numerical work would have to be conducted, in order to examine the behaviour of the specimens under different load cases than simple uni-axial compression.

# Nomenclature

In this list the nomenclature, which has been used in chapter 3, is provided. Nomenclature for the rest of the thesis is discussed in the text of the respective chapters.

Symbol	Explanation
$T^o$	Onset traction
$T^t$	Onset traction at a given damage
$\Delta^o$	Onset displacement
$\Delta^f$	Displacement at fracture
$\tilde{\Delta}^t$	Onset displacement for a given damage
$E_{ij}$	Cauchy strain tensor
$S_{ij}$	Piola-Kirchhoff stress tensor
$D_{ij}$	Material tangent stiffness
$d$	Damage parameter
$G$	Energy release rate
$G_c$	Critical energy release rate
$\sigma_{ij}$	Stress tensor
$\epsilon_{ij}$	Green-Lagrange strain tensor
$u_i$	Displacement vector
$\tilde{T}_i$	Prescribed external traction
$T_i$	Traction vector
$b_i$	Body force
$C_{ijkl}$	The constitutive tensor
$v_i$	Prescribed external displacement
$\Omega$	Domain of computation
$\Gamma_\sigma$	Part of boundary with prescribed tractions
$\Gamma_u$	Part of boundary with prescribed displacements
$\Gamma_{coh}$	Part of boundary containing the active cohesive zone
$\Gamma_c$	The potential crack surface
$n_i$	Surface normal vector
$\xi$	First natural/curvilinear coordinate
$\eta$	Second natural/curvilinear coordinate
$x_i$	Global coordinate
$\bar{x}_i$	Global coordinate of midsurface
$R_{ij}$	Rotation matrix mapping from local to global coordinates
$r_i$	Force vector
$q_i$	Nodal displacements
$N_{ij}$	Shape function matrix
$J$	Jacobian determinant
$\Delta_i$	Local opening displacement
$E$	Penalty stiffness
$I$	Functional
$w^k$	Displacement increment used in the Newton-Raphson solution method
$W$	Work
$\psi$	Surface potential
$\lambda$	Displacement norm
$\beta$	Mode mixity parameter



# Bibliography

- Andreasen, J. H.. 2011. *Note from Fracture Mechanics course*. Department of Mechanical and Manufacturing Engineering, Aalborg University.
- ANSYS, Inc. 2010. *ANSYS Mechanical APDL and Mechanical Applications Theory Reference*. ANSYS, Inc.
- Anton, H., I. Bivens, and S. Davis. 2012. *Calculus - Early Transcendentals*. ISBN: 978-0-470-64769-1. 10th Edition. John Wiley and Sons, inc.
- Barenblatt, G. I.. 1961. The Mathematical Theory of Equilibrium Cracks Formed in Brittle Fracture. *Zhurnal Prikladnoy Mekhaniki i Tekhnicheskoy* 1(4), 3–56.
- Camanho, P. P., C. G. Dávila, and M. F. D. Moura. 2003. Numerical Simulation of Mixed-mode Progressive Delamination in Composite Materials. *Composite Materials* 37(16), 1415–1438.
- Cook, R. D., D. S. Malkus, M. E. Plesha, and R. J. Witt. 2002. *Concepts and Applications of Finite Element Analysis*. ISBN: 0-471-35605-0. 4th Edition. John Wiley and Sons, inc.
- Dávila, C. G., P. P. Camanho, and A. Turon. 2007. Cohesive Elements for Shells. Technical Report NASA/TP-2007-214869, NASA Langley Research Center.
- Goyal, V. K.. 2002. *Analytical Modeling of the Mechanics of Nucleation and Growth of Cracks*. Faculty of Virginia Polytechnic Institute and State University.
- Kassapoglou, C.. 2010. *Design and Analysis of Composite Structures*. ISBN: 978-0-470-97263-2. 1st Edition. John Wiley and Sons, Ltd.

- Kildegaard, A.. 2006. *Elasticitetsteori*. Aalborg University. Department of Mechanical and Manufacturing, Aalborg University.
- Leong, M.. 2012. *The influence of defects on the failure of wind turbine blades*. Ph. D. thesis, Institute of Mechanical and Manufacturing Engineering, Aalborg University.
- Lindgaard, E.. 2011a. *Slides from extra lecture in Fracture Mechanics course*. Department of Mechanical and Manufacturing Engineering, Aalborg University.
- Lindgaard, E.. 2011b. *Slides from Ph.D. course in Fracture Mechanics*. Department of Mechanical and Manufacturing Engineering, Aalborg University.
- Mi, Y., M. A. Crisfield, G. A. O. Davies, and H. B. Hellweg. 1998. Progressive Delamination Using Interface Elements. *Journal of Composite Materials* 32(14), 1246.
- Reeder, J. R. and J. C. Jr.. 1990. Mixed-Mode Bending Method for Delamination Testing. *AIAA* 28(7), 1270–1276.
- Shames, I. H. and C. L. Dym. 1985. *Energy and Finite Element Methods in Structural Mechanics*. ISBN: 0-89116-505-3. 1. Hemisphere Publishing Corporation.
- Sun, C. T. and Z. Jin. 2011. *Fracture Mechanics*. 978-0-12-385001-0. 1st Edition. Academic Press.
- Turon, A.. 2006. *Simulation of Delamination in Composites under Quasi-Static and Fatigue Loading using Cohesive Zone Models*. ISBN: 978-84-690-4372-1. 1st Edition. Universitat De Girona.
- Turon, A., C. G. Dávila, P. P. Camanho, and J. Costa. 2007, July. An engineering solution for mesh size effects in the simulation of delamination using cohesive zone models. *Engineering Fracture Mechanics* 74(10), 1665–1682.
- van Kan, J., G. Segal, and F. Vermolen. 2005. *Numerical Methods in Scientific Computing*. ISBN: 13 978-90-71301-50-6. 1st Edition. VSSD.

Zenkert, D.. 1997. *The Handbook of Sandwich Construction*. EMAS Publishing.



**Part III**

**Appendix**



## Appendix A

# Fracture Mechanical Properties

Our assistant supervisor and Siemens contact, Brian Bak, has provided some CZM properties for use in laminated glass-epoxy materials. These are given in Table A.1.

$G_{Ic}$ [J/mm <sup>2</sup> ]	$G_{IIc}$ [J/mm <sup>2</sup> ]	$T_I^0$ [MPa]	$T_{II}^0$ [MPa]	K [N/mm <sup>3</sup> ]	$\eta$
0.613	2.252	12	22	$10^5$	1.4

Table A.1: Fracture mechanical properties initially provided by Brian Bak.

After later consultation with the author of Leong (2012), Brian Bak suggested that for the materials used in the wrinkle defect test specimens, the properties shown in Table A.2 are more correct.

$G_{Ic}$ [J/mm <sup>2</sup> ]	$G_{IIc}$ [J/mm <sup>2</sup> ]	$T_I^0$ [MPa]	$T_{II}^0$ [MPa]	K [N/mm <sup>3</sup> ]	$\eta$
0.613	2.252	40	30-70	$10^5$	1.4

Table A.2: Fracture mechanical properties as later suggested by Brian Bak and Martin Leong.



## Appendix B

# Implementation and Usage of the User Programmed Cohesive Zone Element

The purpose of this appendix is to describe the element implementation by the use of pseudocode. Furthermore it is presented how element results are computed and how to use the element. Before the pseudocode is presented, ANSYS specific variables used in the element formulation are described along with simple subroutines. The pseudocode documentation consists of two routines namely the element routine (section B.1) and the material routine (section B.2). The element routine is furthermore documented using a flowchart. Finally a guide for using the element is provided along with a description of the extra functionality and possibilities for output from the element, that has been implemented.

### **B.1 Element routine**

In this section the element routine is described. It should be noted, that various error checks have been left out, and the integration method documented is solely Newton-Cotes first order integration. When ANSYS calls an element formulation, pointers to arrays which contain the various data associated to the given element are provided. Not all the data provided by ANSYS is necessary in order to implement the CZ element routine successfully. In Table B.1 the names of the used pointers, as well as the type of the data

they each point to, are described. In order to keep the pseudocode for the

xRef	Global coordinates of nodes in the undeformed configuration. Data is given in a 2D array, where column $i$ represents the coordinate vector of node $i$ . The following pseudocode is written as if the columns were stacked into a 1D array.
TotValDofs	Total displacements in the global coordinate system of nodes given in a 1D array.
kfstps	Number of current equilibrium iteration.
saveVars	Element specific user state variables, which can be saved for each converged substep. Saved variables are: $[d^{node1} \ d^{node2} \ d^{node3} \ d^{node4} \ d_{dev}^{node1} \ d_{dev}^{node2} \ d_{dev}^{node3} \ d_{dev}^{node4}]$ , where $d$ represents current damage, and $d_{dev}$ describes if there was damage development in last converged substep.
realConst	Constants supplied to element when the element is defined in the modelling process. Can be defined in two ways: keyopt(1) = 0: $[T_3^o \ \Delta_3^f \ \Delta_3^o \ T_1^o \ \Delta_1^f \ \Delta_1^o \ \eta]$ , or as: keyopt(1) = 1: $[T_3^o \ G_{cI} \ E_3 \ T_1^o \ G_{cII} \ E_1 \ \eta]$

Table B.1: ANSYS pointers used to formulate the CZ element.

element routine and the material routine as simple as possible, subroutines are presented in the pseudocode. These subroutines will only be documented in the extent of what is found in Table B.2. A flowchart of the element routine is

MatParm	Converts realConst values to valid format and saves them in $\{Mat\}$ array.
Rotation	Calculates the rotation matrix based on the theory from section 3.5.
NaturalCoordinate	Returns the natural coordinates $\xi$ and $\eta$ for a given nodenumber.
NMat	Returns the shape function matrix $[N]$ for a given natural coordinate.
Traction	Calculates the traction vector $\{T\}$ .
Jacobian	Calculates the area scaling according to (3.5.5).
Diag	Changes only parameters on diagonal of matrix.
Ostiff	Calculates the material tangent stiffness matrix $[D^{TAN}]$ for the case where damage is developing.

Table B.2: Functions which are used in pseudocode to simplify documentation. These functions will not be documented, but this table gives a short description of their purpose.

seen in Figure B.1 and the pseudocode can be found in Algorithm 1 in the end of this appendix. It should be noted, that besides the output described in the pseudocode the element routine is also capable of returning other results for the user to use and plot. Furthermore some additional numerical functions are added. Descriptions of the added features and possible outputs are described in section B.4, but was left out of the pseudocode for simplicity.

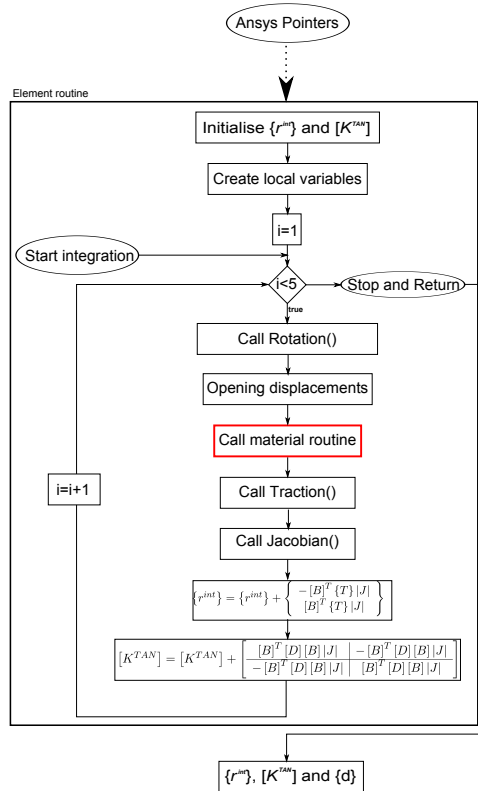


Figure B.1: Flowchart of the element routine. The arguments of called functions have been left out for simplicity.

## B.2 Material routine

The material routine is called for each iteration of the integration loop in the element routine as indicated by the red box in Figure B.1. The pseudocode for the material routine is given in Algorithm 2 in the end of this appendix.

## B.3 Using the Element with ANSYS

Usage of the element can be split into three parts:

- Configuration of ANSYS and Windows to support UPF elements.
- Using the element.
- Postprocessing of element results.

For examples on using the element, it is advised to look into APDL input files included on the appendix CD.

### B.3.1 Configuration of PC

ANSYS must be installed with ANSYS Customisation Files as shown on B.2. Furthermore some path variables need to be defined. This can be done by:

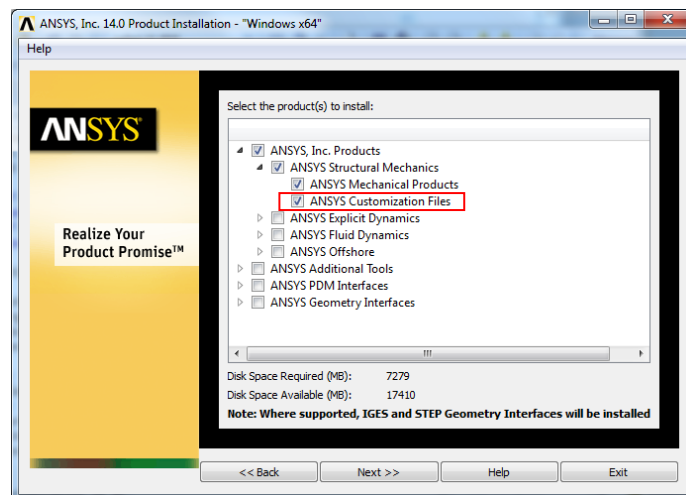


Figure B.2: ANSYS Installation.

- Run (windows +R) type: "control.exe sysdm.cpl,System" and select "Environment Variables"
- Add a new system variable named: "ANS\_USE\_UPF" and set the value to "TRUE"
- Add a new system variable named: "ANS\_USER\_PATH" and set the value to *[WorkingDirectory]*, e.g. "C:\FEM\ANSYS\"

- Add the following to the already defined system variable "Path": [*Location of ANSYS.exe*], e.g. "C:\Program Files\ANSYS Inc\v140\ansys\bin\winx64\;"
- Copy "UserElemLib.dll" from the attached CD (found in the folder 'UPF DLL') into the location you used for *WorkingDirectory*

### B.3.2 Using the Element

To use the element you should have the following in your APDL script:

```
\UPF,UserElem
ET,1,USER300
USRDOF,DEFINE,UX,UY,UZ
USRELEM,8,3,BRICK,10,17,,0,4,3,0
```

These parameters should not be changed, as they refer to element type, number of integration points, number of real constants and number of saved variables. See ANSYS, Inc (2010) for more information.

#### Keyoptions

Keyoptions can be set using:

KEYOPT,1,1,VAL     *Format of material properties input*

Select VAL=0 if material parameters are given in terms of displacements/tractions. Use VAL=1 if material parameters are given in terms of energies/tractions/penalty stiffness.

KEYOPT,1,2,VAL     *Tangent stiffness matrix conditioning*

Select VAL=0 if no conditioning should be used. Use VAL=1 or VAL=2 for Goyal (2002) modified tangent stiffness matrices. See subsection B.4.3.

#### Material Input

Material properties are set through real constants. For Keyoption VAL=0 input is in the following order:

```
R,1,Nmax,Dfmode1,D0mode1,Smax,Dfmode2/3,D0mode2/3
RMORE,1,eta,nEquiSec,initD,mu
```

or for Keyoption VAL=1:

```
R,1,Nmax,G1c,PenaltyK,Smax,G2/3c,PenaltyK,eta,nEquiSec,initD,mu (keyoption
1=1)
RMORE,1,eta,nEquiSec,initD,mu
```

where the names denote the properties seen in Table B.3. With regards to nEquiSec and mu, see section B.4.

Name	Meaning
Nmax	Onset traction in mode 1
Dfmode1	Final mode 1 opening displacement (full damage)
D0mode1	Mode 1 onset opening displacement
Smax	Onset traction in mode 2 and 3
Dfmode2/3	Final mode 2 and 3 opening displacement (full damage)
D0mode2/3	Mode 2 and 3 onset opening displacement
eta	The curve fitting parameter in the B-K criterion
G1c	The critical energy release rate in mode 1
PenaltyK	The penalty stiffness
G2/3c	The critical energy release rate in mode 2/3
nEquiSec	Maximum number of equilibrium iterations to be performed before the element will use the secant stiffness instead of the tangent stiffness. If 0 or empty field is used, the tangent stiffness will always be used
initD	The initial element damage
mu	The damping factor

Table B.3: Meaning of input parameters.

## Meshing

Since CZ elements initially have a volume of zero, meshing will give errors unless done in the following way. First mesh with ANSYS interface element INTER205 using the command CZMESH, see ANSYS, Inc (2010) for more information. Then after meshing, change all interface elements to the UPF. This can be done using the EMODIF command.

### B.3.3 Postprocessing

Result data from the CZ element is saved in stress/strain/strain energy postprocessing fields according to Table B.4. For information on the last four result variables, see section B.4.

Quantity	Plotted in ANSYS by	APDL Command
$\Delta_3$	Elastic strain in y-direction	PLNSOL,EPEL,Y
$\Delta_1$	Elastic strain in xy-direction	PLNSOL,EPEL,XY
$\Delta_2$	Elastic strain in zy-direction	PLNSOL,EPEL,YZ
$T_3$	Stress in y-direction	PLNSOL,S,Y
$T_1$	Stress in xy-direction	PLNSOL,S,XY
$T_2$	Stress in zy-direction	PLNSOL,S,YZ
$d_E$	Elastic strain <b>OR</b> stress in x-direction	PLNSOL,EPEL,X <b>OR</b> PLNSOL,S,X
$\beta_{avg}$	Stress in z-direction	PLNSOL,S,Z
$E_{stored}$	Element Strain Energy	PLESOL,SENE
$E_{dissipated}$	Elastic strain in z-direction	PLNSOL,EPEL,Z

Table B.4: Result variables saved for each element.

## B.4 Additional Element Features

During the project extra functionality has been added to the element as necessary or for experimentation. The added functionality is listed below, and is subsequently described in further detail.

- Additional Element Results
- Damage Damping
- Tangent Stiffness Matrix Conditioning
- History Dependent Choice of Material Tangent Stiffness
- Initialising Damage
- Convergence Dependent Tangent Stiffness

### B.4.1 Additional Element Results

As mentioned in section 4.1, the possibilities of outputting and plotting the element damage, mode mixity and element energies (dissipated and stored) have been added. These are described below.

**Element Energies:** The element stored energy is the energy that is contained in the element "elastically" - that is, the energy that can be recovered from the element upon unloading. This energy is, in the notation of section 3.7, simply calculated as:

$$E_{stored} = \frac{1}{2} \{ \mathbf{r}^{int, ce_k} \}^T \{ \mathbf{q} \} \quad (\text{B.4.1})$$

The dissipated energy is calculated from the equivalent properties for the current mode mixity as found in the material routine. Thus the current critical energy release rate is:

$$G_c = \frac{1}{2} T^0 \Delta^f \quad (\text{B.4.2})$$

The energy that can still be put into the element before full damage has occurred is calculated dependent on the current damage as:

$$G_{left} = \frac{1}{2} E (1 - d) \tilde{\Delta}^0 \Delta^f \quad (\text{B.4.3})$$

The dissipated energy in the element is then calculated as:

$$E_{dissipated} = \iint_{ce_k} (G_c - G_{left}) d\bar{\Gamma} \quad (\text{B.4.4})$$

**Element Damage:** The element damage is calculated based on the above energies as:

$$d_E = \frac{E_{dissipated}}{G_c} \quad (\text{B.4.5})$$

It should be noted that the dissipated energy and thus also the element damage are not completely correct, since they do not take into account the element history, but are calculated from the present state only.

**Mode Mixity:** Finally the element mode mixity is calculated as a running average mode mixity over the course of damage development in the element. This is done using a temporary mode mixity "contribution" defined as:

$$\beta_{contrib}^i = \beta_{contrib}^{i-1} + \beta^i (d_E^i - d_E^{i-1}) \quad (\text{B.4.6})$$

where  $i$  refers to the iteration number. The running average is then calculated as:

$$\beta_{avg}^i = \frac{\beta_{contrib}^i}{d_E^i} \quad (\text{B.4.7})$$

By calculating the mode mixity to be output this way, it should represent the dominating mode mixity over the life of the element. Note also that for elements in which no damage has occurred, the value  $-1$  is output to emphasise that the mode mixity concept in this case makes no sense.

### B.4.2 Damage Damping

Damage damping has been implemented, but not tested properly. Hence it should only be used as an experimental feature. The damping is implemented following the method used by Dávila et al. (2007), using the following expression for the damped damage parameter:

$$d_{damped}^i = \frac{\Delta t}{\mu + \Delta t} d^i + \frac{\mu}{\mu + \Delta t} d_{damped}^{i-1} \quad (\text{B.4.8})$$

where  $\mu$  is the damping parameter.

### B.4.3 Tangent Stiffness Matrix Conditioning

Some modifications to the element consistent tangent stiffness matrix have been suggested by Goyal (2002). These modifications have been implemented and can be enabled and chosen by setting KEYOPT(2) of the element. The implemented modifications, in the notation of section 3.9, can be stated as:

$$[\mathbf{M}]_{ii} = \max(0, [\mathbf{M}]_{ii}) \quad \text{for} \quad \text{KEYOPT}(2)=1 \quad (\text{B.4.9})$$

$$[\mathbf{K}^{\text{tan}}]_{ii} = \max(0, [\mathbf{K}^{\text{tan}}]_{ii}) \quad \text{for} \quad \text{KEYOPT}(2)=2 \quad (\text{B.4.10})$$

These modifications are described in Goyal (2002, eq. (4.18) and (4.19)) respectively.

### B.4.4 History Dependent Choice of Material Tangent Stiffness

For each converged substep, the element stores information about whether damage were developing or not in that substep. Now when the next substep is initiated, the initial guess for the material tangent stiffness is chosen according to this information.

### **B.4.5 Initialising Damage**

The element damage parameter can be initialised upon model creation. This function is especially practical for modelling pre-existing cracks in the structure by introducing elements with  $d = 1$ .

### **B.4.6 Convergence Dependent Tangent Stiffness**

By setting the value of  $nEquiSec$ , the element material routine will change from returning  $D^{\tan 2}$  to returning  $D^{\tan 1}$ , when the number of equilibrium steps performed in any given substep exceeds the number in  $nEquiSec$ . See Figure 3.13 on page 49.

---

**Algorithm 1** Main subroutine

---

**function** USERELEM**Input:** Standard element input from Ansys

▷ Initialise internal force vector and tangent stiffness matrix

$$\{r^{int}\} = 0$$

$$[K^{TAN}] = 0$$

▷ Create local variables

$$\{u^-\} = \text{TotValDofs}(1:12)$$

$$\{u^+\} = \text{TotValDofs}(13:24)$$

$$\{Mat\} = \text{MATPARAM}(\text{RealConst})$$

▷ Numerical Newton-Cotes integration

**for**  $i = 1 \rightarrow 4$  **do**

$$\xi, \eta = \text{NATURALCOORDINATE}(i)$$

$$[R] = \text{ROTATION}(\text{xRef}, \{u^-\}, \{u^+\}, \xi, \eta)$$

$$[N] = \text{NMAT}(\xi, \eta)$$

$$\{\Delta\} = [R][N] (\{u^+\} - \{u^-\})$$

$$[D^{TAN}], d, E = \text{MATDAMAGE}(\text{saveVars}, i, \{\Delta\}, \{Mat\})$$

$$\{T\} = \text{TRACTION}(\{\Delta\}, d, E)$$

$$|J| = \text{JACOBIAN}(\text{xRef}, \{u^-\}, \{u^+\}, \xi, \eta)$$

$$\{r^{int}\} = \{r^{int}\} + \begin{Bmatrix} -[N]^T [R]^T \{T\} |J| \\ [N]^T [R]^T \{T\} |J| \end{Bmatrix}$$

$$[M] = [M] + [N]^T [R]^T [D^{TAN}] [R] [N] |J|$$

**end for**

$$[K^{TAN}] = [K^{TAN}] + \left[ \begin{array}{c|c} [M] & -[M] \\ \hline -[M] & [M] \end{array} \right]$$

**return**  $[K^{TAN}], \{r^{int}\}, \{d\}$ **end function**

---

---

**Algorithm 2** Material subroutine

---

**function** MATDAMAGE(saveVars,i,{ $\Delta$ },{*Mat*},kfstps)

$$tol = 10^{-19}$$

▷ Calculate  $\lambda$  and  $\beta$  and disregard  $\Delta_3$  if interfacial penetration is present

$$\Delta_s = \sqrt{\{\Delta\}_1^2 + \{\Delta\}_2^2}$$

**if**  $\{\Delta\}_3 < tol$  **then**

$$\lambda = \Delta_s$$

$$\beta = 1$$

**else**

$$\lambda = \sqrt{\{\Delta\}^T \{\Delta\}}$$

$$\beta = \frac{\Delta_s}{\Delta_s + \langle \Delta_3 \rangle}$$

**end if**

▷ Calculate mode mixity parameter

$$B = \frac{\beta^2}{1 + 2\beta^2 - 2\beta}$$

▷ Calculate material parameters for the found mode mixity

$$d = \text{saveVars}(i)$$

$$\Delta^o = \sqrt{(\Delta_3^o)^2 + \left( (\Delta_1^o)^2 - (\Delta_3^o)^2 \right) B^\eta}$$

$$T^o = \sqrt{(T_3^o)^2 + \left( (T_1^o)^2 - (T_3^o)^2 \right) B^\eta}$$

$$E = \frac{T^o}{\Delta^o}$$

$$\Delta^f = \frac{\Delta_3^f \Delta_3^o + \left( \Delta_1^f \Delta_1^o - \Delta_3^f \Delta_3^o \right) B}{\Delta_3^o}$$

---

---

**Algorithm 2** Material subroutine (continued)

---

▷ Calculate the onset displacement  $\Delta^{o,old}$  from the last converged substep

$$\Delta^{o,old} = \frac{\Delta^o \Delta^f}{\Delta^f - d(\Delta^f - \Delta^o)}$$

▷ Check for opening or closing, and calculate new damage

**if**  $\lambda > \Delta^{o,old}$  **then**

$$d = \min \left( \frac{\Delta^f (\lambda - \Delta^o)}{\lambda (\Delta^f - \Delta^o)}, 1 \right)$$

**end if**

▷ Calculate closing stiffness

$$[D^{TAN}] = 0$$

$$diag([D^{TAN}]) = (1 - d) E$$

**if**  $\{\Delta\}_3 < 0$  **then**

$$[D^{TAN}]_{33} = [D^{TAN}]_{33} + dE$$

**end if**

▷ For first equilibrium iteration decide whether to expect damage development or not

$$d_{dev} = saveVars(i + 4)$$

**if**  $kfstps == 1$  **then**

**if**  $d_{dev} == true$  **then**

$OpenStiff = true$  ▷ Expect damage development

**else**

$OpenStiff = false$  ▷ Expect unloading

**end if**

**else**

**if**  $\lambda > \Delta^{o,old}$  AND  $\lambda < \Delta^f$  **then**

$OpenStiff = true$  ▷ Damage development

**else**

$OpenStiff = false$  ▷ unloading

**end if**

**end if**

---

---

**Algorithm 2** Material subroutine (continued)

---

▷ If opening is expected, modify tangent stiffness matrix to represent opening stiffnesses.

**if** *Openstiff* == *true* **then**

    OSTIFF( $[D^{TAN}]$ )

**end if**

**end function**

**return**  $[D^{TAN}]$ ,d,E

---